Hybrid functional study of point defects in germanium

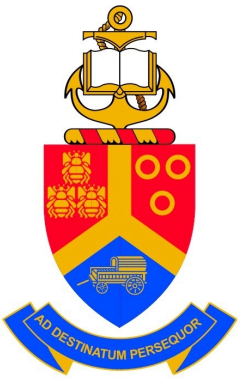

by
Emmanuel Igumbor

Submitted in partial fulfilment of the requirements
for the degree
Doctor of Philosophy (PhD) in Physics
in the Faculty of Natural and Agricultural Sciences
University of Pretoria

Promoter: Prof Walter E. Meyer
Co-promoter: Dr Richard C. Andrew

January 5, 2017

Declaration

I, **EMMANUEL IGUMBOR**, student number **13120795**, declare that this thesis, which I hereby submit for the degree of Doctor of Philosophy in Physics at the University of Pretoria, is my own work and has not been previously submitted by me for a degree at this or any other tertiary institution.

SIGNATURE:.....

DATE:.....

Abstract

Hybrid functional study of point defects in germanium

by

Igumbor Emmanuel

Submitted in partial fulfilment of the requirements for the degree Doctor of Philosophy (PhD) in Physics in the Faculty of Natural and Agricultural Sciences, University of Pretoria.

Promoter: Prof Walter E. Meyer

Co-promoter: Dr Richard C. Andrew

Germanium exhibits electron and hole mobilities that are higher than silicon. These unique properties make Ge a promising material for the development of metal-oxide semiconductor field effect transistors (MOSFETs). Point defects in semiconductors influence the electronic structure as well as the thermodynamic and optical properties of the material. Well-known defects in Ge have been intensively studied experimentally and results reported.

In the past, defects in Ge were difficult to study theoretically, since the *local density approximation* (LDA) and the *generalized gradient approximation* (GGA) functionals in the framework of density functional theory (DFT) incorrectly predict Ge to be a metal. However, the screened hybrid functional developed by Heyd, Scuseria, and Ernzerhof (HSE) accurately predicts the band gap and gives better estimates of the charge state transition levels of point defects in semiconductors. This thesis reports the results of DFT calculations using the HSE06 functional to predict the structural, electronic and charge state thermodynamic properties of Ge di-interstitials, rare earth (RE) substitutional and interstitial impurities as well as vacancy-RE impurity complexes in Ge.

Results obtained showed that the Ge di-interstitial could exist in three configurations with formation energies between 6.53 and 7.63 eV. The lowest energy configuration was the double tetrahedral configuration with a binding energy of 1.24 eV. This configuration induced only a shallow donor level at an energy of 0.04 eV below the conduction band minimum. Other configurations of the Ge di-interstitial exhibited negative-U ordering.

RE interstitials in Ge formed with formation energies between −4.76 and 6.71 eV, with the Pr interstitial in Ge having the lowest formation energy at −4.76 eV for the neutral charge state in the tetrahedral configuration. The tetrahedral configuration was the most stable configuration for the Ce, Pr, Eu and Tm, while the Er interstitial showed charge state controlled metastability. While the Ce interstitial induced a shallow donor level in the band gap, the Eu and Er interstitials induced deep levels within the band gap of Ge. The Pr interstitial in Ge did not induce any charge state transition levels, with the neutral charge state stable for all Fermi energies in the band gap.

Tm^{3+} defects in Ge formed with formation energies between 1.81 and 5.31 eV for the neutral charge state. Of all the Tm^{3+} related defects in Ge studied, the Tm_i^{3+} in the tetrahedral configuration formed with the lowest formation energy of 1.81 eV. Tm_i^{3+} induced a shallow donor level, while Tm_{Ge}^{3+} and Tm_i^{3+}-V_{Ge} induced both acceptor and donor levels that were deep and shallow. Tm^{3+} substitutional and vacancy complex (Tm_{Ge}^{3+}-V_{Ge}) in Ge exhibited charge state controlled metastability and negative-U ordering.

The role of the di-interstitial, vacancy related defects, substitutional impurities and vacancy-interstitial complexes in Ge were pointed out and it is expected that the data and information presented will be useful in the process modelling of Ge-based devices for industrial, laboratory applications and for comparison to experimental results.

Dedication

This thesis is dedicated to Almighty God.

Acknowledgements

My special appreciation goes to the following persons and organizations for their contributions towards the completion of this study:

- My promoter, Prof W. E. Meyer and co-promoter, Dr R. C. Andrew for their guidance, encouragement, valuable discussions and support.
- The University of Pretoria, Department of Physics and the National Research Foundation of South Africa (NRF) for financial support during the entire duration of this study.
- My colleagues in the Department of Physics of the University of Pretoria for their willingness to help, their interest and encouragement.
- All members of the computational and solid state research group at the University of Pretoria for their fruitful and constructive, discussions.
- All members of the Thin film and semiconductor research group at the University of Pretoria for their support and fruitful discussions.
- My family for their endless support and encouragement, in particular my parents Evangelist and Mrs M. A. Igumbor, all my siblings and their spouses.
- My lovely wife Dr Brenda and my dear son Excel-Rima for their love, moral support, encouragement and perseverance while the study last.
- The almighty God for His providence, love, care and guidance.

Contents

List of Figures

List of Tables

Acronyms

BOA	Born-Oppenheimer approximation
CBM	Conduction band minimum
DFT	Density functional theory
DLTS	Deep-level transient spectroscopy
DOS	Density of states
E_b	Binding energy
E_A	Electron affinity
E_C	Conduction band minimum energy
E_D	Donor level
EMT	Effective Mass Theory
E_V	Valence band maximum energy
GGA	Generalized gradient approximation
HSE	Heyd, Scuseria, and Ernzerhof
I_A	Ionisation energy
LDA	Local Density Approximation
LPAW	Linearised augmented-plane-wave
LYP	Lee-Yang-Parr
LSDA	Local spin density approximation
LSDFT	Local spin density functional theory
MOSFETs	Metal-oxide semiconductor field effect transistors
PACs	Perturbed angular correlation spectroscopy
PAW	Projector augmented wave
PBE	Perdew, Burke, and Ernzerhof
PBEsol	Perdew, Burke, and Ernzerhof for solid
RE	Rare earth
VBM	Valence band maximum
XC	Exchange-correlation

Symbols

$\hat{H}$	Hamiltonian
$\vec{r}_i$	Spatial coordinate
σ_i	Spin coordinate
e	Acceptor level
$\hbar$	Planck constant
χ	Spin orbital
Ψ	Wavefunction
ζ	Local spin polarisation
ω	Adjustable parameter
3D	Three dimensions
$\mathbf{k}$	Wave vector
ε_F	Fermi energy
μ	Chemical potential
$\epsilon(q/q')$	Transition level
U^{eff}	Effective U
Å	Angstroms

Chapter 1

Introduction

This chapter presents a concise introduction of the topic of interest–hybrid functional study of point defects in germanium. The rationale and motivation behind the research work presented in this thesis are summarized. In addition, objectives and overview of the thesis are given.

1.1 Rationale and motivation

A concise summary of the past and the present technological applications of germanium (Ge), a semiconductor with a band gap of 0.78 eV [1] at 0 Kelvin was written by Haller 2006 [2] and Claeys and Simoen (2011) [3]. One of these important applications is in the field of microelectronics. Ge as a semiconductor material has gained renewed interest due to its electron and hole mobilities that are higher than silicon (Si) [3]. This advantage makes Ge a promising material for the development of metal-oxide semiconductor field effect transistors (MOSFETs). However, despite this important application of Ge, there have been several challenges surrounding the successful implementation of Ge as MOSFETs [3]. Claeys and Simoen (2011) [3] in a detailed report, highlighted the possible future direction for the semiconductor industry and the probable role that

Ge can play.

Point defects in semiconductors have been reported to influence the quality of device performance either positively or negatively [3]. Control of defects in semiconductor materials has played a major role in improving the quality of materials for industrial and laboratory applications. The understanding of defects and their thermodynamic charge state transitions is important for controlling and engineering their formation in order to optimize the properties of the material. The successful implementation of Ge based high mobility semiconductor devices lies in the proper understanding of the formation of point defects and the charge state transition levels created within the band gap of Ge.

For some time now, numerous challenges facing the successful production of Ge based semiconductors can be attributed to the fact that the role defects play in Ge were not fully understood. For instance, the electrically active defects induced by electron irradiation in Ge need to be fully comprehended [3]. Recently, several experimental methods have been used to study electron irradiation induced defects in Ge [4, 5, 6, 7]. Experimental studies of defects in Ge, using the deep level transient spectroscopy (DLTS) [4, 6, 8] and perturbed angular correlation spectroscopy (PACs) [9] techniques have led to successful detection of point defects in Ge. While the experimental study of point defects in Ge is gaining interest, first principle modelling of point defects in Ge is relatively scarce.

Density functional theory (DFT) [10, 11] is an *ab initio* method that is frequently used to model the electronic structure of materials, and requires the use of a functional to determine the energy of the electron charge density. These functionals can be classified as: the local density approximation (LDA) [12], generalised gradient approximations (GGA) e.g., the Perdew, Burke, and Ernzerhof (PBE) [13, 14] and hybrid functionals, e.g the Heyd, Scuseria, and Ernzerhof (HSE) [15]. The LDA and GGA have been used for more than two decades. However, despite the huge success achieved

by using the LDA and GGA in predicting lattice constants and structural properties of materials, they have major shortcoming. One of the major failures of the LDA and GGA exchange correlation energy functionals, is their inability to accurately predict the band gap of materials [16, 17, 18, 19, 20]. For example, LDA and GGA predict Ge to be semi-metallic without a band gap! Consequently, the electronic and charge state transition properties were difficult to predict and often predicted wrongly [16, 17, 18].

The HSE on the other hand, accurately predicts the band gap of most semiconductor materials [19, 20]. Since the advent of the hybrid functionals, the study of point defects in Ge is beginning to gain momentum and better predictions for the band gap and charge state transition levels of Ge have been obtained. However, there are still more properties (structural, electrical and thermodynamic) of point defects in Ge to be fully studied. For example, charge state controlled metastability, negative-U properties and the formation of vacancy complexes have not been fully studied theoretically. In addition, the properties of rare earth related point defects in Ge have not yet been fully investigated theoretically. The successful implementation of Ge based semiconductor devices requires the proper understanding of the formation of defects and their electrical properties.

This thesis contributes to this body of knowledge by presenting a hybrid functional study of point defects in Ge from first principle by means of DFT. The impact and roles of di-interstitials, vacancy complexes, substitutional impurities and rare earth (RE) related point defects in Ge have been investigated, with emphases on their structural properties, electronic structures, formation energies and charged state transition properties.

1.2 Research objective and goals

This thesis presents results of various investigations of the nature and electrical properties of point defects in Ge using the HSE06 hybrid functional. Since point defects influence the electrical properties of Ge, it is paramount to know which point defects are present and how they affect the performance of Ge based devices. In order to understand how to control point defect activities in Ge, a comprehensive fundamental study of their electronic properties and geometric structures needs to be made. In addition, the energies required for point defects to form and the thermodynamic charge state transition levels induced by defects in the band gap of Ge, need to be scientifically investigated as well. The main objectives and goals of this study are as follows:

1. To investigate the stability and formation of the *di*-interstitial point defect in Ge from first principles, using the HSE06 hybrid functional.

2. To predict the thermodynamic charge state transition levels of Ge *di*-interstitials using the HSE06 hybrid functional.

3. To predict the electrical behaviour of rare earth (RE) point defects in Ge. These results will help to understand the influence of the RE interstitial and substitutional defects in Ge.

4. To investigate the presence of charge state controlled metastability and negative-U properties in a number of RE related and *di*-interstitial defects in Ge.

5. To identify and predict the properties of dopant and RE dopant-vacancy complexes in Ge using the HSE06 functional.

1.3 Overview of study

In this thesis, the electronic properties, formation energies and charge state transition levels of point defects in Ge as calculated using the HSE06 functional, are presented. Synopsis of the thesis is given below.

1.3.1 Synopsis

1. **Chapter 2** presents the theoretical background and the underlying principle of density functional theory. Also discussed in this chapter is the use of pseudopotentials and a number of different exchange correlation functionals, which include the local density approximation (LDA), generalised gradient approximation (GGA) and the hybrid functionals.

2. **Chapter 3** presents the general theory of defects in semiconductors, with emphasis on the structural and electronic properties of point defects in Ge. In addition, the chapter also highlights point defects in Ge that have been reported in literature.

3. In **Chapter 4**, the methods that are use to study the properties of point defects in semiconductors are discussed. The effect on the approximations of the accuracy of the results is also discussed. Finally, the validation of the techniques and approximations used to obtain the results presented in this thesis is also given.

4. **Chapter 5** contains the results obtained in this study, which are presented under the headings discussed:

   (a) Ab initio study of germanium *di*-interstitial using a hybrid functional.

   (b) A hybrid functional calculation of Tm^{3+} defect in germanium.

   (c) Rare earth interstitials in Ge: a hybrid density functional theory study

(d) A first principle hybrid functional calculation of Tm_{Ge}^{3+}-V_{Ge} defect complexes in Ge.

Finally, the results of this thesis are summarized under the topics:

- The stability of vacancy complexes in Ge.
- Charged state controlled meta-stability
- The negative-U ordering of point defects in Ge.

5. In **Chapter 6**, the important conclusions from results presented in **Chapter 5** are highlighted. In addition, recommendations for future work are listed.

Chapter 2

Density functional theory: a theoretical background

2.1 Introduction

Different theoretical methods and approximations are used by scientists to model many-body problems. In this chapter, the basic problem and steps taken to construct a number of methods adopted over the years to solve many-body problems, will be discussed. Many-body problems and the Born-Oppenheimer approximation (BOA) will be discussed in Section 2.2, the Hartree-Fock theory (HF) in Section 2.3 and density functional theory (DFT) in Section 2.4. Various exchange-correlation energy functionals which include the local density approximation, the generalized gradient approximation and the hybrid functional are discussed in Section 2.5. In addition, the techniques adopted to address the infinitely many electrons in a solid-state system are discussed in Section 2.6, the formalism of the pseudopotential and Brillouin zone (BZ) integration are discussed in Section 2.7 and Section 2.8, respectively.

All mathematical proofs that are associated with many-body problems and DFT in this chapter, followed Richard Martin's approach in the book entitled "Electronic

structure, basic theory and practical methods" [21, 22]

2.2 The many-body wavefunction problem

Basically, the many-body problem Schrödinger equation for a specific set of atoms in a specific configuration is given as [23, 24]

$$\hat{H}\Psi_i = E_i\Psi_i, \tag{2.1}$$

where $\hat{H}$ is the Hamiltonian and the many-body wavefunction is represented by Ψ_i which corresponds to the ith state with energy E_i . In general, the Ψ_i is a function of the electron spin and co-ordinates as well as the nuclear positions. The Ψ_i is defined as

$$\Psi_i = \Psi_i(\vec{r}_1, ..., \vec{r}_N, \sigma_1, ..., \sigma_N : \vec{R}_1, ..., \vec{R}_M, \delta_1, ..., \delta_M), \tag{2.2}$$

where $\vec{r}$ and σ are the spatial and spin coordinates of the electrons, respectively. $\vec{R}$ and δ represent the spatial and spin coordinates of the nuclei [21, 22], respectively.

The Hamiltonian operator for a set of N number of electrons in a field due to M number of ions of charge Z_K at sites R_K is given as [23]:

$$\begin{aligned}\hat{H} = -\frac{\hbar^2}{2m_e}\sum_{k=1}^{N}\nabla_k^2 - \frac{1}{2}\sum_{K=1}^{M}\frac{\hbar^2}{M_K}\nabla_K^2 + \frac{1}{2}\sum_{k\neq i}^{N}\frac{e^2}{|\vec{r}_k - \vec{r}_i|} \\ + \sum_{k=1}^{N}\sum_{K=1}^{M}\frac{Z_K e^2}{|\vec{r}_k - \vec{R}_K|} + \frac{1}{2}\sum_{K\neq L}^{M}\frac{Z_K Z_L e^2}{|\vec{R}_K - \vec{R}_L|}\end{aligned} \tag{2.3}$$

where M_K is the atomic mass of each of the nuclei, e and m_e are the electron charge and mass, respectively. The first and second terms of Equation (2.3) describe the kinetic energy operator ($\hat{T}_k$) of the electrons and the kinetic energy operator ($\hat{T}_K$) of the ions, respectively. The coulomb interaction between the electrons (third term in Equation (2.3)) is the internal potential and the electron-nuclei coulomb interaction

(fourth term in Equation (2.3)) is referred to as the external potential. Finally the last term of Equation (2.3) is the coulomb interaction between the nuclei. When atomic units are used with $\hbar = m_e = e = 1$ where 1 $a.u.$ of length called a Bohr is equal to 0.529 Å, and 1 $a.u.$ of energy is equivalent to 27.21 eV (which is also known as a Hartree). Equation (2.3) is then written in a simpler form as follows:

1. The kinetic energy operator of the electrons $\hat{T}_e$ becomes:

$$\hat{T}_e = -\frac{1}{2}\sum_{k=1}^{N} \nabla_k^2. \tag{2.4}$$

2. The kinetic energy operator of the ions $\hat{T}_K$ becomes:

$$\hat{T}_K = -\frac{1}{2}\sum_{K=1}^{M} \nabla_K^2. \tag{2.5}$$

3. The coulomb interaction between electrons becomes:

$$\hat{V}_{ee} = \frac{1}{2}\sum_{k\neq i}^{N} \frac{e^2}{|\vec{r}_k - \vec{r}_i|}. \tag{2.6}$$

4. The electron-nuclei coulomb interaction becomes:

$$\hat{V}_{ie} = \sum_{k,K}^{M} \frac{Z_K e^2}{|\vec{r}_k - \vec{R}_K|}. \tag{2.7}$$

5. The coulomb interaction between the nuclei becomes:

$$\hat{V}_{ii} = \frac{1}{2}\sum_{K\neq L}^{M,N} \frac{Z_K Z_L e^2}{|\vec{R}_K - \vec{R}_L|}. \tag{2.8}$$

The Hamiltonian defined in Equation (2.3) can now be expressed in terms of the oper-

ators defined in Equation (2.4) to Equation (2.8) as

$$\hat{H} = \hat{T}_e + \hat{T}_K + \hat{V}_{ee} + \hat{V}_{ie} + \hat{V}_{ii}. \tag{2.9}$$

Solving Equation (2.1) with the Hamiltonian in Equation (2.3) in practice is difficult, because of the many interactions due to the presence of the electrons and ions. With the Hamiltonian, it is best done by decoupling the motion of the electrons from that of the ions. The electron many-body problem is then solved by considering each electron experiencing an effective potential due to its interaction with other electrons and ions. Subsequently, the forces on the ions may be calculated by minimizing the energy with respect to the position of the ions, which will then lead to an equilibrium geometric structure. The big question is how can we separate the electrons from the ions of the many-body wavefunction problem? To attempt to solve the complex many-body problem, the adiabatic or the Born-Oppenheimer approximation is introduced.

2.2.1 Adiabatic (Born-Oppenheimer) approximation

This approximation decouples the Schrödinger equation of Equation (2.3) of the coupled nucleus-electron system. In this approximation, it is assumed that due to the large mass of an ion compared to that of an electron, the ions can be considered as being stationary when the electron wave function is calculated [25]. This implies that the effect of the momentum of the electrons on the nuclei is neglected [22, 24]. This leads to a separate Schrödinger equation for the nuclei, which separates the problem into an electronic part and an ionic part where electrons are moving in the array of fixed nuclei with a time-independent potential. The Hamiltonian of the many-body electronic problem is then approximated as [25]

$$\hat{H} = \hat{T}_e + \hat{V}_{ee} + \hat{V}_{ie}, \tag{2.10}$$

and hence, for the electron wave function, Equation (2.1) becomes

$$\hat{H}_{elec}\Psi_{elec}(\vec{r}_1, \vec{r}_2, ...) = E_{elec}\Psi_{elec}(\vec{r}_1, \vec{r}_2, ...). \tag{2.11}$$

The Hamiltonian in Equation (2.11) can be written in the form

$$\hat{H} = \hat{T}_e + \hat{V}_{ee} + \hat{V}_{ie}, \tag{2.12}$$

with

$$\hat{T}_e = -\frac{1}{2}\sum_{k=1}^{N} \nabla_k^2, \tag{2.13}$$

$$\hat{V}_{ee} = \frac{1}{2}\sum_{k\neq i}^{N} \frac{1}{|\vec{r}_k - \vec{r}_i|}, \tag{2.14}$$

and finally

$$\hat{V}_{ie} = \sum_{k,K}^{M,N} \frac{Z_K}{|\vec{r}_k - \vec{R}_K|}. \tag{2.15}$$

Note that the parametric dependence of Ψ_{elec} on $\vec{R}_L$ was explicitly omitted from Equation (2.3) by the Born-Oppenheimer approximation. The total energy can be written as the sum of the E_{elec} and $E_{nucleus}$, and thus is given as

$$E_{tot} = E_{elec} + E_{nucleus} \tag{2.16}$$

One interesting part of the Born-Oppenheimer approximation is that the number of variables in the Hamiltonian of Equation (2.3) has been reduced, but the resulting Schrödinger equation is still difficult to solve. One of the earliest approximations that help to solve Equation (2.11) is the Hartree approximation [26].

2.3 The Hartree-Fock (HF) method

2.3.1 The Hartree equation

The Hartree approximation was derived in 1928 [27]. In this approximation, the many-body wavefunction Ψ_{tot} is written as a product of single particle functions as

$$\Psi_{tot}(\vec{r}_1, \vec{r}_2, ..., \vec{r}_N) = \Psi(\vec{r}_1), \Psi(\vec{r}_2), ..., \Psi(\vec{r}_N), \tag{2.17}$$

where each of the wave functions $\Psi_k(\vec{r}_k)$ satisfies the single electron Schrödinger equation. The Hamiltonian $\hat{H}$ as a result of the Hartree approximation is

$$\hat{H}^H = \hat{T}_e + \hat{V}_{ee}^H + \hat{V}_{ie}, \tag{2.18}$$

where $\hat{T}_e = -\frac{1}{2}\bigtriangledown^2$ is the one-electron kinetic energy operator term, $\hat{V}_{ee}^H$ is the Hartree potential, defined as

$$\hat{V}_{ee}^H = \sum_{i \neq j} \int \frac{d\vec{r}}{|\vec{r}_i - \vec{r}_j{}'|} n_i(\vec{r}). \tag{2.19}$$

The $n_i(\vec{r})$ of Equation (2.19), is the probability density of the ith particle, defined as

$$n_i(\vec{r}) = |\psi_i(\vec{r})|^2. \tag{2.20}$$

2.3.2 The Hartree-Fock approximation

The Hartree wave function in Equation (2.17) neglects the fact that electrons are indistinguishable Fermions. The wave functions of Fermions are antisymmetric with respect to interchanging any pair of particles [26]. The deficiency in Equation (2.17) can be corrected by forming a new wave function which is a linear combination of Hartree products in the form of a determinant called a Slater determinant after John

Slater [28, 29].

$$\Psi(\vec{r}_1,\vec{r}_2,....,\vec{r}_N;\sigma_1,\sigma_2,....,\sigma_N)=\frac{1}{\sqrt{N!}}\begin{vmatrix}\chi_1(\vec{r}_1,\sigma_1) & \chi_2(\vec{r}_1,\sigma_1) & .... & \chi_\alpha(\vec{r}_1\sigma_1)\\ \chi_1(\vec{r}_2,\sigma_2) & \chi_2(\vec{r}_2,\sigma_2) & .... & \chi_\alpha(\vec{r}_2,\sigma_2)\\ . & . & .... & .\\ . & . & .... & .\\ . & . & .... & .\\ . & . & .... & .\\ \chi_1(\vec{r}_N,\sigma_N) & \chi_2(\vec{r}_N,\sigma_N) & .... & \chi_\alpha(\vec{r}_\alpha,\sigma_\alpha)\end{vmatrix}, \tag{2.21}$$

where the factor in front of the matrix ensures normalization, $\chi_i(\vec{r}_i,\sigma_i)$ are single particle spin-orbitals, each of which is a product of a functions of position $\phi(\vec{r}_i)$ and spin variable $\alpha(\sigma_i)$. For an arbitrary number of electrons, the wavefunction form in Equation (2.21) can be shown to satisfy the desired antisymmetry condition. A single Slater determinant is used as an approximation to the electronic wavefunction in Hartree-Fock theory. Equation (2.21) satisfies the Pauli exclusion principle (no two electrons occupy the same state).

2.3.3 The Hartree-Fock equations

The expectation of the Hamiltonian of an $N-$electron system can be approximated by using the antisymmetric wave function that was derived in Equation (2.21), and the variational principle as

$$\begin{aligned}\langle\Psi|H|\Psi\rangle=&\sum_{i,\sigma}\int d^3\vec{r}\psi_i^{\sigma*}(\vec{r})[T_e+V_{ext}]\psi_i^{\sigma}(\vec{r})+V_{ee}^H\\ -\frac{1}{2}&\sum_{i,j,\sigma}\int d^3\vec{r}d^3\vec{r}'\psi_i^{\sigma*}(\vec{r})\psi_j^{\sigma*}(\vec{r}')\frac{1}{|\vec{r}-\vec{r}'|}\psi_j^{\sigma}(\vec{r})\psi_i^{\sigma}(\vec{r}').\end{aligned} \tag{2.22}$$

The single-body expectation values (the first term in Equation (2.22)) represents that of the Hartree approximation. The last term of Equation (2.22) is the exact exchange energy which describes the Coulomb interaction between electrons of the same spin. The exchange potential energy term in Equation (2.22), can be represented as the sum over all orbitals of the same spin as

$$V_x^{i,\sigma}(\vec{r}) = -[\sum_{i,j} \int d^3(\vec{r}')\psi_j^{\sigma *}(\vec{r}')\psi_i^{\sigma}(\vec{r}')\frac{1}{|\vec{r}-\vec{r}'|}]\frac{\psi_j^{\sigma}(\vec{r})}{\psi_i^{\sigma}(\vec{r})}. \tag{2.23}$$

By minimising Equation (2.22) with respect to the many-body Slater wavefunction of Equation (2.21), the single-electron Hartree-Fock Hamiltonian is [26]

$$\begin{aligned}\hat{H}^H = [-\frac{1}{2}\bigtriangledown^2 - \sum_{K=1}\frac{Z_K}{|\vec{r}-\vec{R}_K|}]\Psi_v(\vec{r}) + \sum_{\mu=1}^{N}\int|\Psi_\mu(\vec{r}')|^2\frac{1}{|\vec{r}-\vec{r}'|}\Psi_v(\vec{r})d^3(\vec{r}') \\ -\sum_{\mu=1}^{N}\int\Psi_\mu^*(\vec{r}')\frac{1}{|\vec{r}-\vec{r}'|}\Psi_v(\vec{r}')\Psi_\mu(\vec{r})d^3(\vec{r}').\end{aligned} \tag{2.24}$$

Careful observation of Equation (2.24) shows that it has an extra term compared to the Hartree equation, called the exchange potential. The exchange potential term, which incorporates the Pauli exclusion principle for all electrons, cancels the non-physical self-interaction of electrons in the Hartree equation and hence the derived energy becomes a functional of the orthonormal single electron wavefunctions.

One major problem of the Hartree-Fock approximation is its inability to describe the known properties of the homogeneous electron gas. In short, Hartree-Fock approximation predicts that the electronic density of states vanishes at the Fermi level, which is not true. This wrong prediction is a result of neglecting the Coulomb repulsion felt by all electrons of opposite spin. This introduces a correlation energy for the electrons in Equation (2.24), which is described as the energy difference between the exact and Hartree-Fock energies [22]. To resolve this shortcoming, numerous approaches called

post-Hartree-Fock methods [30, 31], were developed. One of these approaches is density functional theory [10, 11] which takes into account both the effects of exchange and correlation energy.

2.4 Density functional theory

The first theory developed to deal with the electron energy and its density distribution was propounded by Thomas [32] in 1927 and Fermi [33] in 1928. Density functional theory (DFT) was invented by Kohn and Hohenberg [10, 11] in 1964 and was later made practical by Kohn and Sham [12] in 1965. DFT makes the electron density $n(\vec{r})$ the central quantity. Due to this reformulation, many-body problems can be simplified, because instead of dealing with the $3N$ spatial coordinates for the many-body wavefunction, $n(\vec{r})$ now depends on 3 spatial coordinates only [34, 35].

2.4.1 Hohenberg-Kohn theorem

DFT is based on two Hohenberg-Kohn (HK) theorems [10, 11].

1. **The uniqueness theorem:** This theorem states that for any system of interacting particles in an external potential, the external potential is determined uniquely (except for a constant) by the ground state electron density [23]. Mathematically the density is expressed as

$$n(\vec{r}) = \sum_{K=1}^{N} |\Psi_K|^2 \tag{2.25}$$

To prove the Hohenberg-Kohn theorem, the following assumptions will be made:

- Consider two different external potentials $V_{ext}^{(1)}(\vec{r})$ and $V_{ext}^{(2)}(\vec{r})$ with two distinct ground state wave functions $\Psi_{ext}^{(1)}$ and $\Psi_{ext}^{(2)}$, respectively, and that the ground states are non-degenerate.
- $V_{ext}^{(1)}(\vec{r})$ and $V_{ext}^{(2)}(\vec{r})$ differ by more than constant.

- However, $V_{ext}^{(1)}(\vec{r})$ and $V_{ext}^{(2)}(\vec{r})$ produce the same ground state density $n(\vec{r})$ having two distinct wave functions $\Psi_{ext}^{(1)}$ and $\Psi_{ext}^{(2)}$ belonging to two different Hamiltonians $\hat{H}_{ext}^{(1)}(\vec{r})$ and $\hat{H}_{ext}^{(2)}(\vec{r})$ respectively.
- The ground state energies of the $\hat{H}_{ext}^{(1)}(\vec{r})$ and $\hat{H}_{ext}^{(2)}(\vec{r})$ Hamiltonians are $E^{(1*)}$ and $E^{(2*)}$ respectively.

According to the variational principle, the ground state wavefunction minimises the expectation value of the Hamiltonian,

$$E^{(1*)} = \langle \Psi_{ext}^{(1)} | \hat{H}^{(1)} | \Psi_{ext}^{(1)} \rangle < \langle \Psi_{ext}^{(2)} | \hat{H}^{(1)} | \Psi_{ext}^{(2)} \rangle. \tag{2.26}$$

By simplification, the expectation values in Equation (2.26) can be rewritten as

$$\langle \Psi_{ext}^{(2)} | \hat{H}^{(1)} | \Psi_{ext}^{(2)} \rangle = \langle \Psi_{ext}^{(2)} | \hat{H}^{(2)} | \Psi_{ext}^{(2)} \rangle + \int d\vec{r} [V_{ext}^{(1)}(\vec{r}) - V_{ext}^{(2)}(\vec{r})] n(\vec{r}), \tag{2.27}$$

so that

$$E^{(1*)} < E^{(2*)} + \int d\vec{r} [V_{ext}^{(1)}(\vec{r}) - V_{ext}^{(2)}(\vec{r})] n(\vec{r}). \tag{2.28}$$

Similarly, for

$$E^{(2*)} = \langle \Psi_{ext}^{(2)} | \hat{H}^{(1)} | \Psi_{ext}^{(2)} \rangle < \langle \Psi_{ext}^{(1)} | \hat{H}^{(2)} | \Psi_{ext}^{(1)} \rangle, \tag{2.29}$$

the expectation values can be rewritten as

$$\langle \Psi_{ext}^{(1)} | \hat{H}^{(2)} | \Psi_{ext}^{(1)} \rangle = \langle \Psi_{ext}^{(1)} | \hat{H}^{(1)} | \Psi_{ext}^{(1)} \rangle + \int d\vec{r} [V_{ext}^{(2)}(\vec{r}) - V_{ext}^{(1)}(\vec{r})] n(\vec{r}), \tag{2.30}$$

so that

$$E^{(2*)} < E^{(1*)} + \int d\vec{r} [V_{ext}^{(2)}(\vec{r}) - V_{ext}^{(1)}(\vec{r})] n(\vec{r}). \tag{2.31}$$

The addition of Equation (2.28) and Equation (2.31) results in a contradiction of

the form

$$E^{(1*)} + E^{(2*)} < E^{(2*)} + E^{(1*)}. \tag{2.32}$$

Based on the above contradiction it follows that our assumptions are not valid, i.e. $V_{ext}^{(1)}(\vec{r})$ and $V_{ext}^{(2)}(\vec{r})$ only differ by a constant. For more details of the uniqueness theorem proof, see Ref. [22]

2. **Hohenberg-Kohn theorem II:** This theorem states that a universal functional can be defined to determine the energy corresponding to a particular charge density and external potential. In addition, the exact ground state energy of the system is the absolute minimum of this functional and the density that minimizes the functional is the exact ground state density [10].

The two Hohenberg-Kohn theorems reduce the problem of finding all physical properties associated with the ground state of a system to finding the electron density that minimises the energy functional [34, 35]. According to the Hohenberg-Kohn theorem, the energy functional can be written as the sum of these two functionals corresponding to the kinetic energy and potential due to the interaction of the electrons with themselves and the external potential as

$$E^{HK}[n] = T_e[n] + E_{int}[n] + E_{ext}[n] = F^{HK}[n] + \int n(\vec{r})V_{ext}d(\vec{r}) \tag{2.33}$$

for

$$F^{HK}[n] = T_e[n] + E_{int}[n] \tag{2.34}$$

where $F^{HK}[n]$ is explicitly independent of the system, and is called the Hohenberg-Kohn functional for the kinetic energy and the electron-electron interaction energy.

Applying the variational principle according to the constraint search method derivation by Levy and Lieb [36, 37, 38], Equation (2.33) becomes

$$E_0 \leq E^{HK}[n] = F^{HK}[n] + \int n(\vec{r}) V_{ext} d(\vec{r}), \tag{2.35}$$

where E_0 is now the ground-state energy for N electrons in the external potential $V_{ext}(\vec{r})$. Equation (2.35) shows that the density which minimizes the Hohenberg-Kohn functional is the exact ground state density.

2.4.2 Kohn-Sham approach

In order to transform the fully interacting system into a non-interacting system, the Kohn-Sham (KS) approach [12] needs to be adopted. According to the Kohn-Sham method, each electron is treated separately as being subject to an effective potential due to all the other electrons [12].

In order to arrive at the final solution, an iterative method is used, whereby Equation (2.9) is used to solve the Schrödinger equation for individual electrons, and a new effective potential is obtained. This new effective potential is then used to compute the electron density which will in its turn also result in a new effective potential. This same process of solving the Schrödinger equation repeatedly and generating a new effective potential continues until the minimum energy of the system changes by less than a set limit. The iterative procedure for solving the Schrödinger equation is referred to as the Self Consistent Field (SCF) approach, this approach is iterated until the total energy and charge density have converged to within a pre-set tolerance. Convergence is guaranteed by the variational principle, that states that the solution that minimises the total energy of the system is the correct solution. This whole process relies on the fact that the ground state density of non-interacting particles in an effective potential can equally represent the exact ground state density of a system of interacting particles.

When the Kohn-Sham approach is adopted, the kinetic energy of the non-interacting particles is obtained, which is very close to the true kinetic energy of the interacting system. [12, 34].

To show the derivation of the Kohn-Sham approach, it is important to recall the definition of the total energy functional used in the Hohenberg-Kohn theorem,

$$E^{HK}[n] = T^{HK}[n] + \int_{\Omega} d^3r \hat{V}_{ext} n(\vec{r}) + E_{II}, \tag{2.36}$$

where E_{II} represents the ionic interaction and $T^{HK}[n]$ represents all internal energies, kinetic and potential, of the interacting electron system. $T^{HK}[n]$ is expressed mathematically as

$$T^{HK} = \hat{T}[n] + \hat{V}_{ee}[n], \tag{2.37}$$

where $\hat{V}_{ee}[n]$ is the electron-electron interaction potential and defined as

$$\hat{V}_{ee}^{HK}[n] = \frac{1}{2} \iint d^3r d^3r_i \frac{n(\vec{r})n(\vec{r}')}{|\vec{r} - \vec{r}'|} + NC. \tag{2.38}$$

In Equation (2.38), the first component of the equation is the Hartree term. The NC is the non-classical term described by Parr and Yang [34] as the most relevant part of the exchange-correlation energy based on the Hohenberg-Kohn theorem.

The Kohn-Sham approach introduces the concept of the auxiliary non-interacting system, with Hamiltonian [34]

$$\hat{H}^{KS} = \sum_{K=1}^{N} [-\frac{1}{2} \bigtriangledown^2 + \hat{V}^{KS} n(\vec{r})]. \tag{2.39}$$

Now considering a given system of N independent electrons, where the ground state has an electron in each of the N orbitals Ψ_i with lowest eigenvalue ϵ_i of the

Hamiltonian [22, 24, 34], the Hamiltonian for one electron system can be written as

$$[-\frac{1}{2}\bigtriangledown^2 + \hat{V}^{KS}n(\vec{r})]\Psi_k = \Psi_k\epsilon_k. \tag{2.40}$$

The above Equation (2.40) yields the density of the auxiliary Kohn-Sham system which is defined as

$$n(\vec{r}) = \sum_{k=1}^{N}|\Psi_k(\vec{r})|^2. \tag{2.41}$$

The Hohenberg-Kohn expression for the ground state energy function can now be expressed in terms of the Kohn-Sham orbital as

$$E^{KS}[n] = \hat{T}_s[n] + E_{XC}[n] + \int_\Omega d^3r\hat{V}_{ext}n(\vec{r}) + E_{II}, \tag{2.42}$$

where the $\hat{T}_s[n]$ is the independent-particle kinetic energy and is given by

$$\hat{T}_s[n] = -\frac{1}{2}\sum_{k=1}^{N}\langle\Psi_k|\bigtriangledown^2|\Psi_k\rangle. \tag{2.43}$$

The kinetic energy $\hat{T}_s[n]$ by Hohenberg-Kohn theorem is extended by Kohn and Sham, by proposing a universal functional $\hat{T}^{KS}[n]$ which includes all internal energies as

$$\hat{T}^{KS}[n] = \hat{T}_s[n] + \iint d^3rd^3r_i\frac{n(\vec{r})n(\vec{ri})}{|\vec{r}-\vec{r}|} + E_{XC}[n], \tag{2.44}$$

where $E_{XC}[n]$ is the exchange-correlation energy that contains all unknown contributions to the energy of the system. The second term in Equation (2.44) is the Hartree term. Equating $\hat{T}^{KS}[n]$ to the Hohenberg-Kohn universal function $\hat{T}^{HK}[n]$ described in Equation (2.36), we have

$$\hat{T}[n] + \hat{V}_{ee}[n] = \hat{T}_s[n] + \iint d^3rd^3r'\frac{n(\vec{r})n(\vec{r'})}{|\vec{r}-\vec{r'}|} + E_{XC}[n], \tag{2.45}$$

which yields

$$E_{XC}[n] = \hat{T}[n] - \hat{T}_s[n] + \hat{V}_{ee}[n] - \iint d^3r d^3r' \frac{n(\vec{r})n(\vec{r}')}{|\vec{r} - \vec{r}'|}, \tag{2.46}$$

or

$$E_{XC}[n] = \hat{T}[n] - \hat{T}_s[n] + E_{Hartree}[n]. \tag{2.47}$$

The exchange-correlation functional represents the difference between the true kinetic energy and the independent particle kinetic energy. In conclusion, The Kohn-Sham equation brought a major breakthrough in solving the many-body electron problem in as much as the exchange-correlation parameter is properly defined.

2.4.3 Kohn-Sham variational equations

Using the auxiliary Euler equation to solve the Kohn-Sham equation yields

$$\hat{V}_{ext}^{KS} + \frac{\delta T^{KS}[n]}{\delta n(\vec{r})} = \mu, \tag{2.48}$$

where μ is the Lagrange multiplier associated with the constant, $n = \int n(\vec{r}) d^3r$ is the electron density. When the Kohn-Sham wave function is varied and Equation (2.36) is applied, a new set of equations is obtained:

$$\frac{\delta T_s[n]}{\delta \phi^*(\vec{r})} + \frac{\delta n(\vec{r},\sigma)}{\delta \phi^*(\vec{r})}[\int_\Omega d^3r \hat{V}_{ext} n(\vec{r})] + \frac{\delta}{\delta n(\vec{r},\sigma)} \frac{1}{2} \iint d^3r d^3r' \frac{n(\vec{r})n(\vec{r}')}{|\vec{r} - \vec{r}'|} + \frac{\delta E_{XC}[n]}{\delta n(\vec{r},\sigma)}] = \frac{\delta T^{KS}[n]}{\delta \phi^*(\vec{r})}. \tag{2.49}$$

where

$$\frac{\delta T_s[n]}{\delta \phi^*(\vec{r})} = -\frac{1}{2} \bigtriangledown^2 \phi^*(\vec{r}); \frac{\delta n(\vec{r},\sigma)}{\delta \phi^*(\vec{r})} = \phi^*(\vec{r}) \tag{2.50}$$

Equation (2.49) can be reduced to

$$\hat{V}_s^{KS} = \hat{V}_{ext} + \int d^3r \frac{n(\vec{r})}{|\vec{r} - \vec{r}'|} + \hat{V}_{XC}, \tag{2.51}$$

where

$$\hat{V}_{XC} = \frac{\delta E_{XC}}{\delta n(\vec{r})} \tag{2.52}$$

is the exchange-correlation potential. The Kohn-Sham approach has an advantage over the Hartree-Fock approach due to the inclusion of the exchange-correlation energy, but unfortunately an exact computation of the exchange-correlation potential remains complex to handle [39]. In Section 2.5 the physical meaning and class of exchange-correlation potentials are discussed.

2.5 The exchange-correlation energy

The exact formulation of the exchange-correlation energy is unknown and hence it needs to be approximated. Several methods have been developed to deal with this problem. The simplest and one of the most remarkable exchange-correlation approximations is the local density approximation (LDA) [12]. The generalized gradient approximation (GGA) [13, 14] is a class of widely used exchange-correlation energy functionals.

The main deficiency of the LDA is it failure to accurately predict some properties of materials, especially the band gaps [40, 41, 42, 43] of most semiconductors. The GGA functionals yield more accurate atomization energies [44, 45, 46], total energies [47, 48] and barriers of chemical reactions than the LDA. Other notable exchange-correlation functionals are the LDA+U [49, 50], GGA+U [51] and hybrid functionals.

2.5.1 The local density approximation (LDA)

As mentioned above, one of the earliest approximations is the local density approximation (LDA) [12]. By using the LDA, the energy of an electronic system is constructed to assume that the exchange-correlation energy per electron in a particular region in the electron gas is equal to the exchange-correlation energy per electron in a homogeneous electron gas with the same electron density. With this assumption, we can write the

exchange-correlation functional $E_{XC}[n]$ as

$$E_{XC}^{LDA}[n] = \int n(\vec{r})\epsilon_{XC}(n)dr, \tag{2.53}$$

where $\epsilon_{XC}(n)$ is the exchange-correlation density for the homogeneous electron gas and $n(\vec{r})$ is the electron density. The above approximation also applies to a spin zero system, but for a spin polarised system, one simply applies the same assumptions using the exchange-correlation energy density of the spin-polarised electron-gas $\epsilon_{XC}(n^{\uparrow}n^{\downarrow})$. When spin is included, the LDA is called the local spin density approximation (LSDA) and is written as

$$E_{XC}^{LSDA}[n^{\uparrow}, n^{\downarrow}] = \int d^3r n(\vec{r})\epsilon_{XC}(n^{\uparrow}, n^{\downarrow}). \tag{2.54}$$

The LSDA can be implemented using DFT which is termed local spin density functional theory (LSDFT). The LSDA can be described in terms of the up and down spin densities, but it is usually expressed in terms of the total charge density $n(\vec{r}) = n^{\uparrow}(\vec{r}) + n^{\downarrow}(\vec{r})$ and the local spin polarization $\zeta(\vec{r})$ as

$$\zeta(\vec{r}) = \frac{n^{\uparrow}(\vec{r}) - n^{\downarrow}(\vec{r})}{n^{\uparrow}(\vec{r}) + n^{\downarrow}(\vec{r})}. \tag{2.55}$$

One of the advantages of using the LDA and LSDA exchange-correlation is that they are not computationally demanding. The LDA and LSDA have been used to predict geometric structure and other properties of materials, but one major short fall the inability to accurately predict the electronic properties of semiconductor materials, most especially the band gap, which is severely underestimated, and defect charge state transition levels [19, 41, 42, 52].

2.5.2 The generalised gradient approximation (GGA)

The GGA goes beyond LDA by using not only the information about the density at a particular point $n(\vec{r})$, but also including the gradient $\bigtriangledown n(\vec{r})$. Within this ap-

proximation, the non-homogeneity of the true electron density is considered and the exchange-correlation functional is written as

$$E_{XC}^{GGA}[n] = \int n(\vec{r})\epsilon_{XC}(n(\vec{r}), \bigtriangledown n(\vec{r}))dr. \tag{2.56}$$

There are many forms of GGA functional that are used for different calculations. These include: PBE functional proposed by Perdew, Burke and Ernzerhof (PBE) [13], PBEsol which is a modification of the PBE for solids [53], Becke exchange [54], Lee-Yang-Parr (LYP) correlation [52, 54, 55] and Meta-GGA [54].

The generalised gradient approximation (GGA) exchange-correlation energy has been known generally to improve the prediction of the structural and electronic properties of some atoms, molecules, and solids compared to the LDA. The GGA functional has recently become popular in DFT calculations since it yields more accurate estimates for total energies [44, 45, 46, 47, 48] and barriers of chemical reactions [56] than LDA and LSDA. The GGA has been used to correctly predict the bulk elastic properties of several materials. One of the most significant advantages of the GGA over the LDA is the prediction of the correct ferromagnetism configurations of the ground state BCC iron [57]. The lattice constants calculated using LDA are in general 2% smaller than the experimental ones, while GGA improves this in most cases but often slightly overestimates the experimental values [19, 52].

Even though the true ground state energy of a given system can be approximated by DFT, DFT with GGA and LDA have some major shortfalls which include the underestimation of the band gap of semiconductors and insulators, and inaccurate weak Van der Waals attractions [58].

2.5.3 Hybrid functionals

The failure of both the LDA and GGA in predicting the band gap of several materials and the underestimation of the band gaps and other properties of charged defects in semiconductors materials [19, 20] has been rectified by hybrid functionals. Hybrid functionals have been very successful and accurate in the prediction of the band gap of several materials [19, 20]. The hybrid exchange-correlation energy functional $E_{XC}^{hyb}[n]$ is defined as

$$E_{XC}^{hyb}[n] = \alpha E_X^{HF}(\omega) + E_C^{GGA} - (\alpha - 1)E_X^{GGA}, \tag{2.57}$$

where E_X^{HF} is the exact non-local Hartree-Fock exchange energy, E_C^{GGA} and E_X^{GGA} are the semilocal GGA correlation and exchange functionals, respectively, α is a mixing parameter and ω is an adjustable parameter. Several hybrid exchange-correlation functionals recently developed include B3PW91, B3LYP [59, 60], PBE0, HSE03 and HSE06. The B3PW91 [54] was the first to be introduced in 1993, subsequently in 1994 and 1999, the B3LYP [59, 60] and PBE0 [61, 62], respectively were developed. Later in 2003, a new class of the hybrid exchange-correlation functional known as HSE was introduced by Heyd, Scuseria and Ernzerhof. The HSE03 [15] and HSE06 [63] screened hybrid functionals usually predict better results for the band gap[54] compared to other exchange-correlation energy functionals.

2.5.3.1 Hybrid functionals based on a screened Coulomb potential

The hybrid density functional with the Hartree-Fock exchange, has improved many GGA results. This improvement was as a result of the inclusion of the non-dynamical correlation which normally delocalized the GGA exchange hole [54, 63]. In solid-state physics and quantum chemistry, the screening of the Coulomb potential has been adopted to eliminate the divergence of the short range ($\frac{1}{r}$) potential [15]. The HSE hybrid functional addresses the effect of the short and long range potential by applying

the screened Coulomb potential to the exchange interaction in order to screen the long range part of the HF exchange. To address the last statement, the Coulomb operator was separated into two parts namely: the short range (SR) and the long range (LR) potential which are expressed as [64]

$$\frac{1}{r} = \frac{erfc(\omega r)}{r} + \frac{erf(\omega r)}{r}, \tag{2.58}$$

where $erfc(\omega r)$ is an error function, $\frac{erfc(\omega r)}{r}$ and $\frac{erf(\omega r)}{r}$ represent the SR and the LR parts of the potential, respectively. The $erfc(\omega r) = 1 - erf(\omega r)$ (is the complimentary error function and ω an adjustable parameter). If ω is adjusted to *zero*, the SR term becomes the full coulomb operator and the LR term becomes *zero*. The opposite is true when $\omega \longrightarrow \infty$.

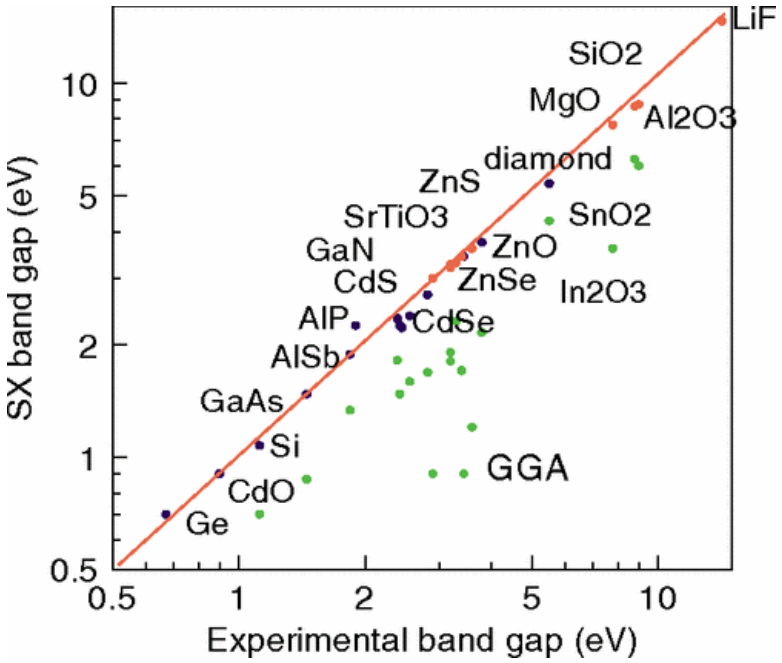

Figure 2.1: *A plot showing the experimental (red) and screened exchange (SX) theoretical band gap as predicted by the HSE (dark blue) and GGA-PBE (green). Reproduced with permission from Clark and Robertson [65].*

2.5.3.2 HSE06 hybrid functional

The mixing parameter for HSE06 is 25% which modifies the hybrid functional equation in Equation (2.57) to

$$E_{XC}^{HSE06} = 0.25E_X^{HF,SR}(\omega) + 0.75E_X^{PBE,SR} + E_X^{PBE,LR} + E_C^{PBE}. \tag{2.59}$$

The Perdew, Burke, and Ernzerhof (PBE) [13] is a unique version of the GGA. For the HSE hybrid functional, the optimal value of ω lies between 0.2 and 0.3 Å^{-1} [63]. The proposed 25% of the mixing parameter is to be adjusted to suite the type of system being investigated. Succinctly speaking, the 25% mixing parameter is not a generic feature for all systems. The 25% and 0.2 Å^{-1} mixing and adjustable parameters, respectively, which yield better thermochemical results and provides good accuracy for band gaps and lattice constants in solids [63] were used for all the results presented in this thesis. Figure 2.1 shows a comparison of the experimental and the calculated band gap of some materials. Table 2.1 shows the band gap values of materials as predicted by the LDA, GGA and HSE hybrid functionals.

Table 2.1: *The theoretical and experimental band gap results of some selected materials in eV.*

Material	LDA	GGA	HSE	Exp
Ar[c]	8.16	8.74	10.34	14.20
C[a]	4.11	4.21	5.42	5.48
Si[b]	0.61	0.61	1.17	1.17
Ge	0.00	0.00	0.80[e]	0.78[a]
AlN [c]	4.17	4.18	5.81	6.19
ZnO [c]	0.75	0.80	2.49	3.44
MgSe[b]	-	1.70	2.60	3.6[d]
MgTe[b]	2.26	2.34	3.01	3.47[d]
MgO[c]	4.70	4.68	6.67	7.83

[a]Ref [19], [b]Ref [48],
[c]Ref [66],[d]Ref [67, 68].
[e]With spin orbit interaction.

The HSE06 functional properly describes the electronic structure of all group-IV

semiconductors and also predicts highly accurate defect charge state transition levels [19]. In addition to the accurate prediction of semiconductor band gaps, the HSE has been used to accurately predict the electronic properties of materials with electrons that are highly localized. Examples are the rare earth elements that have highly localised f and d states in their valence shells [69, 70, 71].

2.6 Periodic boundary conditions

In order to use DFT to model the properties of real crystals or to calculate the bulk properties of solids, the problem of infinitely many electrons must be resolved. To address this problem, the periodicity of the solid crystal structure must be taken into account when solving the Kohn-Sham equation. In a real solid system, there are too many electrons and ions to model computationally. To solve this problem, the effective potential V_{XC} in the Kohn-Sham equation must be periodic and the one-particle wavefunction must also be written in the form required by Bloch's theorem.

2.6.1 Bloch's theorem

Considering the Hamiltonian $\hat{H}$ for a single particle in a potential $V(\vec{r})$ as

$$H = \frac{-\bigtriangledown^2}{2} + V(\vec{r}), \tag{2.60}$$

where $\bigtriangledown^2$ is the kinetic energy operator. Bloch's theorem [72] considers electrons subjected to a periodic potential $V(\vec{r})$ which is generated by the periodic structure of the solid. Bloch's theorem states that the one-particle wavefunction $\Psi_{(n,\vec{k})}(\vec{r})$ can be written as

$$\Psi_{(n,\vec{k})}(\vec{r}) = e^{i(\vec{k}\cdot\vec{r})} u_{(n,\vec{k})}(\vec{r}), \tag{2.61}$$

where $u_{(n,\vec{k})}$ is a function with the periodicity of the lattice, $\vec{r}$ is the position vector, the exponential term is the phase, $\vec{k}$ is the wave vector that is chosen in the first Brillouin zone due to the translational symmetry and n is the band index. The band index is a quantum number that corresponds to the appearance of independent eigenstates of different energies but with the same $\vec{k}$. An alternative formulation of Bloch's theorem, expressly showing the translational symmetry, is

$$\Psi_{(n,k)}(\vec{r}+\vec{R}) = e^{i(\vec{k}\cdot\vec{R})}\Psi_{(n,k)}(\vec{r}), \tag{2.62}$$

where $\vec{R}$ is a real space lattice vector. According to Equation (2.62), the eigenstates of $\hat{H}$ were chosen to associate with each Ψ a wave vector $\vec{k}$. Bloch's theorem has helped to reduce the infinitely many electron problem to an infinitely many k-point problem inside the Brillouin zone [73].

2.6.2 Energy cut-off

To deal with the problem of infinitely many k-points, plane waves are used to expand the periodic function $u_{(n,\vec{k})}$ in the form

$$u_{(n,\vec{k})}(\vec{r}) = \sum_{\mathbf{G}} C_{(n,\vec{k})}(\vec{G})e^{i(\vec{G}\cdot\vec{R})}, \tag{2.63}$$

where $\vec{G}$ is the reciprocal lattice vector defined through $\vec{G}\cdot\vec{R} = 2\pi m$ (m is an integer), $\vec{R}$ is a real space lattice vector and the $C_{(n,\vec{k})}$ are plane wave expansion coefficients. The electron wavefunctions can be expressed as a combination of an infinite number of discrete plane waves from a basis set and is given as [74]

$$u_{(n,\vec{k})}(\vec{r}) = \sum_{\mathbf{G}} C_{(n,\vec{k})}(\vec{k}+\vec{G})e^{i(\vec{k}+\vec{G})\cdot\vec{R}}. \tag{2.64}$$

If $E_n(\vec{k})$ is an energy eigenvalue, then for all reciprocal vectors $\vec{G}$, $E_n(\vec{k}+\vec{G})$ is an eigenvalue. The number of plane waves must be restricted since it is not possible to consider an infinite basis set. To restrict the number of plane waves, there must be an imposed upper boundary to the kinetic term of the plane waves. This imposed boundary is called the energy cut off E_{cut}, which is given as

$$\frac{|\vec{k}+\vec{G}|^2}{2} < E_{cut}. \tag{2.65}$$

2.6.3 Hellmann-Feynman theorem

The Hellmann-Feynman theorem [75, 76] or the force theorem states that the force on the atoms is given as in classical electrostatics

$$\mathbf{F}_i = \frac{\partial E_{tot}}{\partial \mathbf{R}_i} = -[\frac{\partial \langle\psi_i|H|\psi_i\rangle}{\partial \mathbf{R}_i} + \frac{\partial E_{ion}}{\partial \mathbf{R}_i}], \tag{2.66}$$

where R_i is the atomic position, ψ_i is the wavefunction of the Hamiltonian H. Equation (2.66) is the differential form of the Hellmann-Feynman theorem. The Hellmann-Feynman theorem is a useful tool in solid state and atomic physics. In quantum mechanics, the Hellmann-Feynman theorem allows a single way of defining a generalized force on eigenstates of the Hamiltonian, associated with the variation of some of its parameters. In order to avoid incurring errors that arise from the use of unconverted wavefunctions, this theorem should only be implemented once the wavefunctions are close to self-consistency since the force is not a variational quantity.

2.6.4 Self-consistent iterative process

In order to find the (local) minimum energy atomic configuration, a self-consistent total energy calculation is required and all the forces acting on the atoms must be minimized through geometric relaxation. The ionic forces are obtained using the Hellmann-

Feynman theorem [75, 76].

An iterative self-consistent approach is also required to calculate the electronic charge density. In this self consistent method, an initial trial electron density is used to calculate the effective potential V_{eff} and the exchange potential V_{XC}. In this process, the Kohn-Sham wavefunction equations are written in the form of a plane-wave basis set. After the Kohn-Sham equations have been solved, the electron density and total energy are computed and results displayed if converged to the required criteria. Otherwise, the effective potential due to the calculated electron density is used to find a new electron density therefore repeating the whole process until there is convergence. See Figure 2.2 for a flow chart illustrating the self-consistent iterative process.

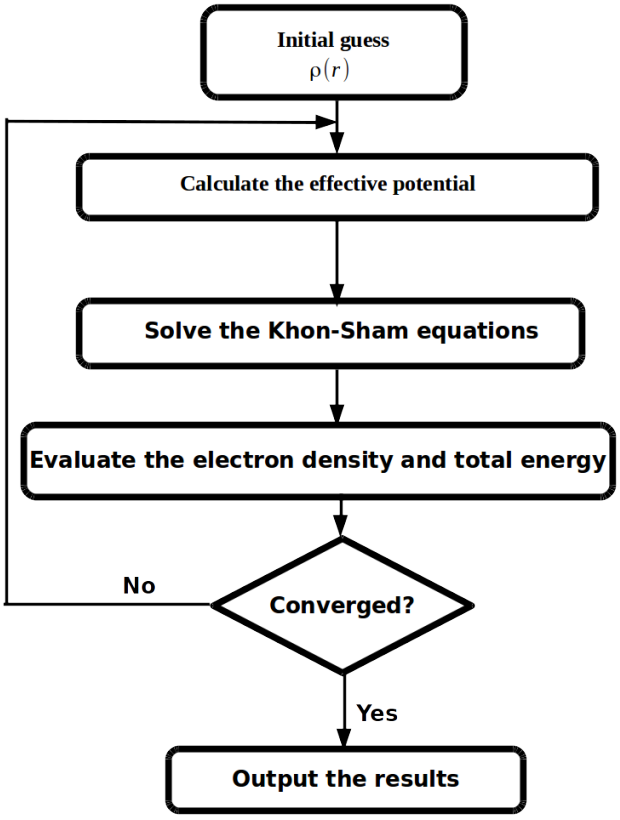

Figure 2.2: *A schematic flow chart illustrating the self consistent field calculation of the DFT.*

2.7 Pseudopotentials

Despite the simplification of the initial many-body problem, it is still computationally expensive to solve for a large system. Pseudopotentials are used to simplify the complexity surrounding the many-body problem of a large system [77]. The idea of the pseudopotential is to freeze the core-state (electrons in the nucleus) since the core electrons are not involved in chemical bonding [78]. Pseudopotentials are built to reproduce the true potential of the nucleus outside a sphere of a given radius, while inside the sphere, they are artificially smoothed as displayed in Figure 2.3.

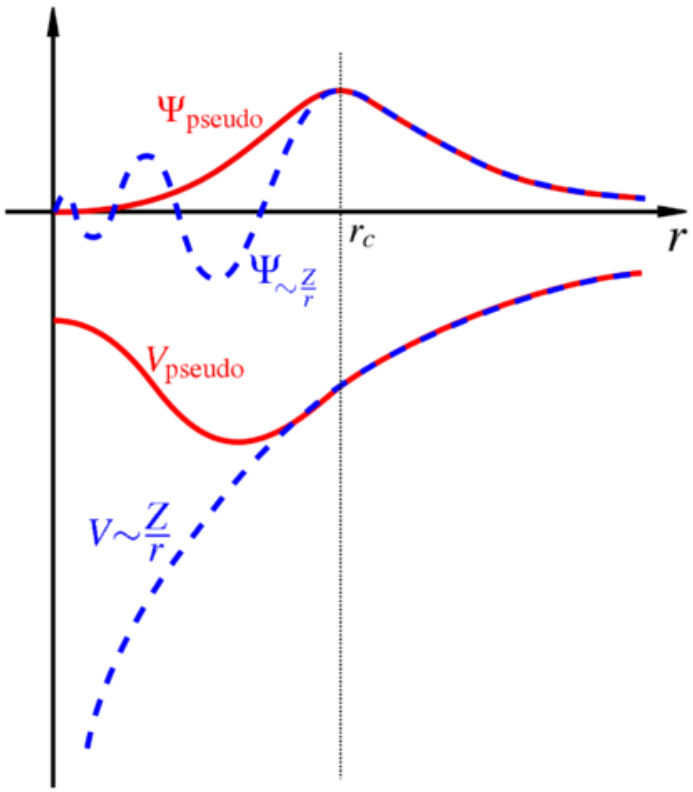

Figure 2.3: *A schematic illustration of the all electron potential $V \sim Z/r$ (dashed line). the pseudopotential V_{pseudo} (solid line) and their corresponding valence wave function ($\Psi_{V \sim Z/r}$) and pseudo-wave function (Ψ_{pseudo}). Reproduced with permission from Makov and Payne [79], and Schwerdtfeger [77].*

By using pseudopotentials, the core electrons are removed, a smaller plane wave

basis set is required and the potential does not go to ∞ as the centre of the nucleus is approached. The general procedure for generating the pseudopotential is as follows:

1. Choose the generation parameter (exchange-correlation potential) cut-off radius (r_c) as well as the valence-core configuration.
2. Choose the pseudopotential form to be used.
3. Then carry out an all-electron density-functional calculation for a reference atom.
4. Calculate the wavefunctions and eigenvalues for an initial set of chosen parameters (exchange-correlation potential) and then compare their values with the all-electron calculated values.
5. A self consistent pseudopotential is then generated only if the results of the eigenvalues and wavefunctions are all equal to those from all electron calculations. In a situation where the results are different, a new set of parameters is chosen and the wavefunction again is calculated for another set of chosen parameters.

By using the pseudopotentials, the core electrons are removed, a smaller plane wave basis set is required and the potential does not go to ∞ as the centre of the nucleus is approached.

2.7.1 The projector-augmented wave method

The projector-augmented wave (PAW) method was introduced by Blöchl in 1994 [80]. This method combines the advantages of the all-electron and pseudopotential method. The PAW method is based on the transformation between the pseudo wavefunction $\tilde{\Psi}_n$ and the exact all electron wavefunctions Ψ_n. The n appearing in Ψ_n, is the composite quantum number for the band, spin and **k**-point. The true or exact wavefunctions Ψ_n

are related to the pseudo wavefunctions $\tilde{\Psi}_n$ by a linear transformation [80]

$$|\Psi_n\rangle = |\tilde{\Psi}_n\rangle + \sum_i (|\Phi_i\rangle - |\tilde{\Phi}_i\rangle)c_i, \tag{2.67}$$

where i is the atomic index and c_i is the linear coefficient functional of the pseudo wavefunction which contains the set of projector functions. According to Equation (2.67), the exact all-electron wave function is expressed in three terms: the pseudo wavefunction $\tilde{\Psi}_n$, the Φ_i (a set of all electron partial waves), which is similar to the all-electron core state Ψ_n, and lastly, the $\tilde{\Phi}_i$ (a set of pseudo partial waves), which is similar to the pseudo core states $\tilde{\Psi}_n$. Advantages of the PAW are as follows:

1. There is no need to deal with the inert core electrons. Projector functions are localized inside the augmentation spheres.
2. The valence pseudo wave functions are smooth and without nodes inside the augmentation spheres, i.e $\Phi_i = \tilde{\Phi}_i$.
3. The PAW method provides access to full all-electron wave functions and electron density which is helpful for orbital-dependent exchange-correlation functionals.

2.8 Brillouin zone sampling

Under periodic boundary conditions, the Kohn-Sham orbitals are evaluated at a point **k** within the Brillouin zone (BZ). A **k**-point is a reciprocal lattice vector used to label an eigenstate (an electronic level), and it represents a position in the first BZ of a solid system [81, 82]. Under periodic boundary conditions, it is mandatory to convert the integral over the BZ into a summation over a set of discrete points of **k**-space. An integral function $F(r)$ over the BZ can be expressed as [82]

$$F(r) = \frac{V_{cell}}{(2\pi)^3} \int_{BZ} f(k)d\vec{k} = \sum_i \omega_i f(k)d\vec{k}, \tag{2.68}$$

where V_{cell} is the unit cell volume, $f(k)$ is the Fourier transformation of $F(r)$ and ω_i is the weighting factor. The generation of an optimal set of k-points for both periodic and aperiodic systems has already been reported [83]. When dealing with defects in semiconductors, especially those that involve charged states and charge transfer within a defect system, a large supercell is needed to avoid defect-defect interaction. For such a system, the volume of the BZ (V_{BZ}) is related to the volume of the supercell (V_{Scell}) by

$$V_{BZ} = \frac{(2\pi)^3}{V_{Scell}}. \tag{2.69}$$

For large supercells, the BZ volume is small, and consequently, less **k**-points are needed to sample it. In the results of this thesis, $\mathbf{k} = 0$ (which is called Γ (gamma) point sampling) was used to sample the BZ in addition to the Monkhorst-Pack (MP) [73] **k**-points spacing. The MP **k**-mesh is a set of **k**-points generated in an evenly spaced (k_x, k_y, k_z) grid spread through the BZ. For more accurate results, the crystal lattice, the space group symmetry and the supercell size play a major role in determining the choice of the MP **k**-mesh to be used.

Chapter 3

Theory of defects

3.1 Introduction

This chapter focuses on crystal structures and the theory of point defects and impurities in semiconductors. In Section 3.2 and Section 3.3, crystal structures and electronic properties of solids are discussed. Interstitials, vacancy and impurities, which are examples of point defects, are discussed in Section 3.4. A brief discussion of defects in semiconductors is presented in Section 3.5. Other properties of defects in semiconductors (such properties as metastability, negative-U and optical properties) are discussed in Section 3.6. In Section 3.7, this thesis focuses on the history and recent development of Ge as a semiconductor material. Finally, point defects observed in Ge and their importance towards the development of Ge-based microelectronics material technology are discussed in Section 3.8.

3.2 Crystal structure

Atoms in a perfect crystal are orderly arranged. Atoms are located at a unique specified sites known as the ***lattice points***, which form a regular periodic structure. To reproduce the whole perfect crystal structure a primitive unit cell is defined, which

is the smallest volume that is periodically translated to reproduce the whole crystal structure [72]. For Ge, there is one predominant crystal structure, a diamond like 3D structure with tetrahedrally coordinated atoms, which can be characterized as sp^3 hybridized [84]. A schematic diagram of diamond structure of Ge is shown in Figure 3.1. The physical dimensions of a unit cell in a three-dimensional lattice are called the lattice constants referred to as a, b, and c. In the case of a cubic crystal structure, for example zincblende, all the constants are equal, i.e $a = b = c$.

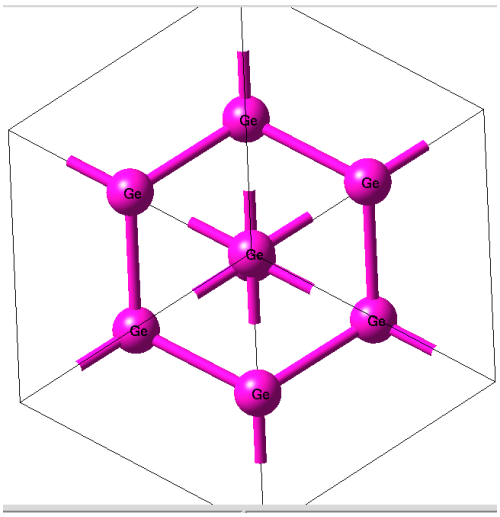

Figure 3.1: *A schematic diagram of a unit cell showing the diamond structure of Ge.*

3.3 Electronic properties of a solid

Band structure and total density of states (DOS) are plotted to study the electronic properties of pure, doped and semiconductors with defects. Primarily, the electronic properties of a solid such as the band gap and the DOS play an important role in the selection of a good semiconductor material such as Ge [3]. For the electronic band structure, the key properties are the effective mass of the charge carriers and the band gap [21, 22]. In a band structure, the region between the valence band maximum (VBM) and conduction band minimum (CBM) is called the band gap. There are no

state in the band gap if the material is free from defects see Figure 3.2.

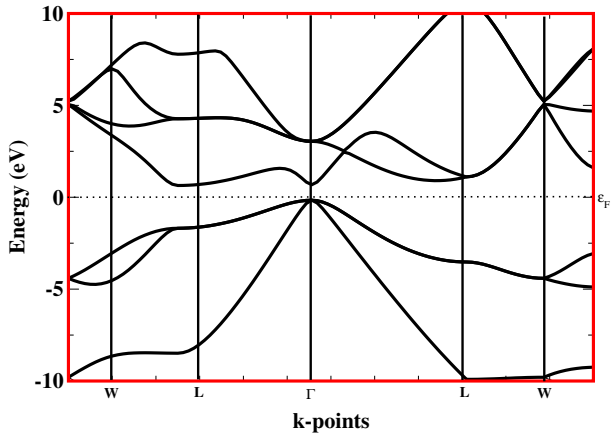

Figure 3.2: *A schematic diagram of electronic band structure.*

The band gap is direct if the valence band maximum and the conduction band minimum are located at the same electron wavevector (**k**), as shown in Figure 3.3. An

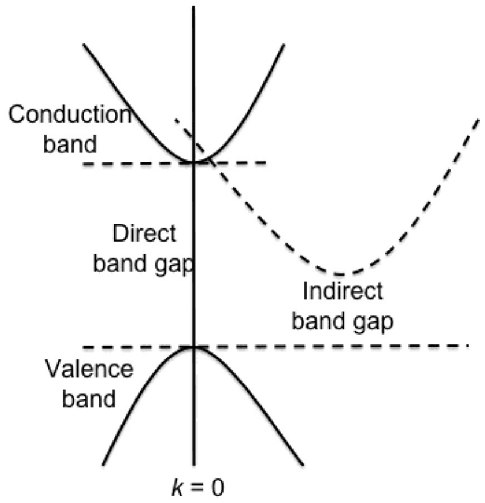

Figure 3.3: *Diagram showing direct and indirect band gap of a semiconductor material. Reproduced with permission from Singh [85].*

indirect band gap means that a phonon is required to effect the change in the **k**-vector required to transfer an electron from the VBM to the CBM (or vice versa). [86]

3.3.1 Band gap of germanium

The band gap of Ge has been studied both experimentally and theoretically. The band gap of Ge at 300 K and 0 K are 0.67 and 0.78 eV [87, 88], respectively. Before the introduction of HSE hybrid functionals, DFT incorrectly predicted the band gap of Ge when using the GGA or the LDA. By using the GGA or LDA, Ge was predicted to be semi-metal (having no band gap) [19, 89]. However, HSE hybrid functionals correctly predict the band gap of Ge [19] (see Figure 3.4). Several reports on the band gap energy of Ge as predicted by HSE hybrid functionals which were in agreement with the experimental band gap at 0 K have been published [90, 91, 92, 93, 94].

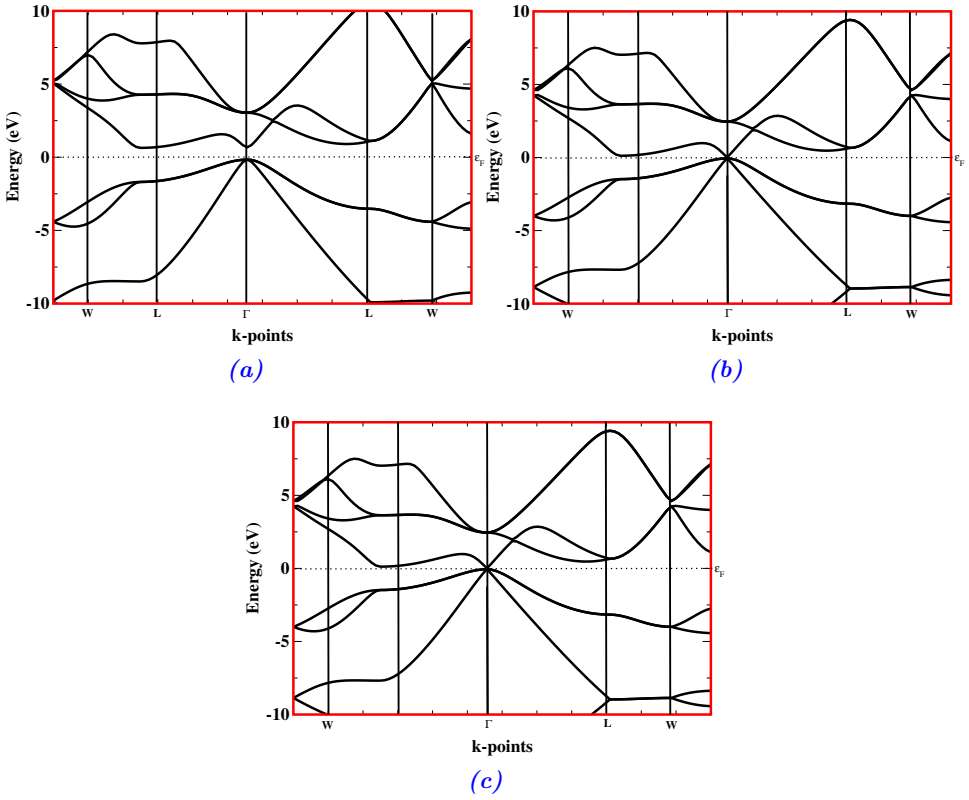

Figure 3.4: *A schematic diagram of band structure of Ge without spin-orbit coupling as predicted by (a) HSE hybrid functional, (b) GGA and (c) LDA.*

3.4 Defects

The quality of a Ge based device depends on the amount of impurities and the number of lattice defects of the crystal. However, in reality there is no crystal that is defect free. Defects occur in many solid-state materials such as semiconductors, metals or insulators [95, 96]. In this thesis, point defects in Ge, a semiconductor, is the main subject of interest.

3.4.1 Classification of defects

In crystalline solids, the crystal accommodates a large number of different kinds of defects. The nature and equilibrium concentration of a defect depends primarily on the temperature, pressure and composition of the system, imposed during the annealing or curing process. Imperfections are usually classified as extended defects or point defects. Both defect types influence the properties of a semiconductor.

3.4.1.1 Extended defects

Extended defects are usually classified by the number of dimensions in which they are extended. These include the atomic size, volume, surface and line defects [95].

1. **Line defects:** A dislocation is an example of a line defect. It occurs when atoms of the crystal lattice are misaligned. Figure 3.5 shows an example of dislocation. Dislocations are used to explain the unexpectedly low critical resolved shear stress in which single crystals of metal undergo permanent or plastic deformation.

2. **Volume defects:** Any volume differing in structure, composition, orientation from the rest of the crystal matrix is a volume defect.

3. **Surface defects:** Surface defects which are also called area defects are free surfaces or interfaces between distinguishable volumes. The interfaces surround-

ing all types of defects are also known as surface defects, e.g. twin and domain boundaries. For more information on extended defects see Crawford (2013) [96]

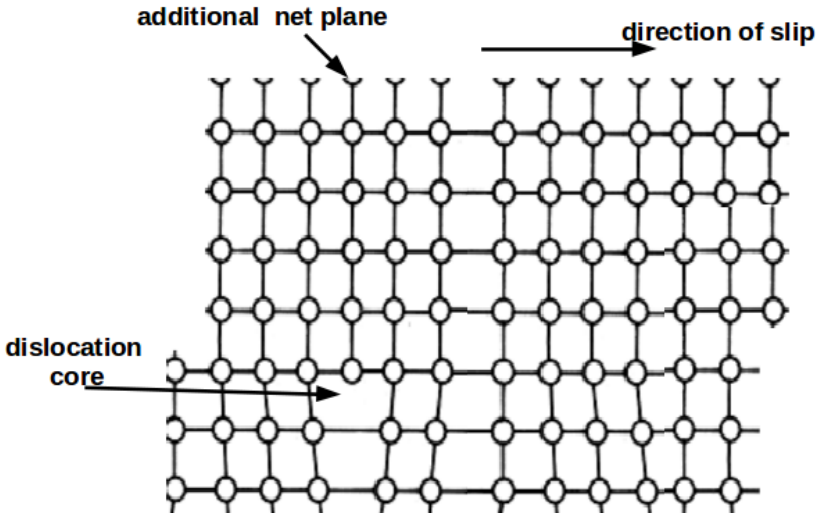

Figure 3.5: *Example of extended defects (dislocation).*

3.4.1.2 Point defects

Point defects occur in most semiconductor materials, including Ge. Point defects in a material changes the ordered crystal pattern at a specific isolated site, and they are classified in two types namely: the extrinsic and intrinsic point defects [97].

1. **Extrinsic point defects:** The extrinsic point defects are atoms different from the host, which are called solutes if they are purposely added to the material. These different atoms are equally called impurities if they are not deliberately added to a material. These different atoms may reside on a lattice site, in which case it is called a substitutional solute (or impurity) or it may occupy an interstitial site, in which case it is called an interstitial solute. A schematic diagram showing the different extrinsic and intrinsic point defects is shown in Figure 3.6.

2. **Intrinsic point defects:** An intrinsic point defect is formed when an atom is

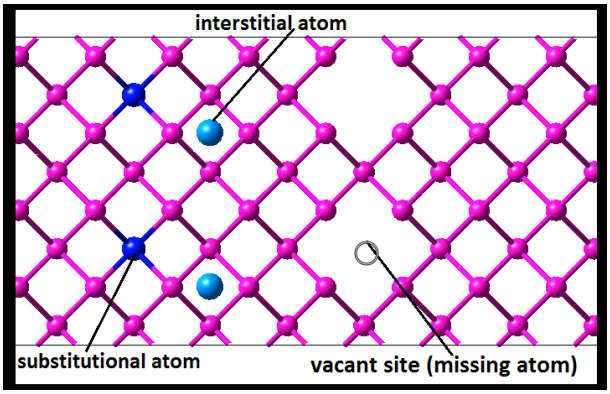

Figure 3.6: *A schematic diagram of point defects, showing interstitial atoms, substitutional impurities and vacancies.*

missing from a position that ought to be filled in the crystal, creating a vacancy, or when an atom occupies an interstitial site where no atom would ordinarily appear, causing an interstitial. In Ge, interstitial point defects are known to form with higher formation energy than vacancies [90]. Vacancies, on the other hand, are present in a significant concentration in Ge. For an atom to move easily from one crystal lattice site to another, it is required that the target site must be vacant. Concentrations of the Ge vacancy influences the rate of diffusion of impurities [98, 99, 100]. A defect that involves paired vacancies on the cation and anion sublattices is called a **Schottky defect**. When the defect consists of a pair of interstitial and vacancy defects, it is called a **Frenkel defect**. Another kind of intrinsic point defect is the **anti-site defect**. The anti-site defect, occurs in a compound whose atoms are less strongly ionized and it becomes energetically possible for species to exchange sites, so that an X-atom is placed on the Y-atom sublattice or Y-atom placed on the X-atom sublattice. In addition, combinations of these simple point defects are often possible, e.g., V_{Ge}-V_{Ge} (*di*-vacancies), Tm_{Ge}-V_{Ge} vacancy-substitutional pairs, N_{Ge}-V_{Ge} vacancy-impurity pairs, or even more complex defects.

A schematic diagram of a point defect is shown in Figure 3.7, which depicts *di*-interstitial in Ge. In this Ge *di*-interstitial, two Ge atoms were added to the pure crystal structure.

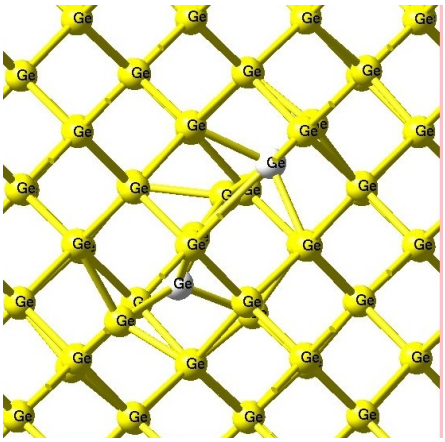

Figure 3.7: *A schematic diagram of a Ge di-interstitial. This crystal structure contains two Ge interstitial atoms at the tetrahedral and split*[110] *sites.*

3.4.2 Bulk defects

Another type of defect is the bulk defect, these defects are regions which normally consist of a combination of both the line and the point defects. This thesis will not consider on bulk defects, for more information on these kind of defects see Ref [3].

3.5 Defects in semiconductors

Crystalline semiconductor solids accommodate a large number of defects as mentioned earlier. The concentration and nature of defects depend primarily on the temperature, pressure as well as the composition of the system [3, 97]. Defects, which under normal conditions, are generally categorized into point defects, line defects, planar defects and bulk defects have the tendency to influence the mechanical, transport, electrical, electronic, thermodynamic and optical properties of semiconductors [3, 48, 69, 92]. Defects can influence a semiconductor material negatively, for example some defects act

as recombination centres [95, 97]. Defects can also influence semiconductor material positively which in turn enhances the material performance, for example the p- or the n-type doping which are responsible for the change of the majority carrier type [95, 97]. Point defects in Ge have been intensively studied theoretically and experimentally [3]. However there are still major unexplored point defect interactions which influences the electronic, thermal and optical properties of Ge. Specifically, little work has been done on systems that involve charged states and charge transfer.

3.5.1 The Fermi energy

The Fermi energy (ε_F) is defined with reference to the VBM [101], and usually lies between the VBM and the CBM i.e, $\mathrm{E_V} < \varepsilon_F < \mathrm{E_C}$. Mathematically, the ε_F is expressed as

$$\varepsilon_F = \mathrm{E_V} + \triangle\varepsilon_F, \tag{3.1}$$

where $\mathrm{E_V}$ is the energy level of the VBM, $\mathrm{E_C}$ is the energy level of the CBM and $\triangle\varepsilon_F$ is the position of the Fermi level above the valence band.

3.5.2 Chemical potential

The chemical potential (μ) describes the energy required when atoms are taken from or returned to atomic reservoirs to build or change a crystal structure [101, 102]. The chemical potential is the partial derivative of the Gibb's free energy with respect to the number of atoms. The μ of a specific element can be obtained from the energy of the most stable structure of the pure element. For a supercell of N atoms of Ge and total energy, $E^{tot}(Ge)$, the chemical potential of Ge is found as

$$\mu_{\mathrm{Ge}} = \frac{E^{tot}(Ge)}{N}. \tag{3.2}$$

3.5.3 Defect concentrations

In a "dilute regime" in which defects do not interact with each other, defects require energy to form. According to the Boltzmann distribution, the concentration (C) of defects in a crystal is given by [102, 103]

$$C = N_0 \exp(- \triangle G/k_B T), \tag{3.3}$$

where k_B and T are the Boltzmann constant in eV/K and the temperature in Kelvin, respectively. The number of possible defect sites is N_0 (per bulk quanta) and $\triangle G$ is the change in the Gibbs free energy of the system. $\triangle G$ is expressed as

$$\triangle G = \triangle E + P \triangle V - T \triangle S, \tag{3.4}$$

where $\triangle E$, $\triangle V$, P, T and $\triangle S$ are the change in total energy (energy of formation), change in volume, pressure, temperature and change in entropy, respectively. Because the $\triangle V$ and $\triangle S$ are negligible for most crystalline solids at moderate temperature and pressure, the Gibbs free energy of the system may be approximated by the formation energy E^f ($\triangle G \approx \triangle E = E^f$). Equation (3.3) can now be written as

$$C = N_0 \exp(-E^f/k_B T). \tag{3.5}$$

According to Equation (3.5), an increase in formation energy leads to a decrease in the concentration of the defects. Furthermore, this implies that high formation energy will lead to low concentration of the defect.

3.5.4 The formation energy

The formation energy is defined as the energy which is required to form a defect from its component atoms taken from chemical reservoirs of pure elements [102, 103]. The

concentration (C) of defect in thermodynamic equilibrium is related to the formation energy (E^f) through the Boltzmann constant, see Equation (3.5). For a charged defect, E^f also depends on Fermi energy (ε_F). E^f of defects are derived directly from total energies, allowing the calculation of equilibrium defect *concentration* [103]. To calculate the defects formation energy, the total energy $E(d, q)$ for a supercell containing the optimized defect d in its charge state q must be determined. The defect formation energy $E^f(d, q)$ is given as [103, 104]

$$E^f(d, q) = E(d, q) - E^{tot}(pure) + \sum_i \triangle(n)_i \mu_i + q\varepsilon_F, \tag{3.6}$$

where $E^{tot}(pure)$ is the energy of a supercell without a defect, $\triangle(n)_i$ is the difference in the number of constituent atoms of type i in the defect and pristine supercell ($\triangle(n) < 0$, when an atom is added and $\triangle(n) > 0$ when an atom is removed) and μ_i is the chemical potential of the atom.

3.5.5 The defect charge states

Charged defects may be investigated by either removing or adding of electrons to the defect. Defects charge states can assume $+1$, $+2$, $+3$ when one, two, three electrons are removed from the valence shell, respectively, or -1, -2, -3 when one, two, three electrons are added to the valence shell of the defect, respectively. In this report, the charge states of defects considered were limited from -2 to $+2$ as other states were not found within the thermodynamically accessible region.

3.5.6 Thermodynamic transition energy (electrical levels)

Point defects are known to increase the internal energy and the entropy of crystals because of the number of ways the defect atoms can be distributed on lattice positions. At any temperature above the 0 K, the free energy will be minimum for a defect

concentration which is determined by the balance of the entropy and energy contributions [101, 102, 103]. This method requires a special calculation of the energy needed to add electrons to (electron affinity) or take away electrons from (ionisation energy) a defect [105]. Lany *et al* [101] evaluates a unique method of calculating the ionization energy (I_A) and the electron affinity (E_A). The I_A is mathematically expressed as

$$I_A = E_0^N - E_{+1}^N, \tag{3.7}$$

while the E_A is expressed as

$$E_A = E_{-1}^N - E_0^N, \tag{3.8}$$

where E_q^N (for q=−1, 0, +1) is the total energy of a perfect cell with charge state q containing N number of atoms. The electrical levels of a defect corresponds to the positions of the Fermi energy at which a charge state change occurs is referred to as charge state transition energy level $\epsilon(q/q')$. The defect charge state transition level is the Fermi energy for which the formation energy of charge state q and q' are equal and is given by [102, 104]

$$\epsilon(q/q') = \frac{E^f(d,q;\ \varepsilon_F = 0) - E^f(d,q';\ \varepsilon_F = 0)}{q' - q}. \tag{3.9}$$

3.5.7 The binding energy

The binding energy E_b is defined as the energy required to split up a defect cluster into well separated non-interacting defects [94, 106]. This can be expressed mathematically:

$$E_b = E_A^f + E_B^f - E_{AB}^f, \tag{3.10}$$

where E_A^f, E_B^f and E_{AB}^f are the formation energies of defect A, B and AB. Equation (3.10) could be interpreted as the reduction in energy of the bonded structure

with respect to the isolated components. Positive E_b implies that the defect is stable and can not without formation energy input be separated. The binding energies of some complexes as well as vacancy complex in Ge are shown in Table 3.1.

Table 3.1: *Table showing calculated results of binding energies of impurity and vacancy (V) complexes in Ge.*

Defects	Binding energy (eV)
BV	−0.33
CV	0.07
PV	0.52
CBV	0.11
CVAs	0.66
CVP	0.60

These results where taken from Ref [107].

3.5.8 Defects energy levels

1. **Acceptor and donor levels:** Point defects are intentionally added to semiconductors,in order to help control the type and concentration of charge carriers. An **acceptor** level is formed by electron deficient solutes which cause holes in the valence shell of the constituent atoms. Solutes with an excess of electron are called **donors**. While transition levels of the type $\epsilon(+2/+1)$ and $\epsilon(+1/0)$ are donors, the transition levels of the type $\epsilon(0/-1)$ and $\epsilon(-1/-2)$ are called acceptors.

2. **Shallow and deep levels:** Intrinsic point defects in semiconductors can be grouped according to the localized band gap states that they form. States that have energies close to either the CBM or the VBM are called shallow levels. If a defect is likely to be thermally ionized at room temperature, it is conventionally referred to as a shallow level. Transition states with energies far away from both the CBM and VBM are referred to as deep levels. In addition, a deep level could be expected when a wave function is localized on a length scale of an atomic bond. A good example of shallow defects are impurities with (shallow) donor or (shallow) acceptor states, due to the loosely bound electron or hole around them.

Figure 3.8 and Figure 3.9, show schematic diagrams of both the shallow and deep levels of a given defect charge state transition levels. Defects that can act both as donors and acceptors are called amphoteric

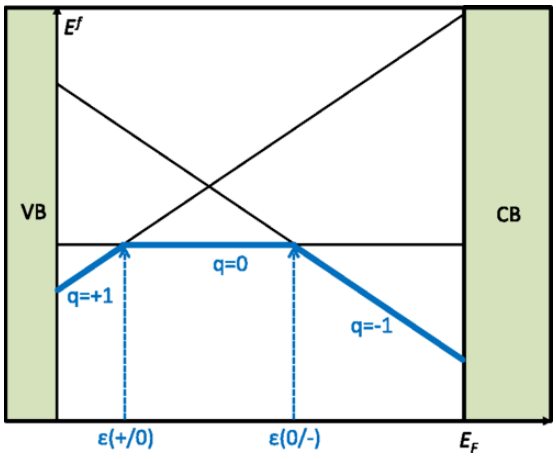

Figure 3.8: *A schematic diagram showing plot of formation energy and the Fermi energy of a defect in charge state +1, 0 and −1. The solid lines represent the* E^f *as defined in Equation* (3.6)*. In this illustration, the defect induced two charged state transition levels; a deep donor and acceptor at* $\epsilon(+1/0)$ *and* $\epsilon(0/-1)$*, respectively. The thick blue lines indicate the thermodynamically stable charge state for a given Fermi energy. Reproduced with permission from Freysoldt and co-workers [104].*

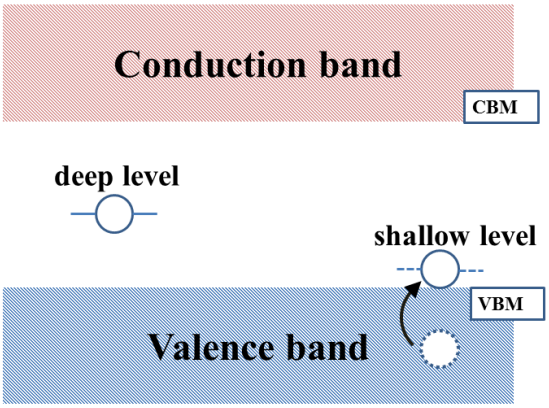

Figure 3.9: *A schematic diagram showing the positions of both shallow and deep electrical levels within the band gap. Adapted from Ref [66].*

3.6 Other properties of defects in semiconductors

3.6.1 Metastability of defects

A defect or defect complex is said to be metastable when the defect or defect complexes, has in at least one charge state, more than one different atomic configurations (configuration A and B) that are stable at local minima. Where one configuration (say configuration A) is the minimum energy in a particular charge state, and the other configuration B is stable in a different charge state, the phenomenon is referred to as charge state controlled metastability. Here the transformation between two or more configurations is controlled by an energy barrier and the processes are fully reversible.

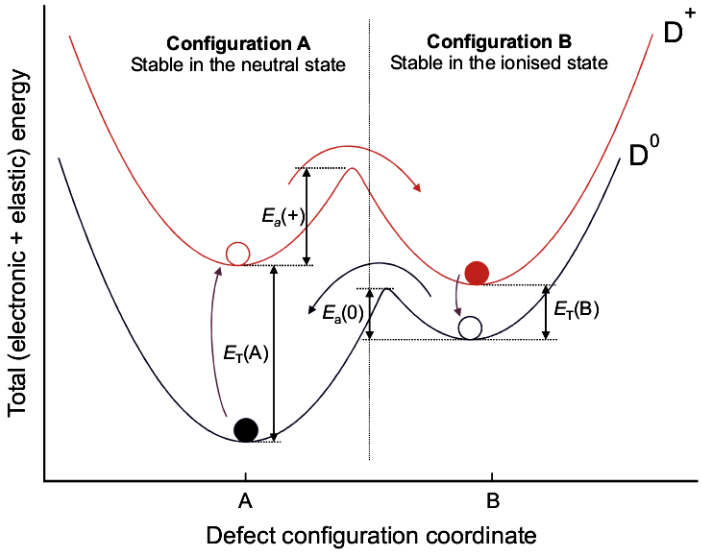

Figure 3.10: *Schematic diagram of defect metastability in semiconductors. Source Ref [108].*

Charge state controlled metastability suggest that even though two different configurations of the same defect type had the same number and type of atoms, the stability of one configuration over the other is charge-state dependent [109, 110, 111]. If a defect can only change in two different configurations, the defect is regarded as a bistable

defect, but in a situation where the defect can change in more than two configurations, it is regarded as a multistable defect [110, 111]. Figure 3.10 shows a schematic configuration coordinate diagram of a metastable defect, where in configuration A the defect is stable in the neutral state and in configuration B the defect is stable in the ionised state.

3.6.2 Negative U

In a three level system, it is expected that, due to Coulomb interaction between the electrons, the first ionisation energy would be less than the second ionisation energy. This difference is referred to by the quantity U. The effective-U (U^{eff}) parameter is the energy difference between two consecutive transition levels [104]. Mathematically, the U parameter is defined as

$$U^{eff} = \mathrm{E}^{\mathrm{f}}{}_{q+1} + \mathrm{E}^{\mathrm{f}}{}_{q-1} - 2\mathrm{E}^{\mathrm{f}}{}_{q}, \tag{3.11}$$

where $\mathrm{E}^{\mathrm{f}}{}_{q}$ is the formation energy of a defect in its charge state q at $\varepsilon_F = 0$. If the $U^{eff} < 0$, the U^{eff} is called a negative-U.

This negative-U occurs as a result of large lattice distortion during atomic relaxation of a particular system. This means that $q = 0$ state becomes thermodynamically unstable against the formation of $q = +1$ and $q = -1$ charge states.

3.6.3 Optical transition energies of a defect

The calculation of different charge state transition levels can be related to the optical transition properties of a defect. Figure 3.11 illustrates schematically, the states involved in the photoluminescence processes associated with a defect.

3.6.3.1 Photoluminescence properties

An excited state can be produced by removing an electron from the VBM to the CBM, in which a hole is left behind to relax into a defect state [112, 113, 114]. Consider the lowest energy of a defect E($V^x D^y C^0$) in its equilibrium neutral state with fully occupied x valence electrons in the outer shell with y defect electron levels and an empty conduction band. With an energy cost E_{abs}, the defect is excited by removing an electron from the defect state to the CBM [113, 114, 115, 116]. At this point the defect is in its excited configuration E($V^x D^{y-1} C^1$) (upper curve of Figure 3.11).

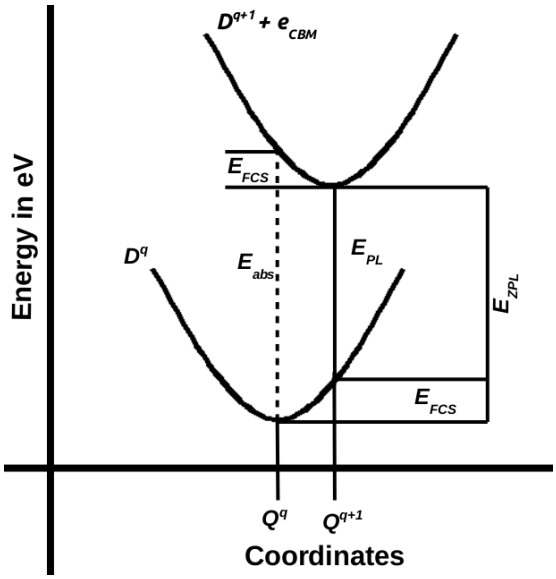

Figure 3.11: *Configuration coordinate diagram illustrating the optical transition properties of a defect.*

After this process, the system relaxes via phonon emission and the energy shift associated with this kind of relaxation is called the Franck-Condon shift (E_{FCS}) [115, 116, 117]. The defect in its excited state can make a radiative transition to the ground state resulting in a photoluminescence process with an emission energy (E_{PL}). After the transition, the defect relaxed via phonon emission to its true ground state. The true ground state is reached after phonon emission [114]. The zero-phonon line (E_{ZPL}) is the

transition energy associated with the luminescence process with no phonon emission. The E_{ZPL} can be defined mathematically as

$$E_{ZPL} = E(V^x D^{y-1} C^1) - E(V^x D^y C^0), \tag{3.12}$$

according to the definition of E_{PL}, the exciton binding energy is defined mathematically [114] as

$$E_b = E_{gap} - E_{ZPL}, \tag{3.13}$$

where the E_{gap} is the band gap energy. The Franck-Condon energy is usually calculated as

$$E_{FCS} = E_{abs} - E_{PL}. \tag{3.14}$$

3.7 Brief history of germanium

Germanium which was isolated from a rare mineral called argyrodite (Ag_8GeS_6) was discovered in Germany in 1885 by Clemens A. Winkler. Ge is classified as a metalloid, because it possesses both metal and non-metal properties. Ge has a unique characteristic of transparency to near infrared electromagnetic radiation wavelength between 1600-1800 nm [3, 118, 119]. Ge has a high refractive index and low optical dispersion [119]. The first research on the electrical properties of Ge started in the 1920s. During this period, Ge was used in rectifying diodes in microwaves radar receivers during World War II. In 1947, Ge rose to new commercial and industrial application importance. Ge was used by J. Bardeen [118] to produced an electronic transistor. Subsequently, transistors made of Ge were used to manufacture telephones, computers, hearing aids and radios. Things began to change in 1954 when it was discovered that Ge based transistors have the tendency to fail at high temperature, and then Silicon began to replace Ge. But silicon had a major deficiency because of its high impurity

level (the technology at that time was able to produce Ge at a higher level of purity compared to Si). Due to the high level of purity of Ge compared to Si, Ge was use in the SiGe substrate in photovoltaic cells (PVCs) which were in high demand.

Germanium's future looks bright due to its efficiency in solar technology because cadmium-indium-gallium-selenium (CIGS) can be substituted by Ge. Ge also can be substituted for Si in certain electronic applications because of its narrow band gap and high electron-hole mobility [1, 118, 119]. The application of germanium (Ge) as a promising material for complementary metal-oxide semiconductor (CMOS) technology is attracting attention due to its narrow band gap, high carrier mobility and low voltage operation [120, 121]. Table 3.2 shows the summarized electronic, physical and mechanical properties of Ge. In the next Section 3.8, the properties of various well known defects studied and their electrical levels in Ge are discussed.

Table 3.2: *Table showing electronic, mechanical and physical properties of Ge. Unless otherwise stated the properties of Ge were measured or calculated at 300 K.*

Basic Parameters	quantities	
Physical properties	crystal structure	diamond
	period and group	4
	Atomic number	32
	group of symmetry	O_h^7-Fd3
	number of atoms in 1 cm^3	4.4×10^{22}
	Auger recombination coefficient	10^{-30} cm^6/s
	Debye temperature	374K
	density	5.3234 g/cm^3
	dielectric constant	16.2
	electron affinity	4.0 eV
	lattice constant (experiment*)	5.658 Å
Mechanical properties	bulk modulus	7.5×110^{11}dyn cm^{-2}
	density	5.323 g cm^{-3}
Electronic properties	band gap experiment	0.66 eV (0.78 eV at 0 K)
	band gap modelled	0.78 eV at 0 K
	electron configuration	$[Ar]3d^{10}4s^24p^2$
Other properties	melting point	937°C
	infrared refractive index	4.00

*(In agreement with modelled result). These data where taken from Refs [122, 123, 124, 125, 126].

3.8 Defects in germanium

The focus of this section will be the discussion of results of previous studies of point defects in Ge. This section presents brief experimental highlights and concise DFT theoretical modelling results of point defects in Ge.

As mentioned earlier, typical point defect are the *self*-interstitial (I_{Ge}), vacancy (V), vacancy-complexes and substitutional impurities. All these point defect types in Ge have previously been studied using well known experimental or theoretical techniques. Recently, a number of papers have investigated the important point defects and metal related point defects [3, 127, 128, 129, 130, 131] in Ge. Various theoretical investigations [89, 100, 92, 132] have attempted to explain experimental results on process induced defects[3, 4, 130, 133], radiation induced defects [8, 128, 129, 131] and grown-in defects [132, 131] in Ge. The first experimental observation of I_{Ge} was by means of perturbed angular correlation spectroscopy (PACs) [9] after electron irradiation of Ge. Experimental studies revealed that Ge self-interstitial (I_{Ge}) occurs at a low formation energy but with lower concentration than the Ge vacancy (V_{Ge}) [134, 105]. This implies that V_{Ge} forms with a lower formation energy than the I_{Ge}. In addition to the lower formation energy of the V_{Ge}, the V_{Ge} mediates the diffusion of both the *p*- and *n*-type dopants in Ge [135, 136, 137].

By using various theoretical approaches such as DFT with LDA, GGA, LDA+U, GGA+U and hybrid functional of HSE, modelling of important results of point defects in Ge has been achieved. By using the GGA, Spiewak *et al.* [89] reported that the I_{Ge} exist in three different configurations. The hexagonal (H), the tetrahedral (T) and the split[110] dumbbell configurations. The split[110] configuration of the I_{Ge}, which is the energetically most favourable configuration, forms an acceptor level located at $E_V + 0.45$ eV [89, 138]. On the other hand, the tetrahedral configuration of I_{Ge} acts as a donor at $E_V + 0.11$ and $E_V + 0.46$ eV for the (+2/+1) and (0/+1) transition

levels [89, 139], respectively. *Self*-interstitial reflection by Ge surfaces has also been proposed [140] and recently, in a theoretical study, interstitials in Ge were found to be bistable having a double donor when at a cage site, without any trace of an acceptor [98].

Several theoretical investigations of vacancies in Ge (V_{Ge}) have been reported in literature. According to Spiewak *et al.* [134, 105] V_{Ge} in Ge induces a single acceptor $\epsilon(0/-1)$ level at 0.02 eV above the E_V and double acceptor $\epsilon(-/-2)$ level at 0.26 eV. This result differs form the result of Fazzio *et al.* [134, 105, 141] who found the same acceptor levels but at different energies, due to Fazzio *et al.* using a probably less appropriate pseudopotential. Haesslein *et al.* [9] studied both point defects in electron-irradiated Ge using PACs. They found two defect levels, one lying at E_V+0.20 eV which was attributed to the mono-vacancy acceptor state and the other, lying at $E_C - 0.04$ eV, was assigned to a donor state of the I_{Ge}. The DLTS results of Zistl [142], which revealed a level at 0.33 eV above the valence band, was also associated with the mono-vacancy acceptor state. One can conclude that V_{Ge} lies somewhere between 0.20 and 0.33 eV above the top of the valence band. Haesslein *et al.* [9] concluded that the defect lying at $E_V + 0.20$ eV corresponds to the $\epsilon(0/-1)$ transition state of the V_{Ge}. Recently, in order to improve the results of the V_{Ge} already reported by Spiewak *et al.* [134, 105], the same authors carried out a HSE calculation of the V_{Ge}. In contrast to previous results, HSE06 calculation suggests that the V_{Ge} displays multiple acceptor levels located in the upper half of the band gap [90]. Recently, Weber *et al.* [91] used HSE hybrid functional to investigate the role of dangling bonds (DB) and vacancies in Ge. They found that the DB in Ge has no levels in the band gap since the only acceptor $(0/-1)$ level was present below the VBM. Furthermore, it was found that the V_{Ge} has a much lower formation energy than the V_{Si}, and is stable in a number of charge states [138, 143].

Another type of point defect in Ge that has been reported in literature is the *di*-vacancy and *multi*-vacancy. [19, 92, 144] The di-vacancy $V_{2(Ge)}$ has been studied

previously using both an *ab initio* method and experimental techniques. But despite the numerous theoretical and experimental breakthroughs made in the study of *di*− and *multi*−vacancies, their properties and identification are still the subject of some controversy. The results reported by Janke *et al.* [136] revealed a pair of electron traps at $E_C-0.35$ eV and E_C- 0.32 eV, which anneal at 150°C and are attributed to $V_{2(Ge)}$. Results of *multi*−vacancies of Ge have been reported previously, according to the report by Ishii *et al.* [145], the bonds in the Ge *tri*-vacancy are weak and the *tetra*- and *penta*-vacancies have lower formation energies than the same defects in Si. The report also revealed that the formation energy differences between the *tetra* and *penta*-vacancies are 0.32 and 0.22 eV, respectively. Ishii *et al.* [145] also reported *hexa*-vacancies with a formation energy of 8.49 eV. In addition, Ishii [145] argued that the fourfold configurations of germanium *tri*-, *tetra*-, and *penta*-vacancies are not very stable compared to silicon.

Recently, another kind of point defect in Ge was investigated theoretically. These are the vacancy complexes, i.e. a complex with a dopant or other substitutional impurity in Ge. In a recent study by Chroneos *et al.* [107], the interaction between a substitutional impurity and a carbon-dopant vacancy complex were studied and found to bond in some cases and not in others. The report also suggests that dopant-carbon pairs are not stable in Ge compared to their isolated components. However, if they are formed during implantation, they will act as strong vacancy traps. By using GGA, the indium vacancy complex in Ge (In_{Ge}-V_{Ge}) was studied and it was found that the formation of large clusters tend to be energetically favourable–this result explains the reasons why In ions are immobile [146]. Recently, Chroneos *et al.* revealed that it is energetically favourable for the Ge vacancy to form clusters containing up to 4 arsenic atoms that are tetrahedrally coordinated [146], and that the formation of clusters of the phosphorous (P) vacancy complex in heavily doped Ge, is possible [147]. In another development, by using GGA+U, Tahini *et al.* [144] reported that the E-centre

arising from incorporated P and As vacancy complex in Ge can form in the 0, −1 or −2 charge states, whereas with Sb only the 0 or −2 charged states are predicted. The electronic properties and thermal stability of centres which involved a vacancy and an impurity atom (P, As, Sb, or Bi) in Ge crystals have been investigated experimentally by Markevich [130], where it was discovered that an E-centre is induced by irradiation. According to Ref [130], the E-centre in Ge has three charge states: −2, −1 and 0, and introduces two energy levels in the band gap. In addition, the report revealed that shallow donor concentrations at equilibrium conditions for the −2 charged state of the vacancy and impurity atom pairs occur when the Fermi level is at $E_C - (0.18)$ eV to $E_C - (0.22)$ eV. Markevich [130] in another development found that the thermal stability of the E-centres in Ge increased with an increase in the size of donor atoms. The A-centre is an oxygen interstitial atom near a lattice vacancy and is an important impurity-defect pair in germanium. Chroneos *et al.* [148] reported that the nearest neighbour carbon-oxygen (C-O) interstitial is significantly bound, whereas the tin-oxygen (Sn-O) interstitial pairs are not [148]. Other point defects in Ge have been studied and reported. DLTS results for the Mn impurity shows that it induces two acceptor and one donor levels in the band gap of Ge [149]. Table 3.3 gives a summary of some studies of point defects in Ge with their electrical levels.

Several extrinsic and intrinsic point defects in Ge have been studied using either experimental or theoretical techniques. But on the other hand, rare earth (RE) defects in Ge have not been previously reported either experimentally or theoretically. In addition, the Ge *di*-interstitial has not been studied either. Part of this thesis will address these issues and the important results of RE related defects in Ge.

Table 3.3: *Table showing studied defects in Ge and their electrical levels in eV.*

Defect	Techniques	Electrical Levels	Author
	PACs	$\epsilon(+1/0)=E_C-0.04$	Haesslein *et al.* [9]
I_{Ge}	LDA	$\epsilon(+1/0)=E_V-0.11$	Spiewak *et al.* [89]
	"	$\epsilon(+2/+1)=E_V-0.46$	"
	"	$\epsilon(0/-1)=E_V-0.45$	"
	"	$\epsilon(0/-1)=E_V-0.31$	Moreira *et al.* [139]
	PACs	$\epsilon(0/-1)=E_V+0.20$	Haesslein *et al.* [9]
	LDA+U	$\epsilon(0/-1)=E_V+0.02$	Spiewak *et al.* [134, 105]
	"	$\epsilon(-1/-2)=E_V+0.26$	"
V_{Ge}	LDA	$\epsilon(0/-1)=E_V+0.37$	Fazzio *et al.* [141]
	"	$\epsilon(-1/-2)=E_V+0.39$	"
	HSE	$\epsilon(-1/-2)=E_V+0.38$	Weber *et al.* [91]
	"	$\epsilon(0/-1)=E_V+0.16$	"
	"	$\epsilon(+1/0)=E_V+0.15$	"
	DLTS	$\epsilon(0/-1)=E_V+0.33$	Zistl [142]
$V_{2(Ge)}$	DLTS	$E_C-0.35$	Janke *et al.* [136]
	DLTS	$E_C-0.32$	"
$Multi-$vacancies	GGA	-	Ishii *et al.* [145]
$Mn_{(Ge)}$	DLTS	$E_C-0.36$	Lauwaert *et al.* [149]
"	"	$E_V+0.14$	"
E-centre (AsV)	GGA+U	$\epsilon(-1/-2)=E_V+0.47$	Tahini *et al.* [144]
"	"	$\epsilon(0/-1)=E_V+0.26$	"
E-centre (SbV)	GGA	$\epsilon(-1/-2)=E_C-0.29$	Coutinho *et al.* [17]
"	"	$\epsilon(0/-1)=E_V+0.31$	Coutinho *et al.* [17]
	"	$\epsilon(0/-1)=E_V+0.30$	Colder *et al.* [150]
"	GGA	$\epsilon(-1/-2)=E_C-0.37$	Fage-Pedersen *et al.* [128]
	DLTS	$E_C-(0.18-0.22)$	Markevich [130]

Chapter 4

Computational background

4.1 Introduction

In Chapter 2, the formalism and the method of handling many-body problems were discussed. In this chapter, details of the computational techniques used to obtain results presented in this thesis are discussed. In Section 4.2, the computational code and techniques such as VASP, SIESTA, AIMPRO etc. are mentioned with elaborate discussion on VASP. Results reported in this thesis are obtained using the supercell approach. The supercell techniques and the corrections adopted are discussed in Section 4.3 and Section 4.4, respectively. In carrying out supercell calculations, several trade-offs between accuracy and computational time need to be made. These trade-offs include supercell size, number of **k**-points and kinetic energy cut-off (E_{cut}). Section 4.5.1 focuses on the various tests of convergence performed. In each case, the optimum value and an estimate of the error introduced was determined. Finally, in Section 4.6 and Section 4.7, detailed calculations and validation of the computational techniques by comparison with previous theoretical and experimental results are presented.

4.2 Computational code and techniques

There are several density functional theory (DFT) based electronic structure codes for both periodic and molecular structure calculations. These codes are Vienna *Ab initio* Simulation Package (VASP) [54, 151, 152], Cambridge Serial Total Energy Package (CASTEP) [79], QuantumEspresso (formerly called the PWscf) [153], Spanish Initiative for Electronic Simulations with Thousands of Atoms (SIESTA) [154, 155] and *Ab initio* Modelling PROgram (AIMPRO) [156]. Each of these codes has their unique advantages over others. For calculations involving defects in semiconductors, the VASP [48, 54], QuantumEspresso [157], AIMPRO [156, 158, 159] and SIESTA [154, 155] have been used to predict the geometric and electronic structures, thermal and optical properties of several semiconductor materials including Ge. The results presented in this thesis were calculated using VASP.

4.2.1 The Vienna *ab initio* simulation package

VASP is a computer program for atomic scale material modelling by electronic structure calculations and quantum-mechanical molecular dynamics (QMMD) from first principles [54, 160]. VASP computes the solution to the many-body problem Schrödinger equation within the framework of DFT. The HSE hybrid functional is also implemented in the VASP code. Other methods such as the Green's function, many-body perturbation theory, are also available in VASP. In VASP, the electronic density, orbital and local potential are expressed in a plane wave basis set [161]. Interactions between the electrons and ions are portrayed using one of the following approximations: the norm-conserving pseudopotential (NCP) [162], the ultra-soft pseudopotential (UPP) [163] or the projector augmented wave (PAW) technique [152, 164]. In order to deduce the electronic ground state, VASP makes use of iterative matrix diagonalisation techniques, such as the residual minimisation method with direct inversion of the iterative subspace

(RMM-DIIS) or the blocked Davidson algorithms [54, 160]. VASP is used to calculate the electronic structure of materials using different approaches, such as cluster and supercells. Except for the supercell method, other approaches will not be fully discussed. For the results of this thesis, the PAW was used for various calculations. Further comprehensive information on VASP can be found in literature [151, 152, 54].

4.3 Supercell and cluster method of defect modelling

The two most common methods to study defects theoretically are the cluster and the supercell approach. The cluster approach attempts to model a defect that is surrounded by a finite number of atoms (essentially representing a molecular entity), usually with dangling bonds terminated by hydrogen atoms. This approach usually involves the use of convergence tests. Convergence tests are carried out in order to be sure that the size of the cluster is proper and applicable to the real physical system that is being investigated [165]. The major deficiency of the cluster approach is that it is prone to considerable quantum confinement effects that are strongly dependent on the size of the cluster [102].

The supercell approach, on the other hand, is ideally suited to model periodic systems, e.g crystals [102]. In this approach, periodic boundary conditions are imposed on the Kohn-Sham orbitals [80, 102] so that Bloch's theorem discussed in Section 2.6.1 can be satisfied. This means that the supercell is modelled as surrounded by an infinite number of identical copies of itself in a crystal lattice. One challenging problem of the supercell approach is unwanted defect-defect interactions when using a small supercell or when defects are charged [166]. This disadvantage, however can be overcome with the use of a computationally expensive large supercell and the introduction of correction terms [167, 168] which will be discussed in Section 4.4. In this thesis, the supercell approach is adopted and used since it provides good description of the

electronic structure of the host and defect systems.

4.3.1 The supercell approach and methodology

As mentioned above, in this approach periodic boundary conditions are used to model the crystal structure [80, 102] as a periodically repeated unit cell containing a unique basal plane [80]. An important merit of the supercell method is that the prediction of the electronic band structure of the host crystal is correctly described [168]. To yield a more accurate result in the modelling of a defect, the size of the supercell should be large in order to minimize defect-defect interactions in periodic-image supercells [102, 104, 167].

The usual approach adopted within supercell formalisms is to choose a plane-wave basis for the Kohn-Sham wavefunctions [80, 102]. This choice is natural because of the inherent periodicity of the system. The optimised structure of the neutral Ge crystal supercell structure is shown in Figure 4.1 (based on space group P1).

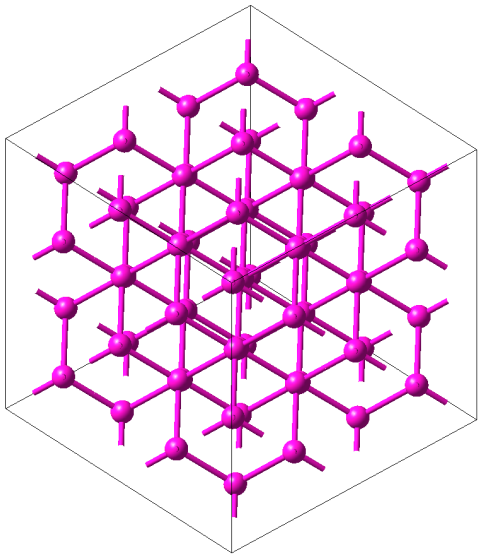

Figure 4.1: *The relaxed geometric structure of a pristine 64-atom supercell of Ge.*

4.4 Supercell correction techniques

The modelling of a defect and the determination of its formation energies in different charged states are subject to finite size errors [167, 169]. In addition, for a charged system, the spurious electrostatic interactions between the charged defect and its periodic images [104, 169] have to be handled in order to avoid errors in the calculated total energy. These errors are usually significant for any reasonably sized supercell and are inherent to the method [101, 104, 170]. A schematic diagram of a cell showing the periodic boundary conditions and the interactions between the defects and their neighbouring images is shown in Figure 4.2.

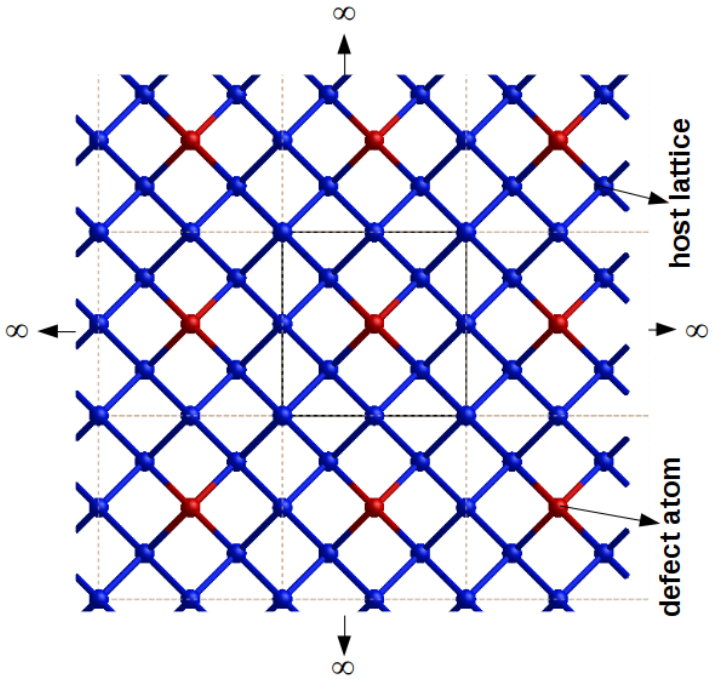

Figure 4.2: *A diagram of a supercell lattice showing the periodic boundary condition and the interactions between the defects and their neighbouring images. The cell with solid outlines in the middle represents the supercell, while the rest are periodic copies.*

4.4.1 Image charge effect

The effect of using a supercell and its image repetitions in 3D gives rise to spurious interactions. This problem of spurious interaction is more complicated when charge states are introduced into a defect system. The introduced charge state in a defect, causes electrostatic interaction between a periodic cell containing the defect. In order to solve this problem, different schemes such as the Makov and Payne correction [171], the Freysoldt, Neugebauer, and Van de Walle [102, 104, 167] correction scheme and the extended Freysoldt scheme [169] have been suggested.

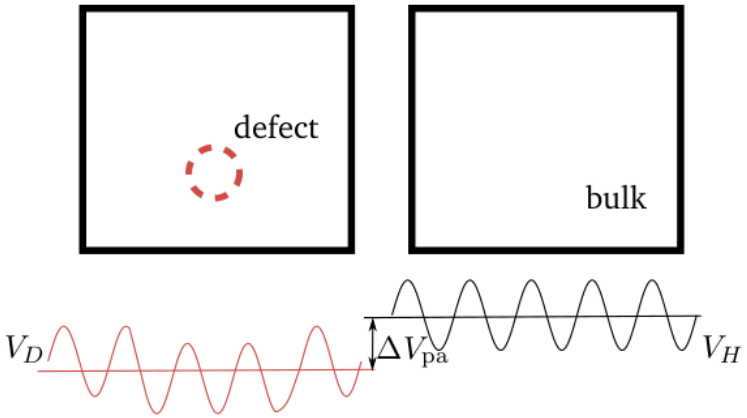

Figure 4.3: *Schematic plot displaying how the defects pull-out of shape the potential relative to the bulk. This distortion is restored by potential alignment relative to that of a pristine crystal. Adapted from Ref [66].*

4.4.2 Potential alignment

Since the introduction of a defect distorts the electrostatic potential relative to the perfect host [168] as shown in Figure 4.3, it is expected that the VBM which serves as a reference energy for the electron reservoir will be shifted. Due to this shifting of the VBM, there is a need for potential alignment between the electrostatic potential of the defect and the perfect supercell [172]. The potential alignment correction can be obtained from the difference in the average electrostatic potential of the host $\overline{V}_H$ at

a point in the supercell where an atom is located; say (a) far from the defect and the defect supercell $\overline{V}_D$ [166, 168, 169]. Mathematically, it may be expressed as

$$\triangle V_{P_a} = \overline{V_D - V_H}. \tag{4.1}$$

The potential alignment $\triangle V_{P_a}$ restores the defect potential relative to that of the pristine crystal.

4.4.3 Corrections schemes

There are different techniques for correcting the errors and the electrostatic potential shift appearing in a relatively small supercell. Such techniques includes the Makov and Payne correction scheme (MPS) [171], the Lany and Zunger scheme (LZS) [101], the Freysoldt, Neugebauer, and Van de Walle scheme which is popularly called the FNV correction scheme [166, 167] and the new extended FNV correction scheme [169].

4.4.3.1 Makov and Payne correction scheme

The Makov and Payne correction scheme is one of the first correction schemes that attempts to correct the error due to charged defect-defect interactions [171]. Makov and Payne correction scheme is based on an extension of the approach by Leslie *et al.* [173], who considered the electrostatic potential due to periodically repeating localised charge q immersed in a dielectric with a dielectric constant (ϵ), calculated using the appropriate Madelung constant (η_M). The Makov and Payne correction scheme extended the approach of Leslie *et al* [173], by including a new term which accounts for the interaction of the delocalized part of the defect induced charge ρ_c with the screened point charge potentials of the images [171]. The Makov and Payne correction scheme can be describe mathematically as

$$E(L) = E(L_\infty) - \frac{\eta_M q^2}{2\epsilon L} - \frac{2\pi qQ}{3\epsilon L^3} + O(L^{-5}), \tag{4.2}$$

where $E(L)$ and $E(L_\infty)$, are the energy calculated from the finite supercell and the energy of the supercell as L goes to infinity, respectively. L is the linear dimension of the supercell and Q is the quadrupole moment of the defect charge. Q is defined as $\int r^2 \rho_c(\mathbf{r}) d\mathbf{r}$ and is asymptotically independent of L. $E(L)$ differs from $E(L_\infty)$, because of the spurious interactions of the aperiodic charge density with its images in neighbouring cells.

4.4.3.2 Freysoldt correction scheme

Another method of practical approach to finite-size correction was introduced by Freysoldt *et al.* [166, 167] and is called the FNV correction scheme. The correction energy of the FNV is expressed as

$$E_{FNV} = E_{PC} - q\triangle V_{PC.\frac{q}{b}}|_{far}, \tag{4.3}$$

where E_{PC} is the point charge (q) correction energy. $\triangle V_{PC.\frac{q}{b}}$ (discussed in Section 4.4.2) is the potential alignment term, which is the potential difference between the defect-induced and the point charge potentials. $\triangle V_{PC.\frac{q}{b}}|_{far}$ is $\triangle V_{PC.\frac{q}{b}}$ far from the defect in the supercell. This potential alignment corresponds to the third order term in Equation (4.2) of the Makov and Payne correction scheme. The relation between $\triangle V_{PC.\frac{q}{b}}$ of the FNV and $\frac{2\pi qQ}{3\epsilon L^3}$ of Makov and Payne correction scheme was discussed by Komsa *et al.* [170]. According to Hine *et al.* [174], the FNV scheme is practical and it involves knowing the electrostatic potentials for the pristine supercell and defect supercell. The two potentials for the pristine supercell and defect supercell are easily obtained from an *ab initio* calculation without the need of carrying out several supercell calculations and no reliance on external parameters is needed.

4.4.3.3 Extended Freysoldt correction scheme

Recently, Kumagai *et al.* [169] described a new method of correction which was an extension of the FNV correction scheme [166, 167]. In the extended FNV correction scheme, Kumagai *et al.* [169] used the principal axis transformation and the Edward scheme to derive the screened potential which is at an arbitrary position $\mathbf{r} \neq 0$ in an anisotropic dielectric. According to the extended FNV scheme, the electrostatic energy of a defect with its images and background charge for a periodic system is given as

$$E_{periodic} = \frac{1}{2}\int_{\Omega}[V_{defect,q}(\mathbf{r}) - V_{bulk}(\mathbf{r})](\rho_d(\mathbf{r}) - \frac{q}{\Omega})d\mathbf{r} \tag{4.4}$$

where the potential of the bulk and defect in its charge state are V_{bulk} and $V_{defect,q}$, respectively, $\rho_d(\mathbf{r})$ is the charge density of a single defect within the supercell and $-\frac{q}{\Omega}$ is the neutralised background charge q distributed over Ω the volume of the supercell. The electrostatic energy of an isolated defect without the periodic boundary condition can be written as

$$E_{isolated} = \frac{1}{2}\int[V_{isolated,q}(\mathbf{r}) - V_{bulk}(\mathbf{r})]\rho_d(\mathbf{r})d\mathbf{r} \tag{4.5}$$

The reason for the extended FNV correction is that the planar average electrostatic potential, used by the FNV correction scheme, is not suitable when atoms far from the defect are strongly shifted from their unrelaxed position after geometric optimization [169].

4.5 Test of convergence

In order to accurately compute the properties of semiconductor materials, tests of convergence for the supercell size, number of **k**-points and plane wave kinetic energy cut-off are required.

4.5.1 Test of supercell size

Before a supercell is used for defect calculations, it must be constructed. To construct a supercell, a fully optimised unit cell is used as a starting point. In order to find the appropriate supercell size, the formation energy of the defect is calculated as a function of the supercell size. Figure 4.4 depicts the formation energy relative to that of a 216 atom supercell as a function of supercell size, for a 400 eV kinetic energy cut-off and using the gamma point to sample the **k**-space. In practice, a supercell size that is large enough is chosen to reduce or eliminate the effect of the defect-defect interactions, but still computationally viable. In this thesis, a 64 atom supercell was adopted since the energy difference between the 64 and 216 atom supercell was less than 0.01 eV.

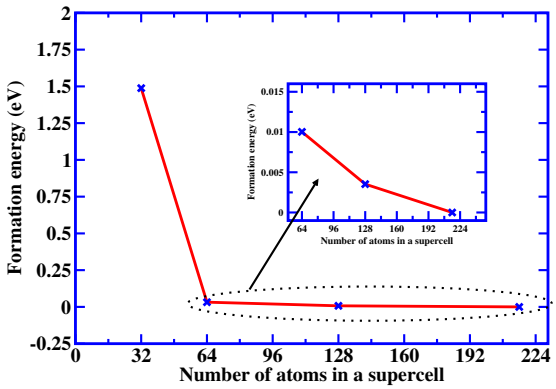

Figure 4.4: *A plot showing the convergence of formation energies difference (eV) and number of atoms of supercell, for the neutral charge state of Ge self interstitial.*

4.5.2 Test of energy cut-off

To ascertain the most suitable energy cut-off (E_{cut}), the total energy of a 64 atom of Ge supercell (relative to that calculated with E_{cut} of 600 eV) with respect to energy cut-off was calculated using Monkhorst-Pack **k**-points of $2 \times 2 \times 2$ (see Figure 4.5). The difference in total energy converges adequately to within a 0.01 eV at 400 eV E_{cut}.

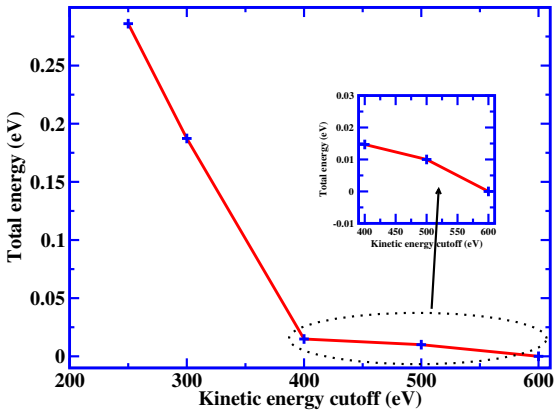

Figure 4.5: *Plot showing the total energy as a function of the E_{cut} as a test of convergence for a 64 atom of Ge supercell. The total energy difference was derived from the difference between the lowest energy and others. The energy cut-off was calculated using Monkhorst-Pack* ***k****-points of* $2 \times 2 \times 2$.

4.5.3 Test of k-points spacing

In order to obtain the most suitable number of **k**-points to sample the Brillouin zone, test of **k**-points are conducted. The variation of the formation energy as a function of Monkhorst-Pack **k**-points (relative to that calculated with $4 \times 4 \times 4$ **k**-point mesh) are determined using an E_{cut} of 400 eV, as shown in Figure 4.6. According to Figure 4.6, using a $2 \times 2 \times 2$ Monkhorst-Pack k-point mesh is sufficient enough to carry out defect calculations because the formation energy difference between a $2 \times 2 \times 2$ and $4 \times 4 \times 4$ **k**-point mesh is less than 0.02 eV. This choice corresponds well to that used in a number of published studies [90, 107, 147, 148].

The overall error due to the combined effects is of the order of 0.05 eV. In calculations involving differences in formation energies (e.g. when determining transition levels), it is expected that the errors partially cancel out, leading to more accurate results than would otherwise be expected.

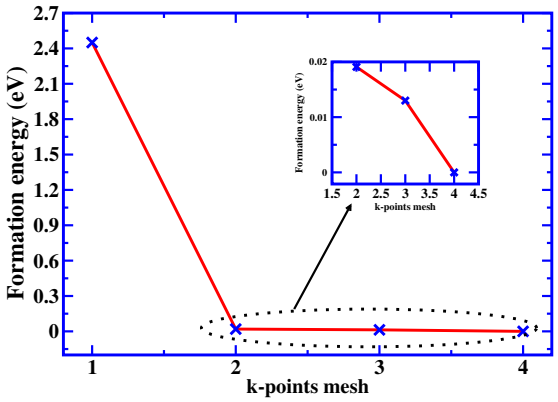

Figure 4.6: *Convergence of defect formation energy of the self interstitial of Ge as a function of* ***k****-points sampling for a 64 atom supercell. (Kinetic energy cut-off of 400 eV was used for the calculation and the values on the x-axis represent an* $n \times n \times n$ *mesh).*

4.6 Details of the calculation

As mentioned earlier, DFT electronic structure calculations as implemented by the Vienna *ab initio* Simulation Package (VASP) [151, 152] was used for the modelling of electronic and optical properties of defects in Ge. The projector-augmented wave (PAW) method, as implemented in the VASP code was used to separate the inert core electrons from the chemically active valence electrons [80, 151]. For Ge, the $4s^2$ and $4p^2$ electrons in the outer shell were treated as valence electrons. This work used the potentials as supplied with the VASP software programme. Calculations were carried out using the Heyd, Scuseria, and Ernzerhof (HSE06) [15, 175] hybrid functional. The pristine 64 atom supercell was constructed from an 8 atom unit cell optimised using a $2 \times 2 \times 2$ Monkhorst-Pack [73] **k**-point Brillouin zone sampling and 400 eV plane wave cut-off of the wave function expansion. In all calculations, the structural optimization continued until both the difference in total energy and forces were less than 10^{-5} eV and 0.001 eV/Å, respectively. The electronic structure was optimised until the energy difference was less than 10^{-5} eV. The energy of formation of a system is strongly dependent on the spin-orbit coupling (SOC) due to the presence of relativistic effects

in heavy atomic systems. To deal with the scalar relativistic effect, the mass-velocity and Darwin correction terms have been incorporated into the PAW potential. In addition to the scalar relativistic effect that was taken into account, spin-orbit coupling was also taken into account for all calculations. To calculate the defect formation and charge state transition energies, Equation (3.6) and Equation (3.9), were used respectively. The uncertainties surrounding the calculation of $E^f(d,q)$ due to finite-size effects and electrostatic defect-defect interactions were handled by including the electrostatic alignment and the image charge correction according to Freysoldt *et al* [104, 166]. The method proposed by Lany *et al.* [101] which was discussed in Section 3.5.6 was used to calculate the ionization energy (I_A) and the electron affinity (E_A). The binding energies E_b which are defined as the energy required to split up the defects cluster into well separated non-interacting defects were calculated using Equation (3.10).

4.6.1 Summary of calculation parameters

For easy comprehension, the details of the calculation adopted in this thesis are summarized in Table 4.1.

Table 4.1: *Table showing summary of calculation details.*

Parameters	Value
number of atoms in supercell	64
kinetic energy cut off (E_{cut})	400 eV
k-points	$2 \times 2 \times 2$
final change in the total energy	$< 10^{-5}$ eV
force	<0.001 eV/Å
correction techniques	FNV and extended FNV

4.7 Validation of computational techniques

The validity of the techniques used in this thesis was investigated by modelling the antimony doped vacancy complex in Ge (Sb_{Ge}-V_{Ge}) known as E-centre in three different

configurations. The formation energy and charge state transition levels of Sb_{Ge}-V_{Ge} were predicted and compared to existing theoretical and experimental results. Table 4.2

Table 4.2: *Calculated formation energies (E^f) in eV at $\epsilon_f = 0$ of Sb_{Ge}-V_{Ge}.*

Defect	Configuration	-2	-1	0	$+1$	$+2$
	fn	0.51	0.11	-0.17	-0.45	2.76
	sn	1.02	0.60	0.31	0.13	3.34
	tn	1.20	0.76	0.45	0.25	3.46

shows the results of the formation energy in eV of the Sb_{Ge}-V_{Ge} at $\epsilon_f = 0$ for the first nearest neighbour (*fn*), second nearest neighbour (*sn*) and third nearest neighbour (*tn*) configurations. Table 4.3 shows the charge state transition levels $\epsilon(q/q')$ in eV for this calculation as well as results from literature.

Table 4.3: *Calculated electrical levels of Sb_{Ge}-V_{Ge} (E-centre) in Ge. These levels are reported with respect to the VBM (E_V) and CBM (E_C). All results are in eV.*

Transition levels	This thesis	DLTS	Cluster
$(-1/-2)$	$E_C - 0.39$	$E_C - 0.37^a$	$E_C - 0.29^b$
		$E_C - 0.41^c$	
$(0/-1)$	$E_V + 0.31^*$	$E_V + 0.31^d$	$E_V + 0.31^b$
		$E_V + 0.30^{a,e}$	

* As determined for the *fn* configuration, which is the most stable configuration
[a]Ref [128], [b]Ref [17], [c]Ref [130] [d]Ref [176] and [e]Ref [150].

Based on the agreement between computational modelling and experimental results, the validation of the computational techniques used for the results of this thesis is established.

Chapter 5

Results

5.1 Introduction

In this chapter, major theoretical results obtained using the HSE06 functional are highlighted. The results in this chapter are solely the author's findings. Some of the results that are presented have been published as articles or they are under review in peer-reviewed journals.

In Section 5.2, results of an *ab initio* study of the germanium *di*-interstitial are reported. Section 5.3 presents the results of a hybrid functional study of Tm^{3+} defects in Ge. In Section 5.4, results of rare earth interstitials in Ge are reported and Section 5.5 presents the result of the Tm^{3+}_{Ge}-V_{Ge} defect complex in Ge.

A summary of all the results is presented in Section 5.6. The references appearing in various articles are not listed in the main reference list unless cited elsewhere.

5.2 *Ab initio* study of the germanium *di*-interstitial using a hybrid functional (HSE)

A published article entitled "*Ab initio* study of germanium *di*-interstitial using a hybrid functional (HSE)" is attached to this chapter in Section 5.7.1 as Article 1.

In this article, results of *ab initio* modelling of the Ge *di*-interstitial ($I_{2(Ge)}$) are reported. The energy of formation, charge state transition levels and the minimum energy configurations of the $I_{2(Ge)}$ were obtained for charge states -2, -1, 0, $+1$ and $+2$. The calculated formation energies show that for all charge states of $I_{2(Ge)}$, the double tetrahedral (T) configuration formed the most stable defect, with 1.24 eV binding energy in the neutral state. The other configurations considered, the double split[110] (SP10) and the combined split[110]/tetrahedral (SPT) formed with binding energies of 0.26 and 0.05 eV, respectively, for the neutral charge state. The difference in the binding energies for the T, SP10 and SPT configurations were as a result of the amount of strain in the bonds of the interstitial atoms and their nearest Ge atoms neighbours. As reported in the paper, the bond angle of one of the interstitials and its two nearest neighbour atoms for the T configuration is about 3° less than that of the SP10 configuration and 1.4° higher than the ideal 109.2° Ge bond angle, this should be the key to understanding the difference in the formation energies of both configurations.

It was found that the (+2/+1), the only charge state thermodynamic transition level for the T configuration is lying below the CBM at $E_C - 0.04$ eV and (+2/+1) for the split[110]-tetrahedral configuration is located at $E_V + 0.41$ eV. According to the result, the *di*-interstitial in Ge is found to, depending on the defect configuration, cause either shallow or deep donor levels at charge state (+2/+1) within the band gap. The $I_{2(Ge)}$ in the SPT and SP10 configurations, gave rise to levels with negative-U ordering, with *effective-U* values of -0.61 (for the SPT configuration) or -1.6 eV (for the SP10 configuration). The result of this article were compared with calculations of

di-interstitials in silicon and other experimental data.

5.3 A hybrid functional calculation of Tm^{3+} defects in germanium (Ge)

A published article entitled "A hybrid functional calculation of Tm^{3+} defects in germanium (Ge)" is attached to this chapter in Section 5.7.2 as Article 2.

The result of DFT modelling of the Tm^{3+} interstitial (Tm_i^{3+}), vacancy-interstitial complex (V_{Ge}-Tm_i^{3+}) and substitutional (Tm_{Ge}^{3+}) defects in Ge are reported. The Tm^{3+} interstitial was found to exist in the tetrahedral and hexagonal configurations with formation energy between 0.24 and 4.35 eV for all charge states. According to the results, for all charge states of the Tm_i^{3+}, the T configuration was energetically more favourable than the H configuration. This is as a result of different amount of strain experienced by the atoms when the interstitial atom was introduced into the pristine supercell. The formation energies for V_{Ge}-Tm_i^{3+} and Tm_{Ge}^{3+} were as low as 0.84 eV. According to the results of the article, the energetically most favourable configurations of these defects were the V_{Ge}-Tm_i^{3+} in the *axial* configuration and the Tm_{Ge}^{3+}. The Tm_{Ge}^{3+} and V_{Ge}-Tm_i^{3+} introduced both a double acceptor and a double donor levels. The charge state thermodynamic transition levels of both the Tm_{Ge}^{3+} and V_{Ge}-Tm_i^{3+} were positioned deep, near the middle of the band gap. The majority of the transition levels induced by the defects under investigation are either shallow donors or acceptors level lying close to the VBM or CBM.

5.4 Rare earth interstitials in Ge: a hybrid density functional theory study

A published article entitled "Rare earth interstitials in Ge: a hybrid density functional theory study" is attached to this chapter in Section 5.7.3 as Article 3.

In this work, results for rare earth (Ce, Pr, Eu and Er) interstitials in Ge were reported. The formation energies and the charge state transition levels for the tetrahedral (T) and hexagonal (H) configurations of Ce, Pr, Eu and Er interstitials in Ge were calculated. We did not consider the split interstitial configuration at this stage. While the charged states of the T configurations for the Ce and Pr interstitials in Ge were not thermodynamically accessible, for both the T and H configuration, the Eu and Er interstitials in Ge created deep levels in the band gap. The H configuration of the Ce interstitial in Ge induced a shallow donor level. The Eu and Er interstitial exhibit properties of negative-U ordering and the characteristics of charge state controlled metastability, respectively.

5.5 A first principle hybrid functional calculation of Tm_{Ge}^{3+} -V_{Ge} defect complexes in germanium

A published article entitled "A first principle hybrid functional calculation of Tm_{Ge}^{3+} -V_{Ge} defect complexes in germanium" is attached to this chapter in Section 5.7.4 as Article 4.

By means of the density functional theory (DFT), using the Heyd, Scuseria, and Ernzerhof (HSE06) hybrid functional, results of the Tm_{Ge}^{3+}-V_{Ge} defect complexes in Ge were reported. The formation energies of the first (*fnn*), second (*snn*), third (*tnn*) and fourth ($f_t nn$) nearest neighbour configurations of Tm_{Ge}^{3+}-V_{Ge} were examined. The charge state transition levels for all these configurations were examined as well. The

Tm_{Ge}^{3+}-V_{Ge} complexes were found to have positive binding energies for the neutral charge state in the *fnn* and $f_t nn$ configurations.

The thermodynamic transition levels revealed that the Tm_{Ge}^{3+}-V_{Ge} creates shallow levels in the band gap for the *fnn*, *tnn* and $f_t nn$ configurations and a deep level at E_V + 0.41 eV for the *tnn* configuration. The *snn* configuration showed no charge state transition levels in the band gap. The Tm_{Ge}^{3+}-V_{Ge} in the *tnn* configuration, displayed evidence of a single donor level $(+1/0)$ and an acceptor level $(0/-1)$ within the band gap. The Tm_{Ge}^{3+}-V_{Ge} defect exhibits charge state controlled metastability.

5.6 Results summary

All results obtained have already appeared in the various articles that are included in Section 5.7. However, it will be very useful to repeat a few important results. Summary of the various important results reported in this thesis are as follows:

1. **Structural and electronic properties of Ge:** Results of structural and electronic properties of Ge have been previously studied either using the LDA, GGA or HSE [3, 98, 138]. Good agreement between experimental and theoretical results for both structural and electronic properties of Ge has been reported in Article 1 and 2.

2. **Point defect induced deep and shallow levels:** A number of defects studied and reported in this thesis induced deep or shallow levels. Point defect induced deep or shallow levels were reported in all the attached articles. Table 5.2 and Table 5.1 show the deep and shallow levels induced in Ge, respectively.

3. **Metastability of point defects in Ge:** The rare earth defects in Ge induced charged state controlled metastability, an interesting property which might have novel applications. The presence of charge state controlled metastability in Ge is

Table 5.1: *Table showing the deep level defects in Ge and their energies in eV.*

Defect	Configuration	Transition levels	Energies (eV)	Nature	Article
$I_{2(Ge)}$	SP10	$(+1/+2)$	$E_V + 0.41$	donor	1
$I_{2(Ge)}$	SP10	$(+1/-1)$	$E_C - 0.20$	negative-U	"
$I_{2(Ge)}$	SPT	$(+1/-1)$	$E_C - 0.31$	"	"
V_{Ge}-Tm_i^{3+}	*axial*	$(0/-1)$	$E_C - 0.30$	acceptor	2
V_{Ge}-Tm_i^{3+}	*axial*	$(+2/+1)$	$E_V + 0.19$	donor	"
V_{Ge}-Tm_i^{3+}	*axial*	$(+1/0)$	$E_V + 0.34$	donor	"
V_{Ge}-Tm_i^{3+}	*basal*	$(0/-1)$	$E_C - 0.23$	acceptor	2
V_{Ge}-Tm_i^{3+}	*basal*	$(+1/0)$	$E_V + 0.44$	donor	"
V_{Ge}-Tm_i^{3+}	*basal*	$(+2/+1)$	$E_V + 0.27$	donor	"
Er_i	T	$(+2/+1)$	$E_C - 0.28$	donor	3
Er_i	H	$(-1/-2)$	$E_C - 0.18$	acceptor	"
Eu_i	H	$(+1/0)$	$E_C - 0.26$	donor	3
Eu_i	H	$(+2/+1)$	$E_V + 0.26$	donor	"
Eu_i	T	$(+2/-2)$	$E_V + 0.18$	negative-U	"
Tm_{Ge}^{3+}-V_{Ge}	*tnn*	$(0/-2)$	$E_V + 0.41$	negative-U	4
Tm_{Ge}^{3+}-V_{Ge}	$f_t nn$	$(-1/-2)$	$E_V + 0.21$	acceptor	"
Tm_i^{3+}	H	$(+2/+1)$	$E_V + 0.22$	donor	2
Tm_i^{3+}	H	$(+1/0)$	$E_C - 0.23$	donor	"
Tm_{Ge}^{3+}	-	$(0/-1)$	$E_C - 0.26$	acceptor	2
Tm_{Ge}^{3+}	-	$(+1/0)$	$E_V + 0.19$	donor	"

reported in Article 3 which describes Eu interstitial in Ge. In addition, the Tm_{Ge}^{3+}-V_{Ge} complexes in Ge reported in Article 4 displays the properties of charge state controlled metastability.

4. **Negative-U properties of point defects in Ge:** Negative-U properties were seen in a number of point defects studied and reported in this thesis. Negative-U behaviour was predicted for the Ge *di*-interstitial, which is reported in Article 1 and for the Eu interstitials in Ge which are reported in Article 3.

5. **Stability of defect complex in Ge:** The stability of defect complexes in Ge are reported in Articles 1, 2 and 4. The Ge *di*-interstitial reported in Article 1 had

Table 5.2: *Table showing the shallow level defects in Ge and their energies in eV.*

Defect	Configuration	Transition levels	Energies (eV)	Nature	Article
$I_{2(Ge)}$	T	$(+2/+1)$	$E_C - 0.04$	donor	1
Tm_i^{3+}	T	$(+2/+1)$	$E_C - 0.04$	donor	2
Tm_i^{3+}	H	$(0/-1)$	$E_C - 0.13$	acceptor	"
Tm_{Ge}^{3+}	-	$(+2/+1)$	$E_V + 0.10$	donor	2
Tm_{Ge}^{3+}	-	$(-1/-2)$	$E_C - 0.05$	acceptor	"
V_{Ge}-Tm_i^{3+}	*axial*	$(-1/-2)$	$E_C - 0.10$	acceptor	"
V_{Ge}-Tm_i^{3+}	*basal*	$(-1/-2)$	$E_C - 0.14$	acceptor	"
Tm_{Ge}^{3+}-V_{Ge}	fnn	$(-1/-2)$	$E_V + 0.06$	acceptor	4
Tm_{Ge}^{3+}-V_{Ge}	tnn	$(+1/0)$	$E_V + 0.05$	donor	"
Ce_i	H	$(+2/+1)$	$E_C - 0.03$	donor	3
Eu_i	H	$(0/-1)$	$E_C - 0.14$	acceptor	3

positive binding energies, which suggest the stability of the defect. In addition, the vacancy-interstitial complex (V_{Ge}-Tm_i^{3+}) and the Tm_{Ge}^{3+}-V_{Ge} complex reported in Articles 2 and 4, respectively have positive binding energies. Table 5.3 shows a collection of binding energies of defect complexes reported in this thesis.

Table 5.3: *Table showing the binding energies of vacancy and interstitial complexes in Ge reported in this thesis.*

Defect	Configuration	Binding energy (eV)	Article
$I_{2(Ge)}$	SP10	0.26	1
$I_{2(Ge)}$	T	1.24	1
$I_{2(Ge)}$	SPT	0.04	1
V_{Ge}-Tm_i^{3+}	*axial*	4.24	2
Tm_{Ge}^{3+}-V_{Ge}	fnn	0.06	4
Tm_{Ge}^{3+}-V_{Ge}	f_tnn	0.05	4

5.7 Published articles

This section presents in Section 5.7.1, an attached article entitled "*Ab initio* study of germanium *di*-interstitial using a hybrid functional (HSE)". Section 5.7.2 and Section 5.7.3 present attached articles entitled "A hybrid functional calculation of Tm^{3+} defects in germanium (Ge)" and "Rare earth interstitials in Ge: a hybrid density functional theory study", respectively. Section 5.7.4 presents an attached article entitled "A first principle hybrid functional calculation of Tm_{Ge}^{3+} -V_{Ge} defect complexes in germanium".

5.7.1 Article 1

Ab initio study of germanium *di*-interstitial using a hybrid functional (HSE)

E. Igumbor, C.N.M. Ouma, G. Webb and W.E. Meyer

Physica B: Condensed Matter 480 (2016): 191-195.

http://dx.doi.org/10.1016/j.physb.2015.08.015

Physica B 480 (2016) 191–195

Contents lists available at ScienceDirect

Physica B

journal homepage: www.elsevier.com/locate/physb

Ab-initio study of germanium *di*-interstitial using a hybrid functional (HSE)

E. Igumbor [a,b,*], C.N.M. Ouma [a], G. Webb [a], W.E. Meyer [a,**]

[a] Department of Physics, University of Pretoria, Pretoria 0002, South Africa
[b] Department of Mathematics and Physical Sciences, Samuel Adegboyega University, Km 1 Ogwa/Ehor Rd, Ogwa, Edo State, Nigeria

ARTICLE INFO

Article history:
Received 15 May 2015
Received in revised form
5 August 2015
Accepted 7 August 2015
Available online 11 August 2015

Keywords:
Interstitial
Defects
Charge state

ABSTRACT

In this work, we present *ab-initio* calculation results of Ge *di*-interstitials ($I_{2(Ge)}$) in the framework of the density functional theory (DFT) using the Heyd, Scuseria, and Ernzerhof (HSE) hybrid functional. The formation energy, transition levels and minimum energy configurations were obtained for $I_{2(Ge)}$ -2, -1, 0, $+1$ and $+2$ charge states. The calculated formation energies show that for all charge states of $I_{2(Ge)}$, the double tetrahedral (T) configuration formed the most stable defect with a binding energy of 1.24 eV in the neutral state. We found the $(+2/+1)$ charge state transition level for the T lying below the conduction band minimum and $(+2/+1)$ for the split[110]-tetrahedral configuration lying deep at 0.41 eV above the valence band maximum. The *di*-interstitials in Ge exhibited the properties of both shallow and deep donor levels at $(+2/+1)$ within the band gap and depending on the configurations. $I_{2(Ge)}$ gave rise to *negative-U*, with *effective-U* values of -0.61 and -1.6 eV in different configurations. We have compared our results with calculations of *di*-interstitials in silicon and available experimental data.

1. Introduction

The application of germanium (Ge) as a promising material for complementary metal-oxide semiconductors (CMOS) technology is attracting attention due to its narrow band gap, high carrier mobility and low voltage operations [1,2]. For successful technology, industrial application and utilization of Ge based devices, it should be single crystalline and free of detrimental defects. The knowledge of formation and transition charge state energies are of interest in defects, and the understanding of defects and their transition charge state energies within the band gap are important towards controlling and engineering their formation in order to improve the material quality. Based on the charge states properties of defects in Ge, it is possible to understand the characteristics of electron irradiation damage and its dependency on the Fermi level. Progress in the identification of electron irradiation damage defects was interrupted by investigations into radiation defects in silicon (Si), but has now become topical again owing to the higher carrier mobilities realized in Ge based devices [3]. Defect studies in Ge are not too common, particularly those dealing with the atomic and electronic details of elemental radiation induced defects. This deficiency does not only apply to experimentation [4] but to modeling as well [5]. Recently, deep level transient spectroscopy (DLTS) [6,7] and infrared absorption spectroscopy [4] studies have succeeded in identifying new radiation defects paired with impurities. Perturbed angular correlation spectroscopy (PACS) studies [8] have led to important findings on the mobility and electrical activity of vacancies (V) and interstitials (I); these two defects created following low temperature radiation, which have been investigated by *in situ* DLTS [7,8].

Various theoretical investigations have attempted to explain experimental data [9,7,10], where some progress has been achieved in understanding the properties of vacancy, *self*- and interstitial related defects in Ge. In a detailed study of interstitial and vacancies in Ge using local density approximation (LDA) and generalized gradient approximation (GGA) [11], the energetic, stability and equilibrium of different configurations were investigated, and interstitials in Ge were found to be bistable having a double donor when at cage site, without any trace of acceptor [12]. The split[110] interstitial has been reported to be more energetically stable than the tetrahedral and hexagonal configurations [9]. The split[110] interstitial configurations were reported to have an acceptor level located at E_V +0.45 eV, while the tetrahedral acts as a donor at E_V +0.11 eV and E_V +0.46 eV for the $(+2/+1)$ and $(0/+1)$ occupancy levels [9,13] respectively. According to Janke et al. [14] vacancy defects in Ge will anneal by diffusion provided the trap density is high enough. *Self*-interstitial reflection by Ge surfaces has been proposed [15] to explain the results of

* Corresponding author at: Department of Physics, University of Pretoria, Pretoria 0002, South Africa.
** Corresponding author.
E-mail addresses: elgumuk@gmail.com (E. Igumbor), wmeyer@up.ac.za (W.E. Meyer).

http://dx.doi.org/10.1016/j.physb.2015.08.015
0921-4526/

diffusion experiments during irradiation. This analysis was extended to diluted SiGe alloys, which provides some explanation of the theoretical donor level calculations for pure Si and alloys with a different Ge content [16]. Cowern et al. [17] reported Ge to be a complex, mutable with a structure similar to an amorphous pocket. Analogous morph structures are expected to exist for both the *self*-interstitial and the vacancy in Si. This paved the way for the study of trivacancy, trivacancy-oxygen complexes and *self*-interstitial clusters in Si and Ge. Defect studies of Si in particular, *self-*, *di-*, *tri-* and *small cluster* interstitials [18,19] and vacancies [20,21] have been reported. However contrary to Si no *di-* and *small cluster* interstitials of intrinsic defects in Ge have been accomplished, thus a detailed formation energy, transition charge states calculation and interpretation of results of *di*-interstitial are still missing. In this work we have carried out hybrid functional of Heyd, Scuseria, and Ernzerhof (HSE) [22,23] calculations of $I_{2(Ge)}$ in the double split [110] (SP10), split[110]-tetrahedral (SPT) and double tetrahedral (T) configurations. We calculated the formation and transition charge state energies within the band gap as was reported in the case of Si [18,12] with a view to finding the most energetically stable configuration, and finally compared our results with experimental and other available data.

2. Computational details

DFT electronic structure calculations were performed in the Vienna *ab-initio* Simulation Package (VASP) [24,25]. We used projector-augmented wave (PAW), as implemented in the VASP code to separate the inert core electrons from the chemically active valence electrons [25–27]. Calculations were carried out using the Heyd, Scuseria, and Ernzerhof (HSE) [22,23] hybrid functional. In this approach, the short-range exchange potential is calculated by mixing a fraction of nonlocal Hartree–Fock exchange with the generalized gradient approximation (GGA) functional of Perdew, Burke, and Ernzerhof (PBE) [11]. The hybrid functional introduces a percentage of exact non-local Fock exchange (25%) to the PBE functional [22,23]. For the bulk, geometric optimization of Ge was performed in the primitive unit cell by means of the 8^3 Monkhorst–Pack [28] *k*-points Brillouin zone sampling scheme and a cutoff energy of 400 eV. Relaxations converged when the forces on all the atoms were less than 0.01 eV/Å. For the pure Ge, we employed 64 atom supercells, and for the defects, two Ge atoms were introduced into the 64 supercell atoms. We then used the 2^3 Monkhorst–Pack [28] special *k*-points Brillouin zone sampling scheme, achieving convergence of the total energy by setting the energy cutoff of the wave function expansion for the charge states to 600 eV. Spin orbit coupling was taken into account in all the calculations. The *concentrations* (C) of defects in thermodynamic equilibrium are related to the formation energy (E^f) through Boltzmann constant

$$C = N_0 \exp(-E^f/k_B T), \tag{1}$$

where $k_B T$ is the temperature in eV and N_0 the number of possible defects sites. In Eq. (1) the increase in formation energies leads to decrease in the concentration of the defects. For the defect charge states, E^f depends on Fermi level (ε_F). E^f of defects are derived directly from total energies, allowing the calculation of equilibrium defect *concentrations* [29]. To calculate the defects E^f and transition energy ($\epsilon(q/q')$) levels, we calculated the total energy $E(d, q)$ for a supercell containing the optimized defect d in its charge state q. The defect formation energy $E^f(d, q)$ as a function of electron Fermi energy (ε_F) is given as [29,30]

$$E^f(d, q) = E(d, q) - E(pure) + \sum_i \Delta(n)_i \mu_{Ge} + q[E_V + \varepsilon_F + \Delta V] + \Delta^q, \tag{2}$$

where $E(pure)$ is a supercell without a defect, $\Delta(n)_i$ is the difference in the number of constituent atoms of type i between the supercells, E_V is the valence band maximum (VBM) and $\mu_{Ge} = -5.18$ eV is the chemical potential of germanium. For us to pay special attention to the uncertainties surrounding the calculation of $E^f(d, q)$ due to finite-size effects within the supercell and inaccuracy underlying the approximation of energy functional, we have included the electrostatic alignment ΔV and the image charge correction (Δ^q) according to Freysoldt et al. [31,32]. The defect transition energy level $\epsilon(q/q')$ is the Fermi energy for which the formation energy of charge state q equals that of charge state q' is given as [30]

$$\epsilon(q/q') = \frac{E^f(d, q; \varepsilon_F = 0) - E^f(d, q'; \varepsilon_F = 0)}{q' - q} \tag{3}$$

The method proposed by Stephan et al. [33] was taken into account for the calculation of the ionization energy (I_A) with reference to the conduction band (CBM) and the electron affinity (E_A) with reference to valence band maximum (VBM). The binding energy E_b which is defined as the energy required to split up an interstitial cluster into well separated non-interacting *mono*-interstitials was calculated using the method proposed by Zollo et al. [34].

3. Results and discussion

In contrast to the LDA and GGA that underestimate the band gap of the semiconductor [13], the HSE functional gives an excellent description of the electronic band gap and charge state transition properties for a wide range of the defects in group-IV semiconductors [35]. The pristine Kohn–Sham band gap of Ge was calculated to be 0.80 eV, which was higher than the experimental band gap at 0 K. To address the band gap problem in order to obtain the experimental band gap of Ge, we employed the quasiparticle band gap [36,33] calculation, which from the calculated I_A and the E_A energies of 4.00 and 3.22 eV respectively, resulted in an improved Ge band gap of 0.78 eV, that is in agreement with the experimental band gap reported by Morin et al. [37] at 0 K. For us to calculate the formation energy of $I_{2(Ge)}$, we first calculated the formation energies of Ge *self*-interstitial. For both the tetrahedral and split[110] configurations in the neutral state for *self*-interstitial, we have calculated 3.88 and 3.80 eV respective formation energies, and our results were in close agreement with earlier results [12,13,38] based on LDA and GGA functionals.

3.1. Structural properties and energetics of $I_{2(Ge)}$

We calculated the relaxed configurations for a number of different geometric configurations and found three competing geometric structures: split[110]-tetrahedral (SPT), split–split[110] (SP10) and tetrahedral–tetrahedral (T). These structural equilibrium configurations were obtained by adding a tetrahedral or split[110] interstitial atom to a cell containing a fully relaxed split [110] or tetrahedral single interstitial atom. The optimized structures as in the case of Si [39,21] demonstrated that each interstitial atom of the pair forms bonds with neighboring atoms resulting in full four-fold coordination as seen in Fig. 1. Fig. 1(a) shows the relaxed structure of the T configuration and Fig. 1(b) represents the optimized structure of the SP10 configuration. This structure is

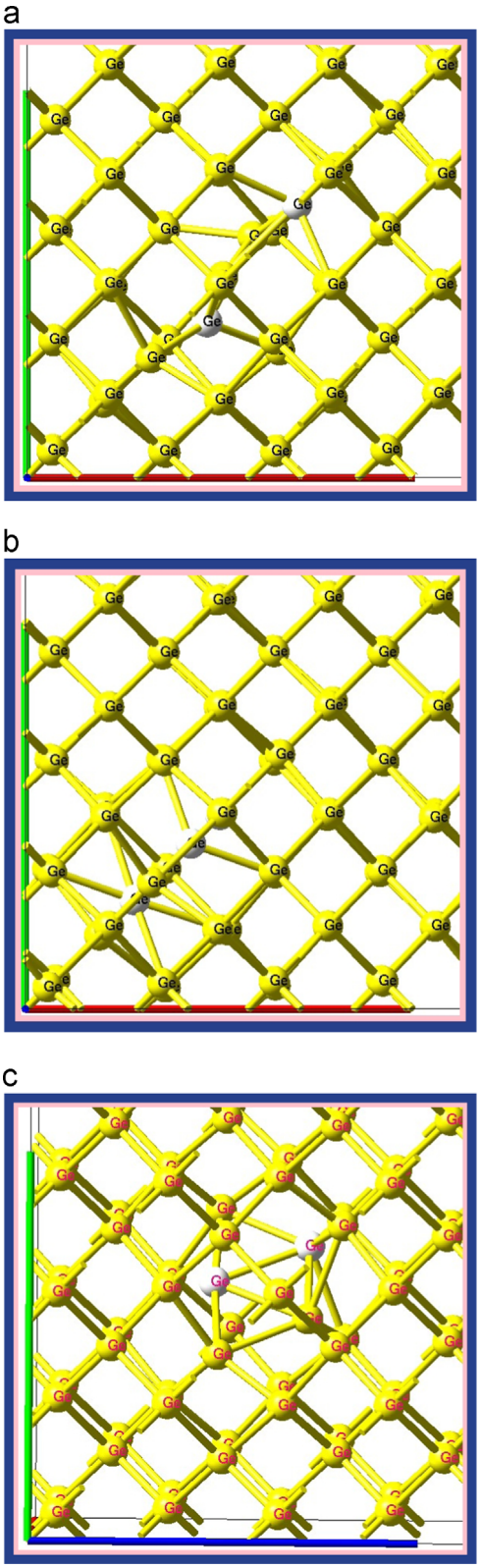

Fig. 1. (a) Optimized structure of T; double tetrahedral interstitial atoms, (b) optimized structure of SP10; double split[110] interstitial atoms and (c) optimized structure of SPT; split[110] and tetrahedral interstitial atoms. All interstitial atoms in white for the various configurations.

obtained by combining two interstitials in the split[110], which many believe to be the most stable interstitial configuration of Ge as well as Si and in the case of Si is responsible for extremely fast migration. Fig. 1(c) represents the optimized structure of the SPT configuration. The defect caused a reduction in bond length as neighboring atoms and defect atoms repositioned to a position of equilibrium, the reduction being approximately between 0.02 and 0.07 Å in all the configurations. The bond angle between one of the defects and its two nearest neighbors after optimization was 110.62° and 113.5° for T and SP10 respectively. For the SPT configurations, the angles were 101° and 110.62° for the two interstitial atoms.

Table 1
Calculated formation E^f and binding energies E_b in eV for the neutral state of the various defect configurations. We have included other references for easy comparison. Our work in bold.

Defects	SP10	T	SPT
Ge_i (E^f)	**3.80** 3.54 [9] 3.56 [13]	**3.88** 3.79 [13] 3.84 [9]	not applicable
$I_{2(Ge)}$ (E^f) $I_{2(Si)}$ (E^f)	**7.34** 6.10 [40]	**6.52** 6.14 [40] 6.46 [44]	**7.63** 5.12 [21] 4.91 [41]
$I_{2(Ge)}$ (E_b) $I_{2(Si)}$ (E_b)	**0.26** 1.74 [40]	**1.24** 1.70 [40]	**0.05** 1.41 [41]

3.2. Electronic structure of the $I_{2(Ge)}$

The most stable structures of the $I_{2(Ge)}$ configuration were represented in Fig. 1; the formation and binding energies for the charge states are shown in Table 1. In all the configurations, the T configuration was the most stable in the neutral state. For the neutral state of $I_{2(Si)}$, the E^f of SP10 was found by Posselt et al. [40] to be lower than that of the T configuration by 0.04 eV. Jones et al. [21] found that the SPT configuration had an even lower formation energy. The results listed in Table 1 show positive binding energies for all configurations investigated. This agrees with results for Si obtained by Posselt et al. [40] and Bongiorno et al. [41], who also found positive binding energies in the SP10, T and SPT of $I_{2(Si)}$. It should be noted that, in contrast to Si, the most stable configuration for $I_{2(Ge)}$ was the T configuration. It is also interesting to know that for Ge, the SP10 configuration has a formation energy of 0.82 eV more than the T configuration while in Si the SP10 formation energy was 0.04 eV less than the T configuration formation energy.

Fig. 2 shows the formation energy of the $I_{2(Ge)}$ as a function of the Fermi-level for the different configurations. As shown in Fig. 2 (a) and (b), our calculation demonstrates that $I_{2(Ge)}$ was stable in the T and SP10 configurations as a double ionized state. The energy levels of $(+2/+1)$ and $(+1/-1)$ transition charge states of Ge and Si were tabulated in Table 2, we have decided to limit the charge state transition levels of $I_{2(Si)}$ to $(+1/-1)$ and $(+2/+1)$ since other levels were not present in our calculation. For the T configuration, the $(+2/+1)$ level lies above the valence band, with a value of 0.74 eV referencing the VBM. The SP10-configuration transition state level for $(+2/+1)$ was 0.41 eV which was lying deep, almost in the middle of the band gap. The $(+2/+1)$ donor level found in both the T and SP10 configurations exhibit both shallow and deep levels. Donor level property was not only found in *di*-interstitial but also in self-interstitial for the T configuration at $E_C - 0.06$ eV. For the SPT configuration, as represented in Fig. 2(c) there was no transition state level found within the band for $(+2/+1)$. Instead we found a deep lying level of $(+1/-1)$, which was not the case for the Si in SP10 configuration where it was earlier found that the $(+2/+1)$ shallow level was 0.03 eV lying close to the valence band [21]. The behavior of $+1$ and $+2$ charge state of $I_{2(Si)}$ is tied to the valence band where as in Ge it is close to the conduction band for

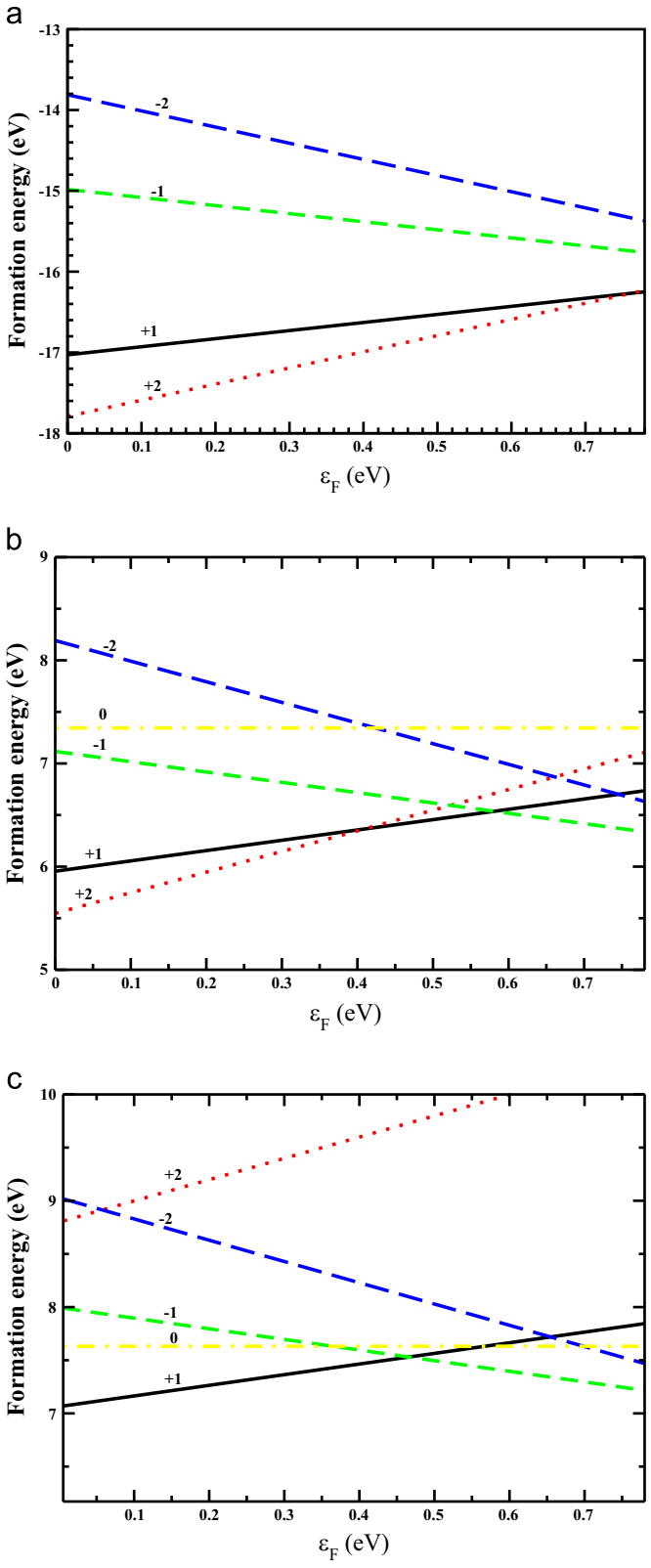

Fig. 2. Plot of formation and Fermi energies of (a) T, (b) SP10 and (c) SPT configurations of $I_{2(Ge)}$ as a function of the Fermi energy (ε_F), indicating the different charge states and transition levels observed with the band gap. The SPT and SP10 configurations show *negative-U* property. We have used the quasiparticle like band gap of 0.78 eV since it was in agreement with experimental band gap result at 0 K.

the T and deep in the band gap for the SP10 configuration. Since $I_{2(Ge)}$ defects transition state levels were positively charged (+1 and +2), they should exhibit a Poole–Frenkel effect (field assisted thermal ionization), which occurs as a result of the lowering of a Coulombic potential barrier when it interacts with the field in the presence of a positively charged trap which gives rise to interaction between the positively charged trap and the electron [42]. Information on the relative stability of different charge states for a specific defect are contained in the formation energy. The charge-state transition levels $\epsilon(q/q')$ delineate the energy regions over which particular charge states are stable. The normal arrangement is $\epsilon(+1/0) < \epsilon(0/-1)$ indicating a positive repulsive energy *U* when electrons are added. However we sometimes witness ordering, of this type $\epsilon(0/-1) < \epsilon(+1/0)$, a term that is referred to *negative-U*. It is interesting to know that while Si shows traces of acceptor on the contrary we discovered that Ge exhibits properties of *negative-U* in the SPT and SP10 configurations. Fig. 2(b) and (c) clearly shows the (+1/−1) transition level at E_V +0.47 and E_V +0.58 eV in SPT and SP10 configurations respectively. The *effective-U* arising from this large difference of lattice relaxation for SPT and SP10 configurations was −0.61 and −1.6 eV respectively. Both the *di*-interstitial and *self*-interstitial of Ge did not show any acceptor-like level in any configuration, and negative charge states were never the most stable in our calculation; which is in contrast to the (0/−1) transition state level found in $I_{2(Si)}$ [19]. No metastability was predicted in any configuration of $I_{2(Ge)}$, whereas Lee et al. [43] predicted metastability for the $I_{2(Si)}$. The electronic energy calculation has shown that the $I_{2(Ge)}$ is more stable than the *mono*-interstitial, and that its existence can be examined by exploring shallow donors near the conduction band edge.

Table 2
Calculated transition states (+2/+1) and (+1/−1) levels (eV) of $I_{2(Ge)}$and $I_{2(Si)}$. This work in bold.

Defects	SP10	T	SPT
$I_{2(Ge)}$ (+2/+1)	**E_V +0.41**	**E_C −0.04**	–
$I_{2(Ge)}$ (+1/−1)	**E_V +0.58**		**E_V +0.47**
$I_{2(Si)}$ (+2/+1)	E_V +0.03 [21]		E_V +0.20 [19]

4. Conclusion

In summary we have carried out detailed calculations of $I_{2(Ge)}$ defects in different configurations, using the Heyd, Scuseria, and Ernzerhof (HSE) hybrid functional in the framework of DFT. The electronic and structural properties of these configurations were described in detail. We have shown that the formation of $I_{2(Ge)}$ from two neutral isolated interstitials was energetically favourable. Our calculation shows that the tetrahedral (T) configuration, where both interstitials were at a tetrahedral site, was more stable than the split[110]-tetrahedral (SPT) and double split[110] (SP10) configurations by more than 0.8 eV, therefore the T configuration should dominate under equilibrium conditions. In this configuration, *di*-interstitials exhibit the property of a shallow donor (+2/+1) at E_C −0.04. In the SP10, deep levels at E_V +0.41 eV for (+2/+1) and E_V +0.47 for (+1/−1) were predicted, while in SPT only a deep level at E_V+0.58 eV for (+1/−1) was predicted. We observed the presence of *negative-U* having *effective-U* values of −0.61 and −1.6 eV for the SPT and SP10 configurations respectively. We pointed out the role of $I_{2(Ge)}$ in an electrically activating donor. We expect the data presented to be useful in the process modeling of Ge-based devices.

Acknowledgment

This work is based on the research supported partly by National Research foundation (NRF) of South Africa (Grant specific unique reference number (UID) 78838). The opinions, findings and conclusion expressed are those of the authors and the NRF accepts no liability whatsoever in this regards.

References

[1] C. Chui, H. Kim, P. McIntyre, K. Saraswat, Technical Digest—International Electron Devices Meeting, 2003, pp. 437–440.
[2] M. Houssa, A. Satta, E. Simoen, B. De, M. Jaeger, M. Caymax, M. Heyns, Germanium-Based Technologies: From Materials to Devices, 2011, p. 233.
[3] L. Lee, E.A. Fitzgerald, T. Bulsara, Mayank, T. Currie, A. Lochtefeld, J. Appl. Phys. 97 (1) (2005) 011101.
[4] J. Fage-Pedersen, A.N. Larsen, A. Mesli, Phys. Rev. B 62 (2000) 10116–10125.
[5] J. Coutinho, R. Jones, P.R. Briddon, S. Öberg, Phys. Rev. B 62 (2000) 10824–10840.
[6] V.P. Markevich, I.D. Hawkins, A.R. Peaker, V.V. Litvinov, L.I. Murin, L. Dobaczewski, J.L. Lindström, Appl. Phys. Lett. 81 (10) (2002) 1821–1823.
[7] F.D. Auret, S.M.M. Coelho, M. Hayes, W.E. Meyer, J.M. Nel, Phys. Status Solidi A 205 (1) (2008) 159–161.
[8] H. Haesslein, R. Sielemann, C. Zistl, Phys. Rev. Lett. 80 (1998) 2626–2629.
[9] M.D. Moreira, R.H. Miwa, P. Venezuela, Phys. Rev. B 70 (2004) 115215.
[10] A. Giese, N.A. Stolwijk, H. Bracht, Appl. Phys. Lett. 77 (5) (2000) 642–644.
[11] J.P. Perdew, K. Burke, M. Ernzerhof, Phys. Rev. Lett. 77 (1996) 3865–3868.
[12] A. Carvalho, R. Jones, C. Janke, J.P. Goss, P.R. Briddon, J. Coutinho, S. Öberg, Phys. Rev. Lett. 99 (2007) 175502.
[13] P. Śpiewak, J. Vanhellemont, K. Sueoka, K. Kurzydłowski, I. Romandic, Mater. Sci. Semicond. Process. 11 (5) (2008) 328–331.
[14] C. Janke, R. Jones, S. Öberg, P.R. Briddon, Phys. Rev. B 75 (2007) 195–208.
[15] E. Kamiyama, K. Sueoka, J. Vanhellemont, J. Appl. Phys. 113 (9) (2013) 5.
[16] J.P. Leitão, A. Carvalho, J. Coutinho, R.N. Pereira, N.M. Santos, A.O. Ankiewicz, N. A. Sobotitlev, M. Barroso, J. Lundsgaard Hansen, A. Nylandsted Larsen, P. R. Briddon, Phys. Rev. B 84 (2011) 165211.
[17] N.E.B. Cowern, S. Simdyankin, C. Ahn, N.S. Bennett, J.P. Goss, J.-M. Hartmann, A. Pakfar, S. Hamm, J. Valentin, E. Napolitani, D. De Salvador, E. Bruno, S. Mirabella, Phys. Rev. Lett. 110 (2013) 155501.
[18] S.K. Estreicher, M. Gharaibeh, P.A. Fedders, P. Ordejón, Phys. Rev. Lett. 86 (7) (2001) 1247.
[19] G.M. Lopez, V. Fiorentini, Phys. Rev. B 69 (15) (2004) 155206.
[20] V.P. Markevich, A.R. Peaker, S.B. Lastovskii, L.I. Murin, J. Coutinho, V.J.B. Torres, P.R. Briddon, L. Dobaczewski, E.V. Monakhov, B.G. Svensson, Phys. Rev. B 80 (2009) 235207.
[21] R. Jones, T.A.G. Eberlein, N. Pinho, B.J. Coomer, J.P. Goss, P.R. Briddon, S. Öberg, Nucl. Instrum. Methods Phys. Res. 186 (1) (2002) 10–18.
[22] J. Heyd, G.E. Scuseria, M. Ernzerhof, J. Chem. Phys. 118 (18) (2003) 8207–8215.
[23] J. Heyd, G.E. Scuseria, J. Chem. Phys. 121 (3) (2004) 1187–1192.
[24] G. Kresse, J. Furthmültitler, Phys. Rev. B 54 (1996) 11169–11186.
[25] G. Kresse, D. Joubert, Phys. Rev. B 59 (1999) 1758–1775.
[26] G. Kresse, J. Furthmültitler, Comput. Mater. Sci. 6 (1) (1996) 15–50.
[27] P.E. Blochl, Phys. Rev. B 50 (1994) 17953–17979.
[28] H.J. Monkhorst, J.D. Pack, Phys. Rev. B 13 (1976) 5188–5192.
[29] S.B. Zhang, J.E. Northrup, Phys. Rev. Lett. 67 (1991) 2339–2342.
[30] Christoph Freysoldt, Blazej Grabowski, Tilmann Hickel, J. Neugebauer, Georg Kresse, Anderson Janotti, V. de Waltitle, G. Chris, Rev. Mod. Phys. 86 (2014) 253–305.
[31] C. Freysoldt, J. Neugebauer, C.G. Van de Walle, Phys. Rev. Lett. 102 (2009) 016402.
[32] C. Freysoldt, J. Neugebauer, C.G. Van de Walle, Physica Status Solidi B 248 (5) (2011) 1067–1076.
[33] S. Lany, A. Zunger, Phys. Rev. B 78 (2008) 235104.
[34] G. Zollo, Y.J. Lee, R.M. Nieminen, J. Phys.: Condens. Matter 16 (49) (2004) 8991.
[35] P. Deák, B. Aradi, T. Frauenheim, E. Janzén, A. Gali, Phys. Rev. B 81 (2010) 153203.
[36] J.P. Perdew, M. Levy, Phys. Rev. Lett. 51 (1983) 1884–1887.
[37] F.J. Morin, J.P. Maita, Phys. Rev. 94 (1954) 1525–1529.
[38] R. Jones, A. Carvalho, J. Goss, P. Briddon, Mater. Sci. Eng.: B 159 (2009) 112–116.
[39] T.A.G. Eberlein, N. Pinho, R. Jones, B.J. Coomer, J.P. Goss, P.R. Briddon, S. Öberg, Physica B: Condens. Matter 308 (2001) 454–457.
[40] M. Posselt, F. Gao, D. Zwicker, Phys. Rev. B 71 (2005) 245202.
[41] A. Bongiorno, L. Colombo, F. Cargnoni, C. Gatti, M. Rosati, Europhys. Lett. 50 (5) (2000) 608.
[42] J.G. Simmons, Phys. Rev. 155 (1967) 657–660.
[43] S. Lee, G.S. Hwang, Phys. Rev. B 77 (2008) 085210.
[44] D.A. Richie, J. Kim, S.A. Barr, K.R.A. Hazzard, R. Hennig, J.W. Wilkins, Phys. Rev. Lett. 92 (2004) 045501.

5.7.2 Article 2

A hybrid functional calculation of Tm^{3+} defects in germanium (Ge)

E. Igumbor and W.E. Meyer

Materials Science in Semiconductor Processing 43 (2016) 129133

http://dx.doi.org/10.1016/j.mssp.2015.12.015

Materials Science in Semiconductor Processing 43 (2016) 129–133

Contents lists available at ScienceDirect

Materials Science in Semiconductor Processing

journal homepage: www.elsevier.com/locate/mssp

A hybrid functional calculation of Tm^{3+} defects in germanium (Ge)

E. Igumbor [a,b,*], W.E. Meyer [a,*]

[a] Department of Physics, University of Pretoria, Pretoria 0002, South Africa
[b] Department of Mathematics and Physical Sciences, Samuel Adegboyega University, Km 1 Ogwa/Ehor Rd, Ogwa, Edo State, Nigeria

ARTICLE INFO

Article history:
Received 8 October 2015
Received in revised form
3 December 2015
Accepted 15 December 2015

Keywords:
Defects
Formation energy
Charge state

ABSTRACT

In this work, we present *ab-initio* calculation results for the Tm^{3+} interstitial (Tm_i^{3+}), vacancy–interstitial complex (V_{Ge}-Tm_i^{3+}) and substitutional (Tm_{Ge}^{3+}) defects in germanium (Ge) as determined by the density functional theory (DFT) using the Heyd, Scuseria, and Ernzerhof (HSE06) hybrid functional. We calculated the formation energies and the charge state transition levels of different configurations. Our results show that the Tm^{3+} interstitial exists in the hexagonal configuration with low formation energy. The formation energies for $V_{Ge} - Tm_i^{3+}$ and Tm_{Ge}^{3+} were as low as 0.84 eV. The most energetically favourable defects were the $V_{Ge} - Tm_i^{3+}$ in the *axial* configuration and the Tm_{Ge}^{3+}. The Tm_{Ge}^{3+} and $V_{Ge} - Tm_i^{3+}$ introduced a single acceptor $\epsilon(0/-1)$ charge state transition level that was positioned deep in the middle of the band gap. The majority of the levels induced by the defects under investigation, were either shallow donor or acceptor level lying close to the band gap edges.

1. Introduction

The application of germanium (Ge) in semiconductor material technology is attracting attention due to its high carrier mobilities [1–3]. The use of Ge technology has been successful lately due to the understanding of the role that defects play in it. The role of defects in Ge is well understood from their formation energies and transition charge state levels in the band gap. Studies of electronic properties of elemental radiation induced defects in Ge are relatively scarce and this deficiency recently led towards investigative experimenting and theoretical modelling [4–6] of defects in Ge. Deep level transient spectroscopy (DLTS) [7,8] and infrared absorption spectroscopy [9] studies have succeeded in identifying new radiation induced defects paired with impurities. Perturbed angular correlation spectroscopy (PACs) studies [10,11] have led to important findings on the mobility and electrical activities of vacancies (V) and interstitials (I); and lately, these two defects have been investigated after introduction at low temperature by in situ DLTS [7,8]. Studies of *self-*, *di-* interstitials, vacancies and substitution related defects in Ge have attracted interest in the past decades [12]. Despite the effort made so far in identifying different defects in Ge, there is still more to be accomplished. The rare earth (RE) elements are known to have a partially filled inner 4f shell which gives rise to sharp transitions that are largely insensitive to the crystal host and temperature variations [13–15]. RE element related defects such as Tm doping of ZnO [16], and other materials have been reported [17–21]. Thulium ions (Tm^{3+}) doped materials have been used to generate blue laser emission through non-linear up-conversion of radiation from the infrared to the visible range [17,18,22]. Recently optical properties of Tm-doped materials were studied and EL has been observed from these materials [16,23,19]. Light emission has been attributed to thulium and erbium defects in material [13–15]. Previous studies of RE implanted Si showed sharp emission peaks that were attributed to Tm^{3+} [24]. While the Er was found in interstitial positions as well as in defect complexes [25], the cerium was found to act as an acceptor in a substitutional position in Si [26]. One would expect that Tm^{3+} interstitials or other related defects in Ge will create deep donor levels, however experimental studies of these defects are yet to be performed. In this work, using the hybrid functional of Heyd, Scuseria, and Ernzerhof (HSE06) [27], we have carried out a detailed density functional theory (DFT) calculation of the electronic properties of Tm^{3+} interstitial (Tm_i^{3+}) in the hexagonal (H) configuration, substitutional (Tm_{Ge}^{3+}) and vacancy–interstitial ($V_{Ge} - Tm_i^{3+}$) defects in Ge with a view to finding the most stable defect types from the formation energies of the various charge states. The charge state thermodynamic transition levels were also examined to determine the type of level induced in the band gap by Tm^{3+} defects. The rest of this paper has been organized as follows: in the next section, we present a description of the computational methodology. The results and discussion were presented in Section 3. Finally, we present our concluding remarks in Section 4.

* Corresponding authors.
E-mail addresses: elgumuk@gmail.com (E. Igumbor), wmeyer@up.ac.za (W.E. Meyer).

http://dx.doi.org/10.1016/j.mssp.2015.12.015
1369-8001/

2. Computational details

We performed a DFT electronic structure calculation using the Vienna *ab-initio* Simulation Package (VASP) [28,29]. The Projector-augmented wave (PAW) method, as implemented in the VASP code was used to separate the inert core electrons from the chemically active valence electrons [28,30]. Calculations were carried out using the Heyd, Scuseria, and Ernzerhof (HSE06) [27] hybrid functional. In this approach, the short-range exchange potential is calculated by mixing a fraction of nonlocal Hartree-Fock exchange with the generalized gradient approximation (GGA) functional of Perdew, Burke, and Ernzerhof (PBE) [31]. In contrast to the *local density approximation* and the *generalized gradient approximation* that underestimate the band gap of the semiconductor [32,33], the HSE06 functional gives an excellent description of the electronic band gap and charge state transition properties for a wide range of the defects in group-IV semiconductors [32,34,6]. For the past decades, the study and prediction of the electronic properties of materials with *f* orbital valence electrons was difficult due to the fact that the *f* orbital is highly localized. The highly localized *f* orbitals were previously treated using LDA+U and other methods [35–38]. Recently, density functional theory using hybrid functionals has been successfully implemented, predicting the electronic and band gap properties of several materials with *f* orbital in the valence shell [35,39]. Following the successful implementation of the hybrid functional, it became feasible for us to handle the *f* state in the valence shell of Tm^{3+}. For Ge, the 4 s and 4*p* electrons in the outer shell were treated as valence electrons, while for Tm^{3+}, the 6 s, 5*p* and 4*f* orbitals were considered as valence electrons. For the bulk, geometric optimization of Ge was performed on an 8-atom unit cell with an 8^3 Monkhorst-Pack [40] k-point Brillouin zone sampling scheme and cutoff energy of 600 eV. For the defects, we employed a 64 atom supercell using a 2^3 Monkhorst-Pack [40] k-point Brillouin zone sampling scheme, and we set the plane wave cutoff of the wave function expansion to 400 eV. We refined the geometry until the final change in the total energy was less than 10^{-5} eV and the forces were relaxed to below 0.001 eV/Å. In all the calculations, spin orbit coupling was taken into account. The formation energy (E^f) of defect is derived directly from total energies, allowing the calculation of equilibrium defect *concentrations* [41]. To calculate the defect formation and thermodynamic transition ($\epsilon(q/q')$) levels, we calculated the total energy E(*d*,*q*) for a supercell containing the optimized defect *d* in its charge state *q*. The defect formation energy $E^f(d, q)$ as a function of electron Fermi energy (ε_F) is given as [42,43]

$$E^f(d, q) = E(d, q) - E(pure) + \sum_i (\Delta n)_i \mu_i + q[E_V + \varepsilon_F] + E^q_{cor}, \quad (1)$$

where *E*(*pure*) is a supercell without a defect, $(\Delta n)_i$ is the difference in the number of constituent atoms of type *i* between the supercells, E_V is the valence band maximum (VBM) and μ_i represents the chemical potential of different constituent atoms. Errors in $E^f(d, q)$ due to finite-size effects within the supercell and inaccuracy underlying the approximation of the energy functional, were handled by including a correction term $E_{cor}{}^q$ according to Freysoldt et al. [42,43]. The defect transition energy level $\epsilon(q/q')$ is the Fermi energy for which the formation energy of charge state *q* equals that of charge state q' and is given as [42]

$$\epsilon(q/q') = \frac{E^f(d, q; \varepsilon_F = 0) - E^f(d, q'; \varepsilon_F = 0)}{q' - q} \quad (2)$$

The method proposed by Stephan et al. [44] was used for the calculation of the ionization energy (I_A) related to the conduction band (CBM) and the electron affinity (E_A) related to valence band maximum (VBM). The pristine Kohn–Sham band gap of Ge was calculated to be 0.80 eV, which was higher than the experimental band gap at 0 K. For consistency, we employed the quasiparticle band gap [45,44] calculation. From the calculated I_A and the E_A energies of 4.00 and 3.22 eV respectively, we obtained a Ge band gap of 0.78 eV, which is in agreement with the experimental band gap at 0 K reported by Morin et al. [46]. The binding energies E_b which are defined as the energy required to split up the defects cluster into well separated non-interacting defects were calculated using the method proposed by Zollo et al. [47]. For the V_{Ge}-$Tm_i{}^{3+}$ in the axial configuration, we obtained a binding energy of 4.21 for the neutral state, showing the stability of the V_{Ge}-$Tm_i{}^{3+}$ defect.

3. Results and discussion

3.1. Structural properties and energetics of Tm^{3+} defects in Ge

The relaxed geometric structures of Tm^{3+} defects in Ge are shown in Fig. 1. Fig. 1(a) represent the structure of the $Tm_i{}^{3+}$ in the H configuration. In this configuration, the angle between the defect atom and the nearest Ge atom before and after relaxation was 86° and 94°, respectively. The interstitial atom caused a change in atomic position after relaxation which led to a bond length reduction between the Tm and Ge atoms by 0.05 Å. The geometric structures of the V_{Ge}-$Tm_i{}^{3+}$ in both the *axial* and *basal* configurations are displayed in Figs. 1(b) and (c), respectively. In both configurations, after relaxation, the bond lengths between the defect atom and its two nearest Ge neighbours were reduced from 2.88 to 2.71 Å and from 3.02 to 2.92 Å. For the V_{Ge}-$Tm_i{}^{3+}$, the bond angle between the Tm atom and two nearest Ge neighbours was reduced from 52.7^0 to 51.3^0. It was interesting to note that the same change of bond length and bond angle was observed in both the *axial* and *basal* configurations except that the position of the vacancy atom differed. The geometric structure of the Tm_{Ge}^{3+} is shown in Fig. 1(d). The introduction of the substitutional defect led to structural rearrangement of the Ge crystal supercell. After the relaxation of

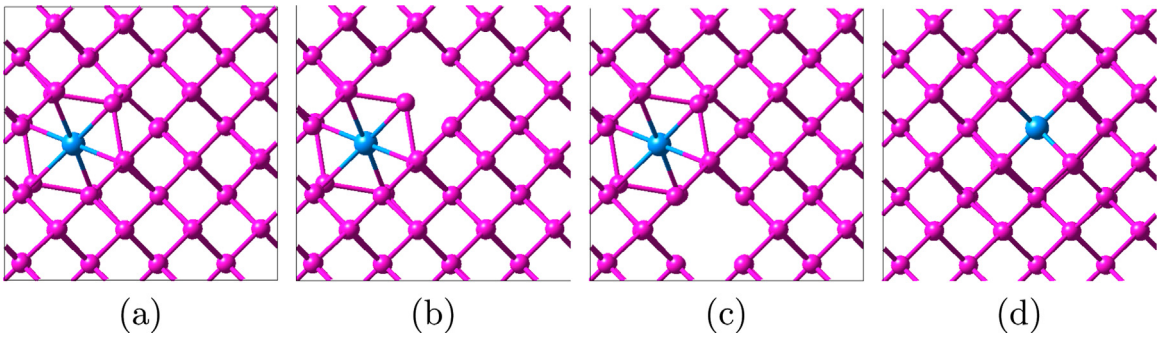

Fig. 1. The relaxed structures of Tm^{3+} defects in Ge, defect atom in blue and the wide space in the crystal structure indicating the position of the Ge vacancy; (a) H configuration of Tm_i^{3+}, (b) V_{Ge}-$Tm_i{}^{3+}$ *(axial)* (c) V_{Ge}-$Tm_i{}^{3+}$ (*basal*) and (d) Tm_{Ge}^{3+}.

Table 1
Calculated formation energies (E^f) in eV at ϵ_f=0 of Tm^{3+} interstitial (Tm_i^{3+}), substitutional (Tm_{Ge}^{3+}) and vacancy–interstitial complex (V_{Ge}-Tm_i^{3+}) in Ge. The result of the Tm_i^{3+} tetrahedral configuration was from Ref. [48].

Defect	Configuration	−2	−1	0	+1	+2
Tm_i^{3+}	*tetrahedral*	3.94	2.75	1.81	0.89	0.24
	hexagonal	4.35	3.37	2.73	2.18	1.96
$V_{Ge} - Tm_i^{3+}$	*axial*	2.55	1.87	1.39	1.04	0.84
	basal	6.93	6.29	5.75	5.31	5.04
Tm_{Ge}^{3+}		3.37	2.64	2.12	1.92	1.83

the Tm_{Ge}^{3+}, the bond length and bond angle which it forms with the nearest Ge atoms reduced by 0.01 Å and 0.9° respectively.

3.2. Properties and energetics of Tm_i^{3+}

The energy of formation (E^f) for the positive, neutral and negative charge states of Tm_i^{3+}, V_{Ge}-Tm_i^{3+} and Tm_{Ge}^{3+} are presented in Table 1. For the Tm_i^{3+} in the hexagonal (H) configuration, the formation energies varied from 4.35 to 1.96 eV. The E^f decreased from the double negative to the double positive charge states. The formation energies of the defects in their charged states were low, and the charge state +2 had the lowest formation energy at $\varepsilon_F = 0$. The low formation energies of Tm_i^{3+} in the H configuration for all the charge states suggested that under equilibrium conditions, Tm_i^{3+} can form relatively easily. It should be noted that, even though the formation energies for Tm_i^{3+} in the H configuration were low, the Tm_i^{3+} was more energetically favourable (in all charge states) in the tetrahedral (T) configuration [48] (see Table 1). The formation energies of Tm_i^{3+} in its charge states as a function of ε_F are shown in Fig. 2(b). The Tm_i^{3+} defect introduced transition state levels in the band gap that were either single acceptor or double donor. The energy level of the acceptor state related to the valence band maximum (VBM) was $\epsilon(0/-1) = 0.65$ eV and the other transition levels were $\epsilon(+1/0) = 0.55$ eV and $\epsilon(+1/+2) = 0.22$ eV above the VBM for the single and double donors respectively. The −1, 0, +1, and +2 charge states were thermodynamically accessible. Charge state −2 was not thermodynamically stable for any Fermi-level in the band gap. The difference in energy level between $\epsilon(+1/0)$ and $\epsilon(0/-1)$ was 0.10 eV. The H configuration, although not the most energetically stable configuration of Tm_i^{3+} displayed some transition levels as reported above that were not found in the T configuration. The T configuration exhibited only the properties of shallow double donor level at E_C − 0.04 eV [48] (see Fig. 2(a)). The interaction energy between two electrons in a two-level defect is referred to as Hubbard *U*. Fig. 2 (b) shows that the Tm_i^{3+} impurity has a *positive-U* property with small *effective-U* value of 0.09 eV (Table 2).

3.3. Properties and energetics of V_{Ge}-Tm_i^{3+}

In this defect, we have two major configurations namely: the *axial* and *basal* configurations derived from the position of the vacancy atom, see Fig. 1(b) and (c). In Table 1, we show that the formation energies of V_{Ge}-Tm_i^{3+} for charge states −2 to +2 varied from 0.84 to 2.55 eV and from 5.04 to 6.93 for the *axial* and *basal* configurations, respectively. In both configurations, the E^f decreased from the double negative to the double positive charge states. The formation energies of the charged states were relatively low. In both configurations, the +2 charge state had the lowest formation energy at $\varepsilon_F = 0$ compared to other charge states. The *axial* configuration has lower formation energies than the *basal* configuration in all the charge states. The low formation energies indicate that the V_{Ge}-Tm_i^{3+} defect can form easily in the two different configurations. It is interesting to know that the formation energies of the V_{Ge}-Tm_i^{3+} in the *axial* configuration were lower than that of the Tm_i^{3+} in the H configuration, while for the Tm_i^{3+} in the H configuration, the formation energies for all the charge states were lower than that of the *basal* configuration of the V_{Ge}-Tm_i^{3+}. The plot of the formation energies of V_{Ge}-Tm_i^{3+} in its charge states as a function of ε_F are shown in Fig. 2(c) and (d) for both the *axial* and *basal* configurations, respectively. For both configurations, the defect introduced both acceptor and donor levels that were deep lying within the band gap. For the *axial* configuration, double $\epsilon(-1/-2)$ and single $\epsilon(0/-1)$ acceptor levels were found lying close to the CBM and close to the middle of the band gap, respectively. This same trend was also observed for the *basal* configuration. While the $\epsilon(-1/-2)$ transition level for the *axial* configuration was 0.10 eV away from the CBM, for the *basal* configuration it was 0.14 eV away from the CBM. V_{Ge}-Tm_i^{3+} also introduced other transition states, single $\epsilon(+1/0)$ and double $\epsilon(+1/+2)$ donor levels in the band gap. As was observed for the acceptor levels, the donor levels were close to the band edges. For the $\epsilon(+1/0)$ level, it was near the middle of the band gap for both configurations. While the $\epsilon(+2/+1)$ for the *axial* configuration was 0.19 eV away from the VBM, for the *basal* configuration, it was 0.27 eV away from the VBM. In both configurations, all the charge states (+2 to −2) were thermodynamically accessible and stable for some values of the Fermi-level, but this was not the case for the Tm_i^{3+} where we found that the defect was never stable in the negative 2 charge state. As was observed in the Tm_i^{3+}, both the *axial* and *basal* configurations displayed *positive-U* behaviour with small *effective-U* values of 0.23 and 0.10 eV, respectively.

3.4. Properties and energetics of Tm_{Ge}^{3+}

The formation energies of the positive, neutral and negative charge states of Tm_{Ge}^{3+}, as shown in Table 1, show a decrease from the double negative to the double positive charge states. The formation energies varied from 1.83 to 3.37 eV. The formation energy of the Tm_{Ge}^{3+} is relatively low, although higher than that of the V_{Ge}-Tm_i^{3+} for the *axial* configuration, and lower than the formation energies of both the Tm_i^{3+} in the H configuration and V_{Ge}-Tm_i^{3+} in the (*basal* configuration) in all the charge states. In this present work, the sequence of formation energy from high to low was V_{Ge}-Tm_i^{3+} (*basal*) > Tm_i^{3+} > Tm_{Ge}^{3+} > $V_{Ge} - Tm_i^{3+}$ (*axial*). In our results, the Tm_{Ge}^{3+} substitutional defect was energetically more favourable than the interstitial in the H configuration, but the T configuration was energetically much more favourable than the Tm_{Ge}^{3+} as was discussed in our earlier work [48]. The plot of the formation energy of Tm_{Ge}^{3+} in its charge states as a function of ε_F is shown in Fig. 2(e). The defect introduced a double acceptor level at $\epsilon(-1/-2)$, lying close to the edge of the band gap (CBM) at E_C − 0.05 eV. The donor levels induced by Tm_{Ge}^{3+} in the band gap were a double donor at $E_V + 0.10$ and a single donor at $E_V + 0.19$ eV. The Tm_{Ge}^{3+} defect in Ge also induced a $\epsilon(0/-1)$ transition level lying at the middle of the band gap. The Tm_{Ge}^{3+} displayed *positive-U* behaviour with a small *effective-U* value of 0.32 eV. We show that not only Tm_i^{3+} interstitial defects in Ge occur at a low formation energy in all the charge states but that this also applies to the V_{Ge}-Tm_i^{3+} and Tm_{Ge}^{3+} defects.

4. Summary

We have carried out detailed calculations of Tm^{3+} (interstitial, vacancy-complex and substitution) related defects in Ge, using a hybrid functional (HSE06) in the framework of density functional

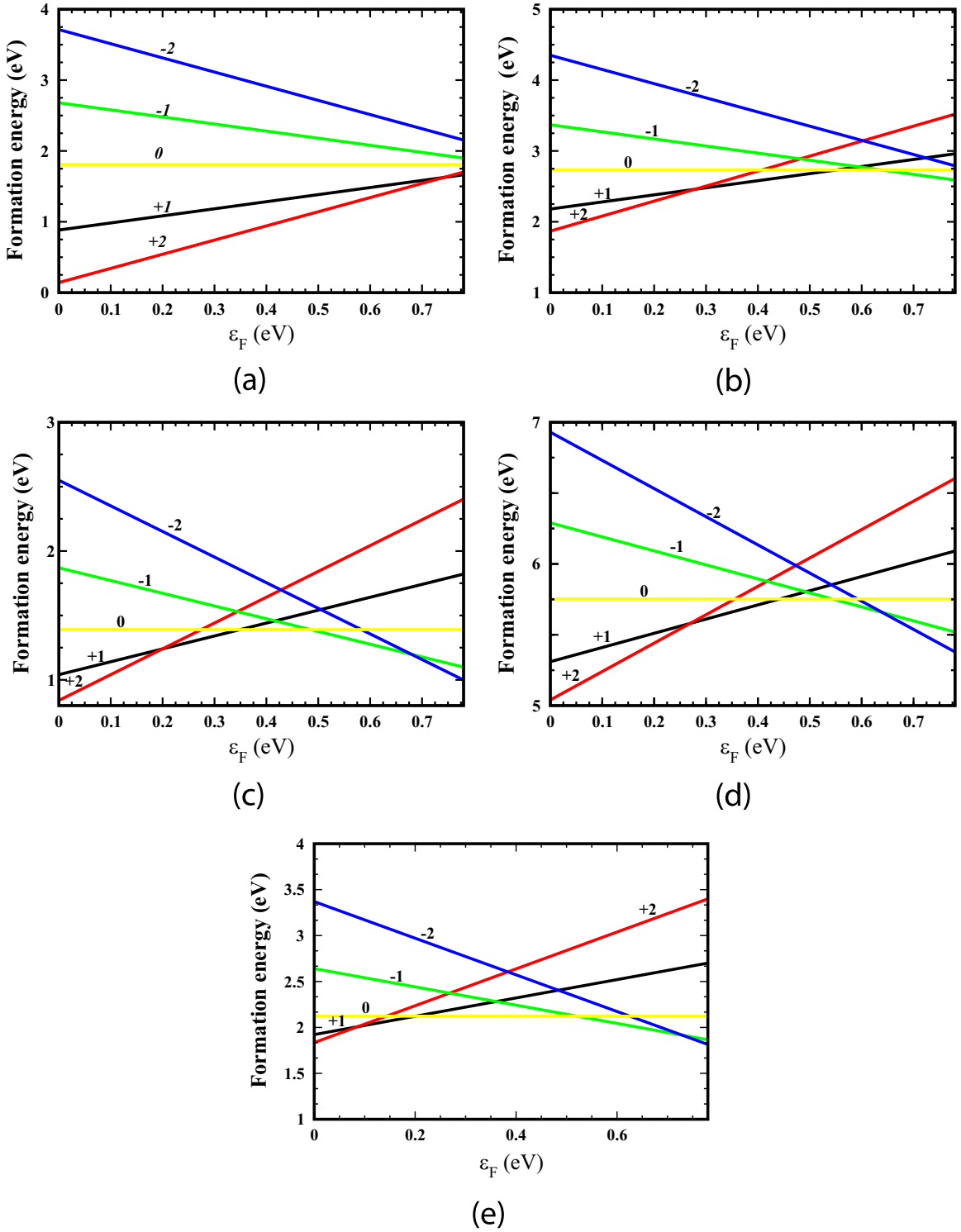

Fig. 2. Plot of formation energy as a function of the Fermi energy for the Tm_i^{3+}, V_{Ge}-Tm_i^{3+} (*axial* and *basal*) and substitution Tm_{Ge}^{3+} in Ge; (a) *tetrahedral* configuration of Tm_i^{3+}, (b) *hexagonal* configuration of Tm_i^{3+}, (c) V_{Ge}-Tm_i^{3+} configuration (*axial*), (d) V_{Ge}-Tm_i^{3+} configuration (*basal*) and (e) Tm_{Ge}^{3+}.

theory (DFT). The formation energies and thermodynamic charge transition levels were described in detail. We have shown that the formation of Tm_i^{3+} in the hexagonal configuration, Tm_{Ge}^{3+}, and V_{Ge}-Tm_i^{3+} for two configurations (*axial* and *basal*) defects in Ge exist with low formation energies. Our calculation shows that V_{Ge}-Tm_i^{3+} in the *axial* configuration had the lowest formation energy for the neutral, negative and the positive charge states. We have shown also that Tm_{Ge}^{3+} forms with a lower formation energy than the Tm_i^{3+} for the H configurations. In addition to the low formation energies, we have shown that Tm_i^{3+}, Tm_{Ge}^{3+}, and V_{Ge}-Tm_i^{3+} defect introduced transition levels of $(0/-1)$ and $(+1/0)$ that were lying deep in the band gap. The V_{Ge}-Tm_i^{3+} and Tm_{Ge}^{3+} introduced additional $(+1/+2)$ and $(-1/-2)$ levels that were lying close to the band edges. Unlike the Tm_{Ge}^{3+} and V_{Ge}-Tm_i^{3+} that acts as a double acceptor $(-1/-2)$, the Tm_i^{3+} does not act as a double acceptor instead, this level lies inside the CBM. We expect

Table 2
The energy of the thermodynamic transition levels $\epsilon(q/q')$ above E_V (eV) for the Tm^{3+} interstitial, substitution and vacancy-interstitial complex in Ge.

Charge states	Tm_i^{3+} (T)	Tm_i^{3+} (H)	$V_{Ge} - Tm_i^{3+}$ (*basal*)	$V_{Ge} - Tm_i^{3+}$ (*axial*)	Tm_{Ge}^{3+}
(−1/−2)	–	–	0.64	0.68	0.73
(0/−1)	–	0.65	0.55	0.48	0.52
(+1/0)	–	0.55	0.44	0.34	0.19
(+2/+1)	0.74 [48]	0.22	0.27	0.19	0.10

the data and information presented to be useful in the process modelling of Ge-based devices.

Acknowledgements

This work is based on the research supported partly by National Research foundation (NRF) of South Africa (Grant specific unique reference number (UID) 78838). The opinions, findings and conclusion expressed are those of the authors and the NRF accepts no liability whatsoever in this regard. The authors also acknowledged MedeA VASP.

Appendix A. Supplementary data

Supplementary data associated with this article can be found in the online version at http://dx.doi.org/10.1016/j.mssp.2015.12.015.

References

[1] L. Lee, E.A. Fitzgerald, T. Bulsara, Mayank, T. Currie, A. Lochtefeld, J. Appl. Phys. 97 (1) (2005) 011101.
[2] H. Tahini, A. Chroneos, R.W. Grimes, U. Schwingenschlgl, A. Dimoulas, J. Phys. Condens. Matter 24 (19) (2012) 195802.
[3] M. Houssa, A. Satta, E. Simoen, B. De, M. Jaeger, M. Caymax, M. Heyns, Germanium-Based Technol.: From Mater. Devices (2011) 233.
[4] A. Chroneos, H. Bracht, Appl. Phys. Rev. 1(1) 011301.
[5] J. Coutinho, R. Jones, P.R. Briddon, S. Öberg, Phys. Rev. B 62 (2000) 10824–10840.
[6] E. Igumbor, C. Ouma, G. Webb, W. Meyer, Phys. B: Condens. Matter 480 (2016) 191–195.
[7] C. Nyamhere, M. Das, F.D. Auret, A. Chawanda, Phys. Status Solidi (c) 5 (2) (2008) 623–625.
[8] F. Auret, P.J. van Rensburg, M. Hayes, J. Nel, S. Coelho, W. Meyer, S. Decoster, V. Matias, A. Vantomme, D. Smeets, Nuclear Instruments and Methods in Physics Research Section B: Beam Interactions with Materials and Atoms 257 (1–2) (2007) 169–171.
[9] J. Fage-Pedersen, A.N. Larsen, A. Mesli, Phys. Rev. B 62 (2000) 10116–10125.
[10] H. Haesslein, R. Sielemann, C. Zistl, Phys. Rev. Lett. 80 (1998) 2626–2629.
[11] R. Sielemann, Nuclear Instrum. Methods Phys. Res. 146 (14) (1998) 329–340.
[12] C. Claeys, E. Simoen, Germanium-based Technologies: From Materials to Devices, Elsevier, 2011.
[13] M. Lourenço, C. Opoku, R. Gwilliam, K. Homewood, Opt. Mater. 32 (12) (2010) 1597–1600.
[14] A. Polman, J. Appl. Phys. 82 (1) (1997) 1–39.
[15] M.A. Loureno, R.M. Gwilliam, K.P. Homewood, Appl. Phys. Lett. 92(16).
[16] F. Fang, A. Ng, X. Chen, A. Djurii, Y. Zhong, K. Wong, P. Fong, H. Lui, C. Surya, W. Chan, Mater. Chem. Phys. 125 (3) (2011) 813–817.
[17] L.C. Courrol, I.M. Ranieri, S.L. Baldochi, R.E. Samad, A.Z. de Freitas, L. Gomes, N. D. Vieira, Opt. Commun. 270 (2) (2007) 340–346.
[18] R. Paschotta, P.R. Barber, A.C. Tropper, D.C. Hanna, J. Opt. Soc. Am. B 14 (5) (1997) 1213–1218.
[19] T. Monteiro, A.J. Neves, M.J. Soares, M.C. Carmo, M. Peres, E. Alves, E. Rita, Appl. Phys. Lett. 87 (19) (2005).
[20] W. Jadwisienczak, H. Lozykowski, A. Xu, B. Patel, J. Electron. Mater. 31 (7) (2002) 776–784.
[21] E. Rita, E. Alves, U. Wahl, J. Correia, A. Neves, M. Soares, T. Monteiro, Phys. B: Condens. Matter 340–342 (0) (2003) 235–239.
[22] T. Andreev, N.Q. Liem, Y. Hori, M. Tanaka, O. Oda, D.L.S. Dang, B. Daudin, B. Gayral, Phys. Rev. B 74 (2006) 155310.
[23] M. Peres, J. Wang, M. Soares, A. Neves, T. Monteiro, E. Rita, U. Wahl, J. Correia, E. Alves, Superlattices and Microstruct. 36 (4–6) (2004) 747–753.
[24] G.S. Pomrenke, E. Silkowski, J.E. Colon, D.J. Topp, Y.K. Yeo, R.L. Hengehold, J. Appl. Phys. 71(4).
[25] H. Przybylinska, W. Jantsch, Y. Suprun-Belevitch, M. Stepikhova, L. Palmetshofer, G. Hendorfer, A. Kozanecki, R.J. Wilson, B.J. Sealy, Phys. Rev. B 54 (1996) 2532–2547.
[26] Y. Miyata, Y. Nose, T. Yoshimura, A. Ashida, N. Fujimura, J. Cryst. Growth 425 (2015) 158–161.
[27] J. Heyd, G.E. Scuseria, M. Ernzerhof, J. Chem. Phys. 118 (18) (2003) 8207–8215.
[28] G. Kresse, J. Furthmüller, Phys. Rev. B 54 (1996) 11169–11186.
[29] G. Kresse, D. Joubert, Phys. Rev. B 59 (1999) 1758–1775.
[30] P.E. Blochl, Phys. Rev. B 50 (1994) 17953–17979.
[31] J.P. Perdew, K. Burke, M. Ernzerhof, Phys. Rev. Lett. 77 (1996) 3865–3868.
[32] H. Tahini, A. Chroneos, R.W. Grimes, U. Schwingenschlgl, H. Bracht, Appl. Phys. Lett. 99(7) 072112.
[33] P. Śpiewak, J. Vanhellemont, K. Sueoka, K. Kurzydłowski, I. Romandic, Mater. Sci. Semicond. Process. 11 (5) (2008) 328–331.
[34] P. Deák, B. Aradi, T. Frauenheim, E. Janzén, A. Gali, Phys. Rev. B 81 (2010) 153203.
[35] B.G. Janesko, T.M. Henderson, G.E. Scuseria, Phys. Chem. Chem. Phys. 11 (3) (2009) 443–454.
[36] V.I. Anisimov, J. Zaanen, O.K. Andersen, Phys. Rev. B 44 (3) (1991) 943.
[37] L. Petit, A. Svane, Z. Szotek, W.M. Temmerman, Phys. Rev. B 72 (20) (2005) 205118.
[38] M. Cococcioni, S.De. Gironcoli, Phys. Rev. B 71 (3) (2005) 035105.
[39] J.L. Da Silva, M.V. Ganduglia-Pirovano, J. Sauer, V. Bayer, G. Kresse, Phys. Rev. B 75 (4) (2007) 045121.
[40] H.J. Monkhorst, J.D. Pack, Phys. Rev. B 13 (1976) 5188–5192.
[41] S.B. Zhang, J.E. Northrup, Phys. Rev. Lett. 67 (1991) 2339–2342.
[42] Freysoldt, Christoph, Grabowski, Blazej, Hickel, Tilmann, J. Neugebauer, Kresse, Georg, Janotti, Anderson, V. de Walle, C.G., Rev. Mod. Phys. 86 (2014) 253–305.
[43] Y. Kumagai, F. Oba, Phys. Rev. B 89 (2014) 195205.
[44] S. Lany, A. Zunger, Phys. Rev. B 78 (23) (2008) 235104.
[45] J.P. Perdew, M. Levy, Phys. Rev. Lett. 51 (1983) 1884–1887.
[46] F.J. Morin, J.P. Maita, Phys. Rev. 94 (1954) 1525–1529.
[47] G. Zollo, Y.J. Lee, R.M. Nieminen, J. Phys.: Condens. Matter 16 (49) (2004) 8991.
[48] E. Igumbor, W.E. Meyer, conference proceeding of the 60th Annual Conference of the South African Institute of Physics submitted to SAIP Journal. Phys (2015).

5.7.3 Article 3

Rare earth interstitials in Ge: a hybrid density functional theory study

E. Igumbor, R. C. Andrew and W. E. Meyer

Journal of Electronic Materials (JEMS)

doi:10.1007/s11664-016-5062-8

Journal of ELECTRONIC MATERIALS
DOI: 10.1007/s11664-016-5062-8

Rare Earth Interstitials in Ge: A Hybrid Density Functional Theory Study

E. IGUMBOR,[1,2,3] R.C. ANDREW,[1] and W.E. MEYER[1,4]

1.—Department of Physics, University of Pretoria, Pretoria 0002, South Africa. 2.—Department of Mathematical and Physical Sciences, Samuel Adegboyega University, Ogwa, Edo State, Nigeria. 3.—e-mail: elgumuk@gmail.com. 4.—e-mail:wmeyer@up.ac.za

In this work, the results of density functional theory calculations for rare earth (Ce, Pr, Eu, and Er) interstitials in Ge are presented. We employed the hybrid functional of Heyd, Scuseria, and Ernzerhof (HSE06) for all the calculations. We calculated the formation energies and charge state transition levels for the tetrahedral (T) and hexagonal (H) configurations of the Ce, Pr, Eu, and Er interstitials in Ge. While for the T configuration, the charge states of the Ce and Pr did not induce any thermodynamic accessible transition state level within the band gap of Ge, for both the T and H configurations the Eu and Er interstitials in Ge induce deep levels in the band gap. The H configuration of the Ce interstitial in Ge induces a shallow donor level at 0.03 eV below the conduction band. The Eu interstitial exhibits *negative-U* properties for the (+2/−2) transition level and the Er interstitial displays characteristics of charge state controlled metastability.

Key words: Defect, rare earth, formation energy, charge state

INTRODUCTION

In recent years, rare earth (RE) doping and defects in materials have been extensively studied because of their potential applications in full colour emission devices.[1,2] A study revealed that the *intra-4f* shell electronic transitions of the RE ions give rise to sharp emission lines with small energy dispersion.[3] It has been suggested that deep-level defects participate in the energy transfer process from the host to the RE^{3+} ions.[4] Therefore, the structure of the local environment of RE^{3+} ions plays a crucial role in the determination of the optical luminescence efficiency of RE doped semiconductors.[1] The size of the RE ion, the number of valence electrons, and its electronegativity may differ from the host, and thus it is expected that the RE could induce one or more gap levels occupied by valence electrons.[5] Studies of defects in semiconductor materials have been carried out in the last two decades, in particular defects in Si[5] and only a few in Ge[2,6–8] (due to problems with the density functional theory predicting a band gap). While the former has a band gap of 1.17 eV,[9] the latter has a narrow band gap of 0.78 eV[10] at 0 K. The narrow band gap of Ge, its high carrier mobility, and low voltage have made it a possible alternative to Si as an active layer in advanced electronic devices.[11,12] Impurities influence Ge-based semiconductor devices either positively or negatively.[6] Several experimental and theoretical studies of point defects such as vacancy[13] and interstitial[6,7] defects in Ge have been reported in the literature. While RE ion defects in Si and other materials have been studied both theoretically and experimentally,[14–16] except for Tm,[2,8] the structural and electronic properties of RE interstitial defects in Ge have not been experimentally or theoretically reported. In order to provide an insight for the experimental study of the electronic properties of defects resulting from the implantation of RE, we have used the Heyd, Scuseria, and Ernzerhof (HSE06) functional[17] in the framework of density functional theory (DFT) to calculate the electronic properties of the Ce, Pr, Eu, and Er interstitials in Ge in two different configurations: the tetrahedral (T) and hexagonal (H). The

(Received February 25, 2016; accepted October 13, 2016)

Published online: 28 October 2016

energies of formation for the T and H configurations of the Ce, Pr, Eu, and Er interstitials in Ge were calculated for charge states $(-2, -1, 0, +1, +2)$. The charge state transition levels are examined and presented as well. The role of shallow and deep levels, charge state controlled metastability and *negative-U* properties of charge state transition levels are also discussed. This article is organised as follows: in "Computational Details" section, we present the computational details, the result and discussion are presented in "Results and Discussion" section, and finally, we present our concluding remarks in "Summary" section.

COMPUTATIONAL DETAILS

DFT electronic structure calculations were performed using the Vienna ab initio Simulation Package (VASP).[18,19] We used the projector-augmented wave (PAW) method, as implemented in the VASP code to separate the inert core electrons from the chemically active valence electrons.[18,20] All the calculations were carried out using the Heyd, Scuseria, and Ernzerhof (HSE06)[17] hybrid functional. In this approach, the short-range exchange potential is calculated by mixing a fraction (25%) of exact nonlocal Hartree-Fock exchange with the generalized gradient approximation (GGA) functional of Perdew, Burke, and Ernzerhof (PBE).[21] In contrast to the local density approximation (LDA) and the GGA that tend to underestimate the band gap of semiconductors,[12,22,23] the HSE06 functional gives an excellent description of the electronic band gap and charge state transition properties for a wide range of the defects in group-IV semiconductors.[7,9,22] For the past decade, the study and prediction of the electronic properties of materials with the *f* orbital valence shell was difficult because the *f* orbital is highly localized. The highly localized *f* orbital was previously treated using LDA + U and other methods.[24–27] Recently, the hybrid functional has been successfully used to predict the electronic and band gap properties of several materials with an *f* orbital in the valence shell.[24,28] Following this success of the hybrid functional, it became feasible for us to handle the *f* orbital in the valence shell of the RE. For Ge, the 4*s* and 4*p* electrons in the outer shell were treated as valence electrons, while depending on the electronic configurations, the 6*s*, 5*d*, 5*p*, and 4*f* orbitals in the outer shell were treated as valence electrons for the Ce, Eu, Er, and Pr. For the bulk, geometric optimization of Ge was performed using an eight-atom unit cell with an 8^3 Monkhorst-Pack[29] *k*-point Brillouin zone sampling scheme and cutoff energy of 400 eV. For the defects, we employed a 64-atom supercell using a 2^3 Monkhorst-Pack[29] *k*-point Brillouin zone sampling scheme, and we set the plane wave cutoff of the wave function expansion to 400 eV. We refined the geometry until the change in the total energy was less than 10^{-5} eV and the forces were relaxed to below 0.001 eV/Å. The energy of formation of a system is strongly dependent on the spin-orbit coupling (SOC) due to the presence of relativistic effects in heavy atomic systems. To deal with the scalar relativistic effect, the mass-velocity and Darwin correction terms have been incorporated into the PAW potential. In addition to the scalar relativistic effect that was taken into account, spin-orbit coupling was also taken into account for all calculations. The *concentrations* (C) of defects in thermodynamic equilibrium are related to the formation energy (E^f) through the Boltzmann constant (k_B)

$$C = N_0 \exp\left(-E^f / k_B T\right), \tag{1}$$

where T is temperature in Kelvin and N_0 is the number of sites in the crystal where the defect can occur per unit volume. For a charged system, the energy of formation of the defect in its charged state depends on the Fermi level (ε_F). The formation energy (E^f) of a defect is derived directly from total energies calculated by DFT, allowing the calculation of equilibrium defect *concentrations*.[30] To calculate the defect formation and thermodynamic transition energy $(\epsilon(q/q'))$ levels, we calculated the total energy $E(d, q)$ for a supercell containing the optimized defect d in its charge state q. The defect formation energy $E^f(d,q)$ as a function of electron Fermi energy (ε_F) is given as[31]

$$\begin{aligned} E^f(d,q) = E(d,q) - E(\text{pure}) + \sum_i (\Delta n)_i \mu_i \\ + q[E_V + \varepsilon_F] + E^q_{cor}, \end{aligned} \tag{2}$$

where E(pure) is the energy of a supercell without a defect, $(\Delta n)_i$ is the difference in the number of constituent atoms of type i between the pristine supercell and the supercell containing the defect, μ_i represents the chemical potential of different constituent atoms, and E_V is the valence band maximum (VBM). The correction term E^q_{cor} according to Freysoldt et al.[32] has been included to account for the discrepancies surrounding the calculation of $E^f(d,q)$ due to finite-size effects within the supercell and inaccuracy underlying the approximation of the energy due to electrostatic interactions. According to Eq. 1, an increase in the formation energy of a defect obtained from Eq. 2 leads to a decrease in the concentration of a defect, and the defect becomes less energetically favourable. The defect transition energy level $\epsilon(q/q')$ is the Fermi energy at which two charge states (q and q') of the defect have the same energy of formation, and is given as[32]

$$\epsilon(q/q') = \frac{E^f(d,q;\varepsilon_F = 0) - E^f(d,q';\varepsilon_F = 0)}{q' - q} \tag{3}$$

As reported in Ref. 7, we took the modelled band gap of the pristine Ge to be 0.78 eV.

RESULTS AND DISCUSSION

Structural Properties of RE Interstitials in Ge

In order to find out the most energetically favourable structure for the neutral charge state of RE interstitials in Ge, two different atomic arrangement were considered: the hexagonal (H) and tetrahedral (T) configurations. The relaxed geometric structures of RE interstitials in Ge are shown in Figs. 1 and 2, for the T and H configurations, respectively. Table I lists the predicted shortest bond distance (Å) between RE and Ge atoms, before geometric relaxation (α_d), after geometric relaxation (β_d), and the difference (Δ_d) between α_d and β_d for the T and H configurations of RE interstitials in Ge. The shortest bond length between RE and Ge atoms was calculated with respect to the nearest neighbour Ge atom.

Figure 1a and b represent the relaxed geometric structures of the Ce and Pr interstitials in Ge, respectively, for the T configuration. For this configuration, while Fig. 1c represents the relaxed geometric structure of the Eu interstitial in Ge, Fig. 1d represents the relaxed geometric structure of the Er interstitial in Ge. For the H configuration, Fig. 2a–c represent the relaxed geometric structures of the Ce, Pr, and Eu interstitials in Ge, respectively. The relaxed geometric structure of the Er interstitial in Ge for the H configuration is displayed in Fig. 2d as well. After geometric relaxation, the shortest bond distance between a RE and its nearest-neighbour Ge atoms for both the T and H configurations decreased. The bond length between Ce and Ge atoms decreases by 0.03 Å and 0.06 Å for the T and H configurations, respectively. The Pr

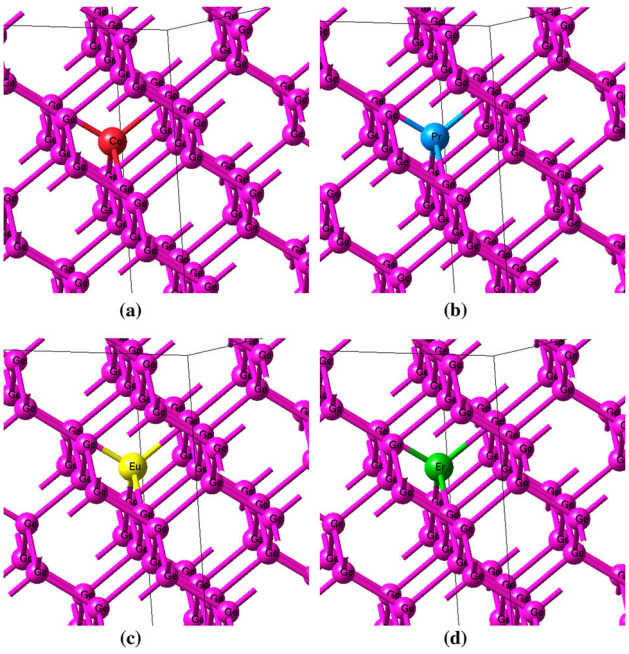

Fig. 1. Relaxed geometric structures for the T configuration of RE interstitials in Ge. (a) Ce, (b) Pr, (c) Eu, and (d) Er.

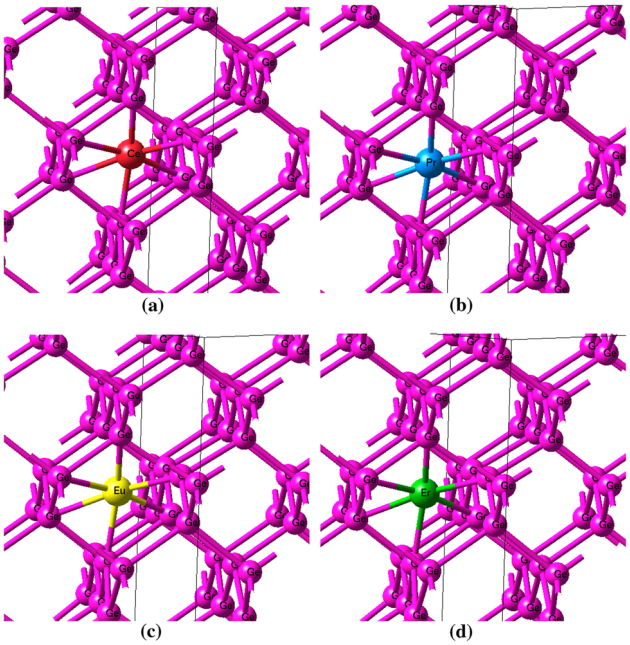

Fig. 2. Relaxed geometric structures for the H configuration of RE interstitials in Ge. (a) Ce, (b) Pr, (c) Eu, and (d) Er.

and Ge atoms' bond length decreased by 0.02 Å in the T configuration and by 0.03 Å in the H configuration. For the Eu and Er interstitials in Ge, after structural relaxation, the shortest bond length between Eu and Ge and Er and Ge atoms decreased by 0.06 Å (for Eu–Ge) and 0.01 Å (for Er–Ge) for the T configuration. For the H configuration, while the Eu and Ge atoms' bond length decreased by 0.08 Å after geometric relaxation, the Er and Ge atoms' shortest bond length decreased by 0.03 Å. For all RE interstitials in Ge, we found that all the shortest bond lengths between RE and Ge atoms decreased within 0.8 Å. We have observed that for all RE interstitials in Ge studied, the RE and Ge shortest bond distance, as well as the reduction in bond length after structural relaxation for the T configuration are lower than that of the H configuration. This suggests that the RE interstitials in Ge experience more bond length strain in the H configuration than the T configuration and should be the key to understanding the difference in the formation energies for both configurations.

Projected Density of States of RE Interstitials in Ge

The plot of electronic properties [spin polarised projected density of states (PDOS)] of RE interstitials in Ge for the T and H configurations are shown in Fig. 3. The majority (spin-up) and minority (spin-down) density of states are shown as right and left halves of each plot, respectively. For the pristine Ge, the majority and minority spins are symmetrical for the entire plot [as shown in insert (o) of Fig. 3],

suggesting non-spin polarization of the system. RE interstitials in Ge for all defects considered show strong evidence of hybridization between the *s* and *p* orbitals of participating atoms. For the Er interstitial in Ge, in the H configuration, orbital states are densely populated both in the conduction band minimum and valence band maximum [see insert (a) of Fig. 3]. But for the T configuration, we observed significant contribution of the orbital states in the conduction band minimum, below the Fermi level [see insert (b) of Fig. 3]. Nevertheless, in contrast to the T configuration, which did not show any full metallic behaviour, the PDOS of the H configuration of the Er interstitial in Ge exhibits metallic character. For the Eu interstitial [insert (c) and (d) of Fig. 3], the defect induced orbital states in the band gap for both the T and H configurations, resulting in 0 band width. This suggests that as a result of the defect introduced, the entire system becomes metallic. For the Ce interstitial in Ge, apart from the hybridization that occurred between the *s* and *p* orbitals, the band width of the T configuration is higher than that of the H configuration. More orbital states are found below the Fermi level at the conduction band minimum for the T than that of the H configuration as shown in insert (f) and (e), respectively, of Fig. 3. This same trend is observed for the Pr interstitial in Ge. where the difference between the band width of the T and H configurations is 0.37 eV. Except for the Pr, all other RE interstitial in Ge studied are spin polarised. Figure 3 shows that some RE interstitials in Ge introduced states within the band gap of Ge. Depending on the RE, RE interstitials in Ge induced orbital states appear to be either deep (in the middle of the band gap of Ge) or shallow (appearing within the band gap, but close to the either conduction band minimum or valence band maximum). It is noted that apart from Eu, RE interstitials in Ge for the T configuration induces fewer orbital states in the band gap of Ge than the H configuration. This could play a major role in predicting the sequence of the formation energy of RE interstitials in Ge.

In order to understand the bonding characteristic and charge transfer (relative to host atoms) for the T configuration of RE interstitials in Ge, we performed total charge density calculation. Table II shows the charge transfer between a RE interstitial atom relative to host atoms. Our results show that there is charge transfer between participating RE and Ge atoms. The Pr and Ce have the least charge transfer of 1.04 *e* and 1.05 *e* with Ge. The Eu, on the other hand, has the highest charge transfer of 1.42 *e* with Ge atom compared to the other participating RE.

Formation Energies of RE Interstitials in Ge

The results of the formation energies of the Ce, Pr, Eu, and Er interstitials in Ge are tabulated in Table III. The formation energies for the T and H configurations of the Ce interstitial in Ge increase from +2 to the −2 charge state. The energies of formation of the Ce interstitial in Ge for both the T and H configurations are between −4.45 eV and 2.61 eV for all charge states. In addition, the T configuration has lower formation energies for all the charge states than the H configuration. This suggests that under equilibrium conditions the T configuration is more energetically favourable in all charge states than the H configuration.

The Er interstitial in Ge forms with formation energies between 0.28 eV and 7.64 eV for all charge states in the T and H configurations. While the formation energy of the H configuration tends to increased from the −2 to the +2 charge state, the formation energies for the T configuration decreased. Charged state controlled metastable defects are important in the study of semiconductor. Charged state controlled metastability suggests that even though two different configurations of the same defect type have the same number and type of atoms, the stability of one configuration over

Table I. Predicted shortest bond distance (Å) between RE and Ge atoms, before geometric relaxation (α_d), after geometric relaxation (β_d), and the difference (Δ_d) between α_d and β_d for the T and H configurations of RE interstitials in Ge

	T			H		
RE–Ge	α_d	β_d	Δ_d	α_d	β_d	Δ_d
Ce–Ge	2.67	2.64	0.03	2.83	2.77	0.06
Pr–Ge	2.31	2.29	0.02	2.77	2.74	0.03
Eu–Ge	2.77	2.71	0.06	2.95	2.87	0.08
Er–Ge	2.67	2.66	0.01	2.70	2.67	0.03

The bond lengths are calculated with respect to the nearest neighbour Ge atoms around the RE.

the other is charge state dependent.[33,34] For the Er interstitial in Ge, the minimum energy configuration of the defect depends on its charge state, suggesting that the defect may display charge state controlled metastability.

The formation energies of both the T and H configurations for the Eu interstitial in Ge show an increasing tendency from the +2 charge state to the −2 charge state. While for both the T and H configurations of the Eu interstitial in Ge the formation energies are between 3.74 eV and 7.82 eV, the T configuration has a lower formation energies than the H configuration. The difference between the formation energy of the T and H configuration for the 0, −1 +1 −2 and +2 charge states is greater than 1.5 eV for all charge state. In addition to the Ce, the Eu and Pr interstitials in Ge are energetically more favourable in the T configuration than the H configuration. For the Pr interstitial in Ge, the T configuration has lower formation energies than the H configuration. Except for the formation energies of the Eu and Er interstitials in Ge which are reasonably high (compared to other RE in this study) for some charge states, the Ce and Pr interstitials in Ge have the lowest formation energies in all the configurations.

The Eu interstitial in Ge has the highest formation energies in both the T and H configuration for charge state −2, −1 , and 0. While the Er interstitial has the highest formation energies for charge state +1 and +2 for the H configuration, the Eu interstitial in Ge forms with the highest formation energy for +1 and +2 charges states for the T configuration. For the T and H configurations of RE interstitials in Ge, in the neutral charge state, the formation energy increases in the sequence Pr < Ce < Er < Eu. One of the possible reasons for such a sequence could be the difference in charge transfer between a RE atom and Ge. While Pr interstitial in Ge has the lowest formation energy for the neutral and negative charge states, the Ce interstitial in Ge has the lowest formation energies for the positive charge states for all configurations. Our calculated formation energies indicate that except for the Er, RE interstitials in Ge under equilibrium conditions are more energetically favourable in the T than the H configuration. This could be as a result of the less strain experience by the RE–Ge atoms bond lengths in the T configuration. Another probable reason why there are differences in formation energies is as a result of the effect of orbital hybridization between a RE atom and its nearest Ge neighbour as seen in the plot of the PDOS.

Charge State Transition Levels of RE Interstitials in Ge

Table IV shows the calculated energies of the charge state thermodynamic transition levels in the band gap of Ge. Plots of the formation energy as a function of the Fermi energy are shown in Fig. 4. For the Ce interstitial in Ge (see Fig. 5a), there is no

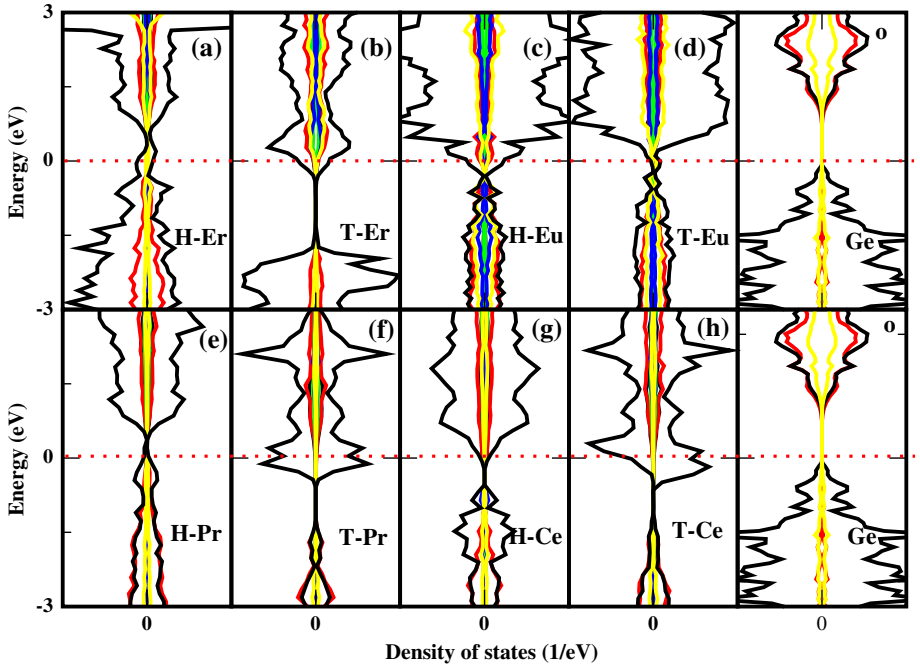

Fig. 3. Plot showing the spin polarised projected density of states (PDOS) of RE interstitials in Ge; (a) H configuration of Er interstitial in Ge (H-Er), (b) T configuration of Er interstitial in Ge (T-Er), (c) H configuration of Eu interstitial in Ge (H-Eu), (d) T configuration of Eu interstitial in Ge (T-Eu), (e) H configuration of Pr interstitial in Ge (H-Pr), (f) T configuration of Pr interstitial in Ge (T-Pr), (g) H configuration of Ce interstitial in Ge (H-Ce), (h) T configuration of Ce interstitial in Ge (T-Ce), and (o) pristine Ge. The Fermi level (at ϵ_f = 0 eV) is shown by the dashed horizontal line. The majority (spin-up) and minority (spin-down) density of states are shown as right and left halves of each plot.

evidence of charge state transition level within the band gap for the T configuration. The +2 charge state is stable for all ε_F in the band gap. For the H configuration of Ce interstitial in Ge, we found a transition level at $(+2/+1)$, which is a shallow donor lying close to the conduction band minimum (CBM) at $E_C - 0.03$ eV (E_C is the energy of the conduction band minimum). This suggests that the energetic distance to the band edge is within a few k_BT at room temperature, resulting in efficient ionization of electrons from the defect level into the conduction band (leading to mobile electrons).

For the Pr interstitial in Ge, there is no evidence of charge state transition level found within the band gap for both the T and H configurations. For the H configuration of Pr interstitial in Ge, the −1 charge state is stable for all ε_F in the band gap. For the T configuration of the Pr interstitial in Ge, the neutral charge state is stable for all ε_F in the band gap as shown in Fig. 5b. According to Fig. 5c, for the Eu interstitial in Ge, the H configuration is predicted to induce deep and shallow levels within the band gap. These levels are deep at $E_V + 0.26$ and $E_C - 0.26$ eV for the double donor (+2/+1) and (+1/0), respectively, and reasonably shallow lying close to the CBM at $E_C - 0.14$ eV for the single acceptor (0/−1). Other levels found in this configuration are not thermodynamically accessible. For the T configuration of the Eu interstitial in Ge, while there is neither a donor nor acceptor level found, we found an interesting charge state transition level at (+2/−2), which lies deep in the band gap at $E_V + 0.18$ eV. The interaction energy between two electrons in a two-level defect is referred to as Hubbard U.[23,35] A defect often has a *negative-U* ($U < 0$) if the atomic position of the defect depends sensitively on its charge state. The Eu interstitial in Ge displays *negative-U* ordering at (+2/−2), i.e charged states +1, 0, and −1 are unstable with respect to dissociating into $q = +2$ and $q = -2$. We calculated the effective *negative-U* of the Eu interstitial in Ge for the T configuration to be −1.50 eV.

Figure 5d indicates the presence of a deep level created by Er interstitial in Ge, for both the T and H configurations. For the T configuration, the Er interstitial induces a transition state at (+2/+1) which is a deep donor level lying at $E_C - 0.28$ eV. For the H configuration, instead of observing a

Table II. Calculated total charge (Coulomb) transfer between a RE and Ge atoms, for the T configuration of RE interstitials in Ge

Defect	Pr	Ce	Er	Eu
Charge transfer	1.04	1.05	1.21	1.42

Table III. Calculated formation energies (E^f) in eV at $\epsilon_f = 0$ of the Ce, Eu Er, and Pr, interstitials in Ge

Defect	Configuration	−2	−1	0	+1	+2
Ce	T	**−0.34**	**−1.62**	**−2.74**	**−3.69**	**−4.45**
	H	2.61	0.99	0.04	−0.87	−1.55
Er	T	3.83	2.65	**1.61**	**0.78**	**0.28**
	H	**2.06**	**1.40**	4.51	7.64	7.21
Eu	T	**4.49**	**5.30**	**4.61**	**4.03**	**3.74**
	H	7.82	6.80	6.17	5.64	5.39
Pr	T	**−2.61**	**−3.81**	**−4.76**	**−1.60**	**−2.40**
	H	1.35	−0.43	−0.12	1.89	1.24

The configurations with the lowest formation energies for each charge state are written in bold.

Table IV. The energy of the charge state transition levels $\epsilon(q/q')$ in the band gap for the Ce, Eu, Er, and Pr, interstitials in Ge for both the T and H configurations

	T			H		
Charge state transition level	Ce	Er	Eu	Ce	Er	Eu
(+2/+1)	–	0.50	–	0.75	–	0.26
(+1/0)	–	–	–	–	–	0.52
(0/−1)	–	–	–	–	–	0.64
(−1/−2)	–	–	–	–	0.60	–
(+2/−2)	–	–	0.18	–	–	–

These transition levels are taken with reference to the VBM.

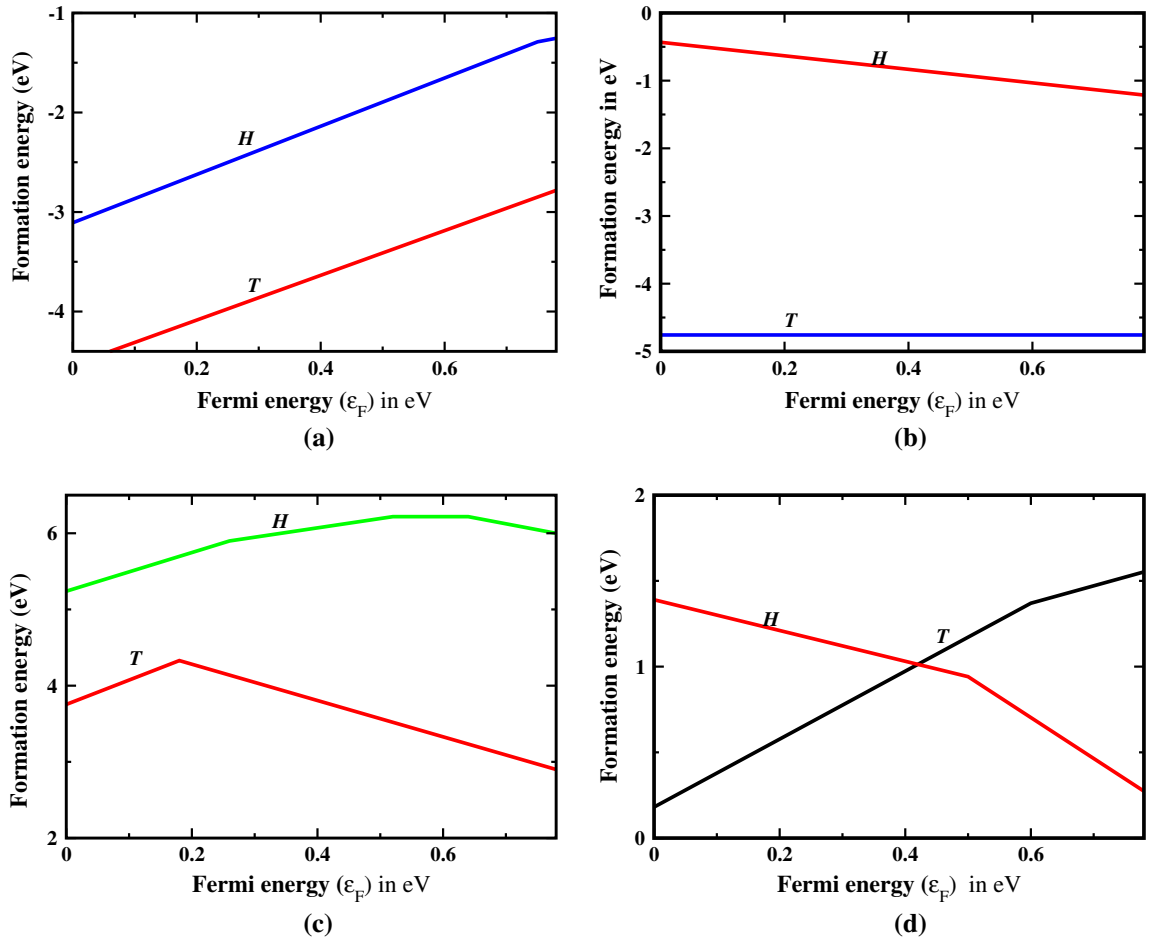

Fig. 4. Plot of formation energy as a function of the Fermi energy for the H (hexagonal) and T (tetrahedral) configurations of RE interstitials in Ge. (a) The H and T configurations of Ce interstitial in Ge, showing donor level for the H configuration. (b) The H and T configurations of the Pr interstitial in Ge, there is no charge state transition level induced by this defect. (c) The H and T configurations of Eu interstitial in Ge, showing negative-U properties for the T configuration. (d) The H and T configurations of Er interstitial in Ge. The Er interstitial in Ge displays the properties of charge state controlled metastability.

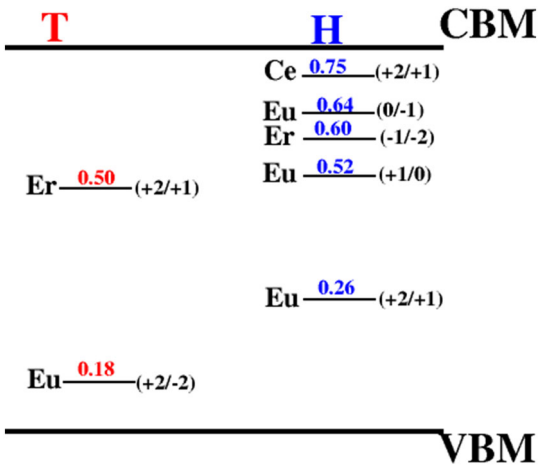

Fig. 5. Calculated *negative-U*, acceptor, and donor transition energy levels for both the tetrahedral (T) and hexagonal (H) configurations of RE interstitials in Ge. All energy levels (eV) are with respect to the VBM.

donor level, we found a $(-1/-2)$ acceptor level lying far away from the valence band maximum at $E_C - 0.18$ eV. According to Fig. 5, for the T configuration, only the Er and Eu interstitials induce charge state transition levels within the band gap of Ge. For the H configuration of RE interstitials in Ge, all except Pr interstitial induce charge state transition levels within the band gap of Ge.

SUMMARY

In conclusion, results of the tetrahedral (T) and the hexagonal (H) configurations of the Ce, Pr, Eu, and Er interstitials in Ge are presented. For all calculations, the Heyd, Scuseria, and Ernzerhof (HSE06) hybrid functional was used in the framework of density functional theory (DFT). The formation energies and charge state transition levels for Re interstitials in Ge are described in detail. We have shown that the formation of Ce, Pr, Eu, and Er interstitials in Ge

exist with formation energies between −4.76 eV and 7.82 eV for all charge states, with that of Eu and Er interstitials in Ge slightly higher for some charge states. Our calculations show that of all the four elements, the Ce and Pr interstitials in Ge, have the lowest formation energies in both the T and H configurations. For the Ce, Pr, and Eu interstitials in Ge, the formation energies for the T configuration are lower than the H configurations in all charge states. The Er interstitial in Ge exhibits properties of charge state controlled metastability.

We have shown that unlike the Pr interstitial in Ge, that has no induced accessible transition level within the band gap, the Er and Eu interstitials in Ge induce charge state transition levels in the band gap. While the H configuration of Eu interstitial induces double and single donor levels at $E_V + 0.26$ eV and $E_C - 0.26$ eV respectively, the T configuration of the Eu interstitial in Ge displays *negative-U* ordering at (+2/−2) transition level. The Er interstitial in Ge induces a donor level in the T configuration and an acceptor level in the H configuration at $E_C - 0.28$ eV and $E_C - 0.18$ eV respectively.

ACKNOWLEDGEMENTS

This work is based on the research supported partly by National Research foundation (NRF) of South Africa [Grant Specific Unique Reference Number (UID) 98961]. The opinions, findings and conclusion expressed are those of the authors and the NRF accepts no liability whatsoever in this regard.

REFERENCES

1. S. Hernández, R. Cuscó, L. Artús, E. Nogales, R. Martin, K. ODonnell, G. Halambalakis, O. Briot, K. Lorenz, and E. Alves, *Opt. Mater.* 28, 771 (2006).
2. E. Igumbor and W. Meyer, *Mater. Sci. Semicond. Process.* 43, 129 (2016).
3. A. Colder, P. Marie, T. Wojtowicz, P. Ruterana, S. Eimer, L. Méchin, K. Lorenz, U. Wahl, E. Alves, and V. Matias et al., *Superlattices Microstruct.* 36, 713 (2004).
4. C.W. Lee, H.O. Everitt, D. Lee, A. Steckl, and J. Zavada, *J. Appl. Phys.* 95, 7717 (2004).
5. R. Jones, *Opt. Mater.* 28, 718 (2006).
6. C. Claeys and E. Simoen, *Germanium-Based Technologies: From Materials to Devices*, 2nd ed. (Netherlands: Elsevier, 2011).
7. E. Igumbor, C. Ouma, G. Webb, and W. Meyer, *Phys. B Condens. Matter* 480, 191 (2016).
8. E. Igumbor, R.E. Mapasha, R. Andrew, and W.E. Meyer, *Comput. Condens. Matter* 8, 31 (2016).
9. P. Deák, B. Aradi, T. Frauenheim, E. Janzén, and A. Gali, *Phys. Rev. B* 81, 153203 (2010).
10. F.J. Morin and J.P. Maita, *Phys. Rev.* 94, 1525 (1954).
11. L. Lee, E.A. Fitzgerald, M.T. Bulsara, T. Currie, and A. Lochtefeld. *J. Appl. Phys.* 97, 011101 (2005).
12. P. Śpiewak, J. Vanhellemont, K. Sueoka, K. Kurzydłowski, and I. Romandic, *Mater. Sci. Semicond. Process.* 11, 328 (2008).
13. S. Coelho, F. Auret, P.J. van Rensburg, and J. Nel, *Phys. B Condens. Matter* 439, 97 (2014).
14. G.S. Pomrenke, E. Silkowski, J.E. Colon, D.J. Topp, Y.K. Yeo, and R.L. Hengehold, *J. Appl. Phys.* 71, 1919 (1992).
15. Y. Miyata, Y. Nose, T. Yoshimura, A. Ashida, and N. Fujimura, *J. Cryst. Growth* 425, 158 (2015).
16. H. Przybylinska, W. Jantsch, Y. Suprun-Belevitch, M. Stepikhova, L. Palmetshofer, G. Hendorfer, A. Kozanecki, R.J. Wilson, and B.J. Sealy, *Phys. Rev. B* 54, 2532 (1996).
17. J. Heyd, G.E. Scuseria, and M. Ernzerhof, *J. Chem. Phys.* 118, 8207 (2003).
18. G. Kresse and J. Furthmüller, *Phys. Rev. B* 54, 11169 (1996).
19. G. Kresse and D. Joubert, *Phys. Rev. B* 59, 1758 (1999).
20. P.E. Blochl, *Phys. Rev. B* 50, 17953 (1994).
21. J.P. Perdew, K. Burke, and M. Ernzerhof, *Phys. Rev. Lett.* 77, 3865 (1996).
22. H. Tahini, A. Chroneos, R.W. Grimes, U. Schwingenschlgl, and H. Bracht, *Appl. Phys. Lett.* 99, 072112 (2011).
23. E. Igumbor, K. Obodo, and W.E. Meyer, *Solid State Phenom.* 242, 440 (2015).
24. B.G. Janesko, T.M. Henderson, and G.E. Scuseria, *Phys. Chem. Chem. Phys.* 11, 443 (2009).
25. V.I. Anisimov, J. Zaanen, and O.K. Andersen, *Phys. Rev. B* 44, 943 (1991).
26. L. Petit, A. Svane, Z. Szotek, and W.M. Temmerman, *Phys. Rev. B* 72, 205118 (2005).
27. M. Cococcioni and S. De Gironcoli, *Phys. Rev. B* 71, 035105 (2005).
28. J.L. Da Silva, M.V. Ganduglia-Pirovano, J. Sauer, V. Bayer, and G. Kresse, *Phys. Rev. B* 75, 045121 (2007).
29. H.J. Monkhorst and J.D. Pack, *Phys. Rev. B* 13, 5188 (1976).
30. S.B. Zhang and J.E. Northrup, *Phys. Rev. Lett.* 67, 2339 (1991).
31. Y. Kumagai and F. Oba, *Phys. Rev. B* 89, 195205 (2014).
32. C. Freysoldt, J. Neugebauer, and C.G. Van de Walle, *Phys. Status Solidi (b)* 248, 1067 (2011).
33. M. Risse and R. Vianden, *J. Appl. Phys.* 93, 2648 (2003).
34. J. Dkabrowski and M. Scheffler, *Mater. Sci. Forum* 83, 735 (1992).
35. C. Freysoldt, B. Grabowski, T. Hickel, J. Neugebauer, G. Kresse, A. Janotti, and C.G. Van de Walle, *Rev. Mod. Phys* 86, 253 (2014).

5.7.4 Article 4

A first principle hybrid functional calculation of Tm_{Ge}^{3+} -V_{Ge} defect complexes in germanium

E. Igumbor, R. E. Mapasha, Richard Andrew and W. E. Meyer

Computational Condensed Matter 8, (2016), 31−35

http://dx.doi.org/10.1016/j.cocom.2016.07.003

Computational Condensed Matter 8 (2016) 31–35

Contents lists available at ScienceDirect

Computational Condensed Matter

journal homepage: http://ees.elsevier.com/cocom/default.asp

A first principle hybrid functional calculation of Tm_{Ge}^{3+}-V_{Ge} defect complexes in germanium

E. Igumbor [a, b, *], R.E. Mapasha [a], Richard Andrew [a], W.E. Meyer [a, **]

[a] Department of Physics, University of Pretoria, Pretoria 0002, South Africa
[b] Department of Mathematics and Physical Sciences, Samuel Adegboyega University, Km 1 Ogwa/Ehor Rd, Ogwa, Edo State, Nigeria

ARTICLE INFO

Article history:
Received 12 January 2016
Received in revised form
12 July 2016
Accepted 14 July 2016
Available online 19 July 2016

Keywords:
Defects
Charge state
Formation energy
Rare earth

ABSTRACT

By means of density functional theory (DFT), using the screened Heyd, Scuseria, and Ernzerhof (HSE06) hybrid functional we present results of the Tm_{Ge}^{3+}-V_{Ge} defect complexes in germanium (Ge). The formation energies of the first (*fnn*), second (*snn*), third (*tnn*) and fourth ($f_t nn$) nearest neighbour configurations of V_{Ge}-V_{Ge} were examined. The charge state transition levels for all these configurations were examined as well. The Tm_{Ge}^{3+}-V_{Ge} complexes were found to have a positive binding energies for the neutral charge state in the *fnn* and $f_t nn$ configurations. The thermodynamic transition levels revealed that the Tm_{Ge}^{3+}-V_{Ge} induced shallow levels in the band gap for the *fnn*, *tnn* and $f_t nn$ configurations and deep level for the *tnn* configuration. The *snn* configuration showed no charge state transition level, the − 2 charge state was stable for all Fermi energies in the band gap. The Tm_{Ge}^{3+}-V_{Ge} displayed evidence of a single donor level (+1/0) and an acceptor level (−1/−2) within the band gap. Charge state controlled metastability was exhibited by the Tm_{Ge}^{3+}-V_{Ge}.

1. Introduction

Study of defects in semiconductor materials have been intensively carried out in the last two decades, most especially for materials such as Si and Ge [1]. While the former has a band gap of 1.11 eV [2], the latter has a narrow band gap of 0.78 eV [3] at 0 K. The high electron and hole mobilities of Ge has made it possible for strained Si_{1-x} Ge_x heterostructures to increase mobility in modern transistors [4]. Impurities influence Ge-based semiconductor devices either positively or negatively [1]. The formation energy and the transition charge state levels created in the band gap are important parameters that determine the effect of defect in a semiconductor [5]. Several experimental and theoretical studies of point defects such as vacancies and diffusion [6–9], interstitials [1,10] and impurity substitution [11,12] in Ge had been investigated using different techniques and approaches. The rare earth (RE) are good examples of elements that have amongst other orbitals, the *4f* orbital at the valence shell, which are highly localized [13,14]. The RE are mainly use to generate optical sources over extensive wavelength range from the visible to the infrared regions [15,16]. The optical properties of RE give a proper description of the photoluminescence experience in a RE related defect in Si [15]. Recently fabrication and optical properties of Tm doped materials were studied and electro-luminescence (EL) has been demonstrated from this material [17–19]. Light emission devices have been attributed to thulium and erbium defects in several materials [20,21]. For Ge, Tm^{3+} defects were extensively studied using a screened hybrid functional [11]. According to *Ref* [11], the Tm^{3+} interstitial and substitutional defects in Ge exist with low formation energies and Tm^{3+} defect introduced transition levels of (0/−1), (+1/0) and (+1/+2) within the band gap [11]. Vacancy impurity complexes in Ge are important because many substitutional centres including dopant migrate by thermally generated vacancies [22]. The results of the RE defect related complexes in GaN [23–25], AlN/Si [26] and GaAs [27] has been previously studied and reported. It have been predicted that the RE defect complexes in GaN exhibit charge state controlled metastability [23]. While for Si, the RE impurities are electrically inert and induced gap levels occupied by the valence electrons [26], but for AlN, the RE impurities induced deep levels within the band gap [28]. For the GaN, AlN, GaAs and Si, the structural and electronic properties of the RE induced defects has been successfully predicted. However, the structural and

* Corresponding author. Department of Physics, University of Pretoria, Pretoria 0002, South Africa.
** Corresponding author.
E-mail addresses: elgumuk@gmail.com (E. Igumbor), wmeyer@up.ac.za (W.E. Meyer).

http://dx.doi.org/10.1016/j.cocom.2016.07.003

electronic properties of RE induced defect complexes in Ge have not been reported both experimentally and theoretically. In this work, we have used the screened hybrid functional of Heyd, Scuseria, and Ernzerhof (HSE06) [29] by means of density functional theory (DFT) to calculate the structural and electronic properties of the Tm^{3+}-V_{Ge} defect complexes in Ge for the nearest neighbour (*fnn*), second nearest neighbour (*snn*), third nearest neighbour (*tnn*) and fourth nearest neighbour ($f_t nn$) configurations. The energies of formation for the various configurations were calculated for charge states $(-2, -1, 0, +1, and +2)$. The charge states transition levels for the Tm^{3+}-V_{Ge} were examined and presented. The role of shallow levels and charge state controlled metastability along side with *negative-U* behaviour were also discussed. The remaining parts of this paper have been organised as follows: in Section 2, we present a description of the computational details, followed by the results and discussion in Section 3 and finally, we present our concluding remarks in Section 4.

2. Computational details

Using the Vienna *ab-initio* Simulation Package (VASP) [30,31], we have carried out DFT calculation of the Tm^{3+}-V_{Ge}. The inert core electrons were separated from the chemically active valence electrons by using the Projector-augmented wave (PAW) method, as implemented in the VASP code [30,32]. For Ge, the 4*s* and 4*p* electrons in the outer shell were treated as valence electrons, while for Tm^{3+}, the 6*s*, 5*p* and 4*f* orbitals were considered as valence electrons. DFT calculations were carried out using the HSE06 hybrid functional [29,33]. In this approach, the short-range exchange potential was calculated by mixing a fraction (25%) of nonlocal Hartree-Fock exchange with the generalized gradient approximation (GGA) functional of Perdew, Burke, and Ernzerhof (PBE) [34]. In contrast to the local density approximation and the generalized gradient approximation that underestimate the band gap of the semiconductor [35,36], the HSE06 functional gives an excellent description of the electronic band gap for a wide range of defects in group-IV semiconductors [37,10]. For the past decades, the study and prediction of the electronic properties of materials with the *4f* orbital valence electron was difficult due to the fact that the *f* orbital is highly localised. The highly localised *4f* orbital was previously treated using LDA + U and other methods [13,38–40]. Recently, the hybrid density functional has been successfully used to predict the electronic properties of several materials with highly localized *f* orbitals in the valence shell [13,14]. Following this success of the hybrid density functional, it became feasible to handle the *4f* orbital in the valence shell of Tm^{3+}. For the bulk, geometric optimization of Ge was performed in an 8-atom unit cell with an 8^3 Monkhorst-Pack [41] k-point Brillouin zone sampling scheme and cutoff energy of 400 eV. For the defects, we employed a 64 atom supercell using a 2^3 Monkhorst-Pack [41] k-point Brillouin zone sampling scheme, and we set the plane wave cutoff of the wave function expansion to 400 eV. We refined the structure until the change in the total energy was less than 10^{-5} eV and the forces were relaxed to below 0.001 eV/Å. In all the calculations, spin orbit coupling was taken into account To calculate the defect formation and transition energy $(\varepsilon(q/q'))$ levels, we calculated the total energy $E(d, q)$ for a supercell containing the optimized defect *d* in its charge state *q*. The defect formation energy $E^f(d, q)$ as a function of electron Fermi energy (ε_F) relative to the valence band edge is given as [42,43].

$$E^f(d,q) = E(d,q) - E(pure) + \sum_i (\Delta n)_i \mu_i + q[E_V + \varepsilon_F] + E^q_{cor}, \tag{1}$$

where $E(pure)$ is the energy of a supercell without a defect, $(\Delta n)_i$ is the difference in the number of constituent atoms of type *i* between the pristine and the supercell containing the defect, μ_i represents the chemical potential of different constituent atoms and E_V is the valence band maximum (VBM). Errors in $E^f(d, q)$ due to finite-size effects within the supercell and inaccuracy underlying the approximation of the energies, were handled by including the correction E^q_{cor} term according to FNV [43,44]. The defect transition energy level $\varepsilon(q/q')$ is the Fermi energy at which two charge states (q and q') of the defect have the same energy of formation is given as [5].

$$\varepsilon(q/q') = \frac{E^f(d,q;\varepsilon_F = 0) - E^f(d,q';\varepsilon_F = 0)}{q' - q} \tag{2}$$

As reported in Ref. [10], we took the modelled band gap of the pristine Ge at 0 K to be 0.78 eV. The binding energies E_b which are defined as the energy required to split up defect cluster into well separated non-interacting defects is given as [45].

$$E_b = E^f_{V_{Ge}} + E^f_{Tm^{3+}_{Ge}} - E^f_{defect-complex}, \tag{3}$$

where $E^f_{V_{Ge}}$, $E^f_{Tm^{3+}_{Ge}}$ and $E^f_{defect-complex}$ are the formation energies of V_{Ge}, Tm^{3+}_{Ge} and Tm^{3+}-V_{Ge} respectively. Eq. (3) could be interpreted as the energy loss of the bonded structure with respect to the isolated components.

3. Results and discussion

3.1. Structural properties of Tm^{3+}-V_{Ge}

The geometric structures of Tm^{3+}-V_{Ge} for four configurations are shown in Fig. 1. Fig. 1a and b show the relaxed geometric structure of the first nearest neighbour (*fnn*) and second nearest neighbour (*snn*), respectively. While Fig. 1c shows the relaxed geometric structure of the third nearest neighbour (*tnn*), Fig. 1d displays the relaxed geometric structure of the fourth nearest neighbour ($f_t nn$). Fig. 1e is the extract of the Tm atom with its four nearest neighbour Ge atoms. For the *fnn* configuration, the Tm-Ge bond length decreased by 0.01 Å. Whereas two bond angles formed decreased by 1° and the other two bond angles were unchanged. For the *snn* configuration, we observed that the Tm-Ge bond length decreased by 0.5 and 0.10 Å except for in one direction, where the bond length increased by 0.40 Å. For the bond angle in *snn* configuration, while two bond angles decreased by 8° and 10°, the other 2 bond angles increased by 7° and 10°. For the *tnn* configuration, all the optimised bond length increased by an average of 0.40 Å and half of the bond angles formed increased by 7° and 1°, while the other half decreased by 8° and 2°. Finally for the $f_t nn$ configuration, all the bond length increased by an average of 0.28 Å. The bond angles formed increased by 2° and 9° except for in one, which decreased by 8°.

3.2. Formation energies and thermodynamic properties of Tm^{3+}-V_{Ge}

Results of the formation energies of Tm^{3+}-V_{Ge} in its various configurations are tabulated in Table 1. In all the configurations, the defect Tm^{3+}-V_{Ge} forms with formation energies between 4.00 and 7.50 eV. Under equilibrium conditions, the *fnn* configuration is energetically more favourable in all charge states except for the − charge state where the $f_t nn$ is energetically most favourable. The Tm^{3+}-V_{Ge} had a lower formation energy in the *tnn* configuration than the *snn* configuration. In the neutral state, the energy difference between the *fnn* and the *snn* is 2.01 eV. By using Eq. (3), we

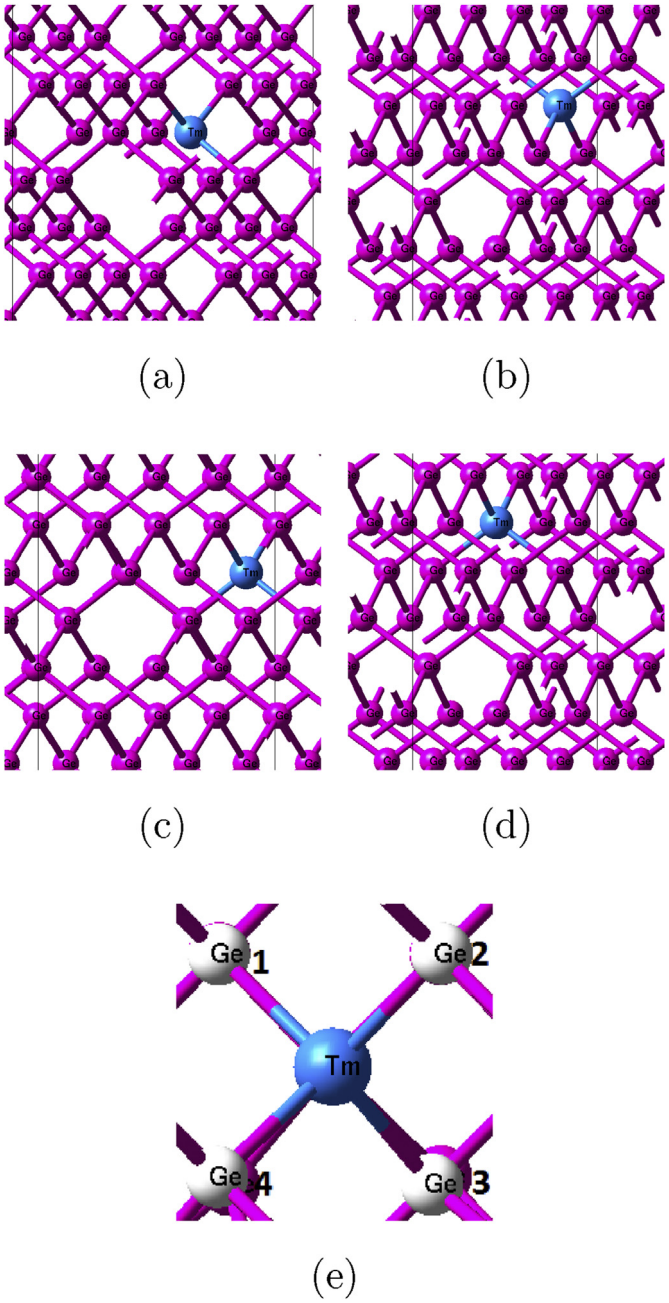

Fig. 1. Geometric structure of the Tm^{3+}_{Ge}-V_{Ge} complex in Ge for the (a) first nearest neighbour, (b) second nearest neighbour, (c) third nearest neighbour, (d) fourth nearest neighbour and (e) extract of the Tm and its nearest neighbour Ge atoms.

Table 1
Calculated formation energies (E^f) in eV at $\varepsilon_f = 0$ of Tm^{3+}_{Ge}-V_{Ge} complexes in Ge for the first nearest neighbour (*fnn*), second nearest neighbour (*snn*), third (*tnn*) nearest neighbours and the fourth (f_t *nn*) configurations. The lowest formation energy in each charge state are written in bold.

Defect	Configuration	−2	−1	0	+1	+2
Tm^{3+}_{Ge}–V_{Ge}	*fnn*	**4.78**	4.72	**5.06**	**4.88**	**5.17**
	snn	6.54	8.79	7.07	7.30	7.64
	tnn	6.01	5.60	5.17	5.12	5.55
	f_t *nn*	4.88	**4.67**	5.07	5.69	5.90

calculated the binding energies for the Tm^{3+}-V_{Ge} in the neutral state to be 0.06, −0.05, − 1.95 and 0.05 eV for the *fnn*, *snn*, *tnn* and the f_t*nn* configurations, respectively. The binding energies suggest that the *fnn* and f_t*nn* configurations can form without dissociating.

Table 2
The energy of the charge state transition levels $\varepsilon(q/q')$ above E_V (eV) for the *fnn*, *tnn* and f_t *nn* configurations of Tm^{3+}_{Ge}-V_{Ge} complexes.

Charge states	*fnn*	*tnn*	f_t *nn*
(+1/0)	–	0.05	–
(0/−2)	–	0.41	–
(−1/−2)	0.06	–	0.21

The plot of the charge state transition levels for the *fnn*, *snn*, *tnn* and f_t*nn* configurations of Tm^{3+}-V_{Ge} are presented in Fig. 2. Fig. 2a and d show the plot of the formation energies of Tm^{3+}-V_{Ge} in its charge states as a function of ε_F for the *fnn*, *snn*, *tnn* and f_t*nn* configurations respectively. Fig. 2e represents the thermodynamically most stable accessible region for the *fnn*, *snn tnn* and f_t*nn* configurations. Table 2 lists the energy of the charge state transition levels. For the *fnn* configuration, the Tm^{3+}-V_{Ge} induced a double shallow acceptor level at E_V + 0.06 eV close to the valence band maximum (VBM). There was no other thermodynamically accessible induced level found for the *fnn* configurations. For the *snn* configurations, there was no transition level induced by Tm^{3+}-V_{Ge} within the band gap. The −2 charge state has the lowest energy level across the band gap. This is in contrast to the *tnn* configuration where we observed the presence of two levels within the band gap. These levels are single donor, located at E_V + 0.05 eV and an acceptor deep level at E_V + 0.41 eV. All other possible transition levels are at almost 1 eV away from the stable region within the band gap. For the f_t*nn* configuration, we observed a single Tm^{3+}-V_{Ge} induced level. Quite interestingly, the level is a shallow acceptor at E_V + 0.16 eV close to the VBM. For all the observed induced levels within the band gap, we discovered that the Tm^{3+}-V_{Ge} is most likely to form acceptor levels than donor levels and most of these levels are close to the VBM.

The Tm^{3+}-V_{Ge} induced defect in Ge reveals interesting properties, such as the charge state controlled metastability and the *negative-U* properties. In Fig. 2e, for the *fnn* and f_t*nn* configurations we noticed the evidence of charged state controlled metastability. The implication of the presence of charge state controlled metastability is that the minimum energy configuration of the Tm^{3+}-V_{Ge} can be controlled by changing the charged state of the defect from −1 to −2. The difference in energy between the *fnn* and f_t*nn* configurations for charge state −1 and −2 is small (0.05 and 0.1 eV respectively). This difference is in order of K_B T at room temperature, so both states should be occupied at room temperature. Taking the high energy of formation of the *snn* and *tnn* configurations, it seems there is a large energy barrier between the two states. In addition, the low binding energy of the defect makes it unlikely for vacancies to be captured for long. It is therefore doubtful if there will be enough opportunity for a significant number of vacancies in the f_t*nn* configuration to surmount the barrier in order for the defect to transform to its *fnn* states. While there was no evidence of *negative-U* behaviour for the *fnn* and f_t*nn* configurations, in the *tnn* configurations, the Tm^{3+}-V_{Ge} exhibited the properties of *negative-U* with *effective-U* value of −0.42 eV. The Tm^{3+}-V_{Ge} complexes enhance the efficient ionization of electrons from the valence band which in turn create holes in the valence band. The Tm^{3+} defects in Ge should be used to control conductivity since it exhibit the properties of shallow levels.

4. Conclusion

In conclusion, the density function theory (DFT) with the screened Heyd, Scuseria, and Ernzerhof (HSE06) hybrid function

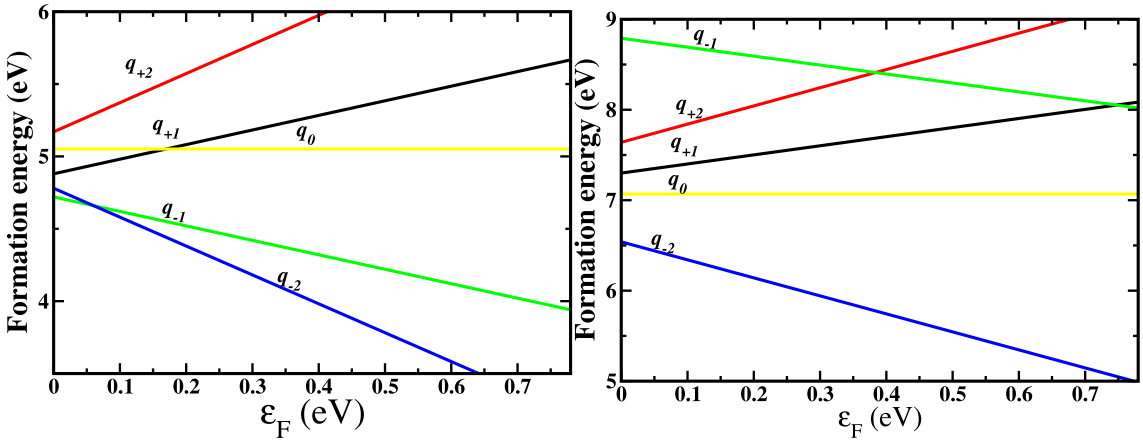

(a) First nearest neighbour (*fnn*). (b) Second nearest neighbour (*snn*).

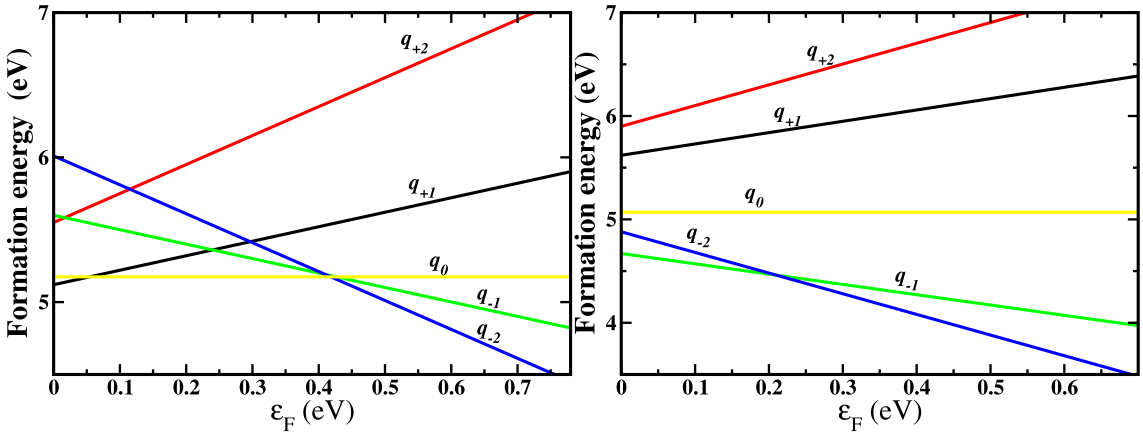

(c) Third nearest neighbour (*tnn*). (d) Fourth nearest neighbour ($f_t nn$).

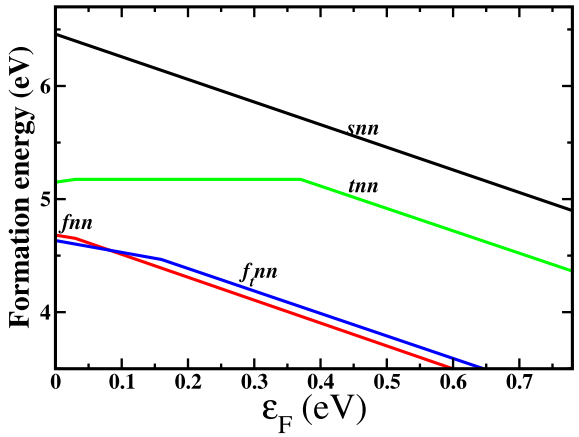

(e) Thermodynamically stable region for various configurations.

Fig. 2. Plot of formation energy as a function of the Fermi energy of the Tm^{3+}_{Ge}-V_{Ge} complexes in Ge for the *fnn*, *snn*, *tnn* and *ft nn* configurations. Fig. 2e shows the most thermodynamically stable region within the band gap for the various configurations being examined. The *fnn* and f_t*nn* configurations displayed the properties of charged state controlled metastability and the *tnn* displays *negative-U* properties.

were used to calculate the Tm^{3+}-V_{Ge} in its four different configurations (first nearest neighbour (*fnn*) second nearest neighbour (*snn*), third nearest neighbour (*tnn*) and the fourth nearest neighbour (f_t*nn*). The structural properties, electronic properties, formation energies and charge state thermodynamic transition levels were calculated and described. We have shown that the

formation of the Tm^{3+}-V_{Ge} occurred in four different configuration with low formation energy except for the *snn* configuration which had a high formation energy. The *fnn* and $f_t nn$ configurations of the Tm^{3+}-V_{Ge} defect under equilibrium condition were energetically most favourable. For the neutral state the *fnn* and $f_t nn$ forms with 5.06 and 5.07 eV formation energies and with a positive binding energy of 0.06 and 0.05 eV respectively. The charge state transition levels shown that the Tm^{3+}-V_{Ge} induced shallow levels close to the valence band maximum. These shallow levels are acceptor at $\varepsilon(-1/-2) = 0.06$ eV and $\varepsilon(-1/-2) = 0.21$ eV for the *fnn* and $f_t nn$ configurations respectively and donor at $\varepsilon(+1/0) = 0.05$ eV for the *tnn* configuration. In addition, Tm^{3+}-V_{Ge} displayed the properties of charge state controlled metastability between the *fnn* and the $f_t nn$ configurations. We have pointed out the role of vacancy complexes in Ge and we expect the data and information presented to be useful in the process modelling of Ge-based devices for industrial applications.

Acknowledgement

This work is based on the research supported partly by National Research foundation (NRF) of South Africa (Grant specific unique reference number (UID) 78838). The opinions, findings and conclusion expressed are those of the authors and the NRF accepts no liability whatsoever in this regard.

References

[1] C. Claeys, E. Simoen, Germanium-based Technologies: from Materials to Devices, Elsevier, 2011.
[2] O. Madelung, Semiconductors Basic Data, Springer Science & Business Media, 2012.
[3] F.J. Morin, J.P. Maita, Phys. Rev. 94 (1954) 1525–1529.
[4] L. Lee, E.A. Fitzgerald, T. Bulsara, Mayank T. Currie, A. Lochtefeld, J. Appl. Phys. 97 (1) (2005) 011101.
[5] Christoph Freysoldt, Blazej Grabowski, Tilmann Hickel, J. Neugebauer, Georg Kresse, Anderson Janotti, C.G.V. de Walle, Rev. Mod. Phys. 86 (2014) 253–305.
[6] S. Coelho, F. Auret, P.J. van Rensburg, J. Nel, Phys. B Condens. Matter 439 (0) (2014) 97–100.
[7] R. Kube, H. Bracht, A. Chroneos, M. Posselt, B. Schmidt, J. Appl. Phys. 106 (6) (2009) 063534.
[8] A. Chroneos, H. Bracht, Diffusion of n-type dopants in germanium, Appl. Phys. Rev. 1 (1) (2014) 011301.
[9] H. Tahini, A. Chroneos, R. Grimes, U. Schwingenschlögl, Appl. Phys. Lett. 99 (16) (2011) 162103.
[10] E. Igumbor, C.N.M. Ouma, G. Webb, W.E. Meyer, Phys. B Condens. Matter 480 (2016) 191–195.
[11] E. Igumbor, W.E. Meyer, Mater. Sci. Semicond. Process. 43 (2016) 129–133.
[12] J. Lauwaert, S. Segers, F. Moens, K. Opsomer, P. Clauws, F. Callens, E. Simoen, H. Vrielinck, J. Phys. D Appl. Phys. 48 (17) (2015) 175101.
[13] B.G. Janesko, T.M. Henderson, G.E. Scuseria, Phys. Chem. Chem. Phys. 11 (3) (2009) 443–454.
[14] J.L. Da Silva, M.V. Ganduglia-Pirovano, J. Sauer, V. Bayer, G. Kresse, Phys. Rev. B 75 (4) (2007) 045121.
[15] J.H. Castilho, I. Chambouleyron, F.C. Marques, C. Rettori, F. Alvarez, Phys. Rev. B 43 (11) (1991) 8946.
[16] A.G. Raffa, P. Ballone, Phys. Rev. B 65 (12) (2002) 121309.
[17] F. Fang, A. Ng, X. Chen, A. Djurii, Y. Zhong, K. Wong, P. Fong, H. Lui, C. Surya, W. Chan, Mater. Chem. Phys. 125 (3) (2011) 813–817.
[18] M. Peres, J. Wang, M. Soares, A. Neves, T. Monteiro, E. Rita, U. Wahl, J. Correia, E. Alves, Superlattices Microstruct. 36 (46) (2004) 747–753.
[19] T. Monteiro, A. Neves, M. Soares, M. Carmo, M. Peres, E. Alves, E. Rita, Appl. Phys. Lett. 87 (19) (2005) 192108.
[20] M. Lourenço, C. Opoku, R. Gwilliam, K. Homewood, Opt. Mater. 32 (12) (2010) 1597–1600.
[21] A. Polman, J. Appl. Phys. 82 (1) (1997) 1–39.
[22] J. Coutinho, S. Öberg, V.J.B. Torres, M. Barroso, R. Jones, P.R. Briddon, Phys. Rev. B 73 (2006) 235213.
[23] C.N. Ouma, W.E. Meyer, Phys. B Condens. Matter 439 (2014) 141–143.
[24] S. Sanna, W. Schmidt, T. Frauenheim, U. Gerstmann, Phys. Rev. B 80 (10) (2009) 104120.
[25] J.-S. Filhol, R. Jones, M. Shaw, P. Briddon, Appl. Phys. Lett. 84 (15) (2004) 2841–2843.
[26] R. Jones, Opt. Mater. 28 (6) (2006) 718–722.
[27] A. Svane, N.E. Christensen, L. Petit, Z. Szotek, W. Temmerman, Phys. Rev. B 74 (16) (2006) 165204.
[28] S. Wang, X. Wang, J. Li, Y. Jia, F. Wang, Mod. Phys. Lett. B 29 (21) (2015) 1550114.
[29] J. Heyd, G.E. Scuseria, M. Ernzerhof, J. Chem. Phys. 118 (18) (2003) 8207–8215.
[30] G. Kresse, J. Furthmüller, Phys. Rev. B 54 (1996) 11169–11186.
[31] G. Kresse, D. Joubert, Phys. Rev. B 59 (1999) 1758–1775.
[32] P.E. Blochl, Phys. Rev. B 50 (1994) 17953–17979.
[33] J. Heyd, G.E. Scuseria, J. Chem. Phys. 120 (16) (2004) 7274–7280.
[34] J.P. Perdew, K. Burke, M. Ernzerhof, Phys. Rev. Lett. 77 (1996) 3865–3868.
[35] H. Tahini, A. Chroneos, R. Grimes, U. Schwingenschlögl, H. Bracht, Appl. Phys. Lett. 99 (7) (2011) 072112.
[36] P. Śpiewak, J. Vanhellemont, K. Sueoka, K. Kurzydłowski, I. Romandic, Mater. Sci. Semicond. Process. 11 (5) (2008) 328–331.
[37] P. Deák, B. Aradi, T. Frauenheim, E. Janzén, A. Gali, Phys. Rev. B 81 (2010) 153203.
[38] V.I. Anisimov, J. Zaanen, O.K. Andersen, Phys. Rev. B 44 (3) (1991) 943.
[39] L. Petit, A. Svane, Z. Szotek, W.M. Temmerman, Phys. Rev. B 72 (20) (2005) 205118.
[40] M. Cococcioni, S. De Gironcoli, Phys. Rev. B 71 (3) (2005) 035105.
[41] H.J. Monkhorst, J.D. Pack, Phys. Rev. B 13 (1976) 5188–5192.
[42] S.B. Zhang, J.E. Northrup, Phys. Rev. Lett. 67 (1991) 2339–2342.
[43] C. Freysoldt, J. Neugebauer, C.G. Van de Walle, Phys. Status Solidi (b) 248 (5) (2011) 1067–1076.
[44] Y. Kumagai, F. Oba, Phys. Rev. B 89 (2014) 195205.
[45] G. Zollo, Y.J. Lee, R.M. Nieminen, J. Phys. Condens. Matter 16 (49) (2004) 8991.

Chapter 6

Conclusion

6.1 Introduction

In this chapter, the conclusion of all reports and results obtained during the process of the research is summarized. This chapter also includes suggested recommendations and future work to be carried out which are related to the topics that are discussed in this thesis.

In this study, *ab initio* density functional theory (DFT) with a hybrid functional has been used to study the structural, electronic and charge state transition properties of point defects in Ge. The hybrid functional of Heyd Scuseria Ernzerhof (HSE06) [15, 63], which is known to overcome most of the shortcomings of standard DFT when using the GGA and LDA exchange correlation functionals, has successfully been used to accurately predict the structural, electronic and charge state transition properties of selected point defects in Ge. The following points summarize the results presented in this thesis.

1. **Validation of the use of the HSE functional**

   The structural and electronic properties of Ge were modelled. The bond length between two nearest neighbours Ge atoms was predicted to be 2.46 Å, which

is in close agreement with experimental and other modelling results reported in literature [107, 177]. The band gap of 0.78 eV at 0 K, as predicted by HSE hybrid functional is in agreement with the experimental band gap as reported by Morin *et al.* [1].

Ge self-interstitial was successfully modelled. The formation energy of the neutral charge state of the Ge self-interstitial in the tetrahedral and split[110] configurations were 3.88 and 3.80 eV, respectively. These results are in close agreement with earlier theoretical reports [89, 98] based on LDA and GGA functional. The Ge self interstitial in the tetrahedral configuration induced a shallow level at E_C −0.04 eV, which is in good agreement with experimental result reported by Haesslein *et al.* [9]

2. **Ge *di*-interstitial ($I_{2(Ge)}$)**

   The formation of $I_{2(Ge)}$ from two neutral isolated interstitials is feasible. The $I_{2(Ge)}$ results show that the tetrahedral (T) configuration, where both interstitials are at a tetrahedral site, is more stable than the split[110]-tetrahedral (SPT) and double split[110] (SP10) configurations by more than 0.8 eV. In the tetrahedral configuration, Ge *di*-interstitials induced a shallow donor (+2/+1) level at E_C − 0.04 eV. In the SP10 configuration, deep levels at E_V + 0.41 eV for (+2/+1) and E_V + 0.47 for (+1/−1) were predicted, while in the SPT configuration only a deep level at E_V + 0.58 eV for (+1/−1) was predicted. The presence of negative-U ordering having effective-U values of −0.61 and −1.6 eV for the SPT and SP10 configurations respectively was observed.

3. **Tm^{3+} related defects in Ge**

   The formation of Tm_i^{3+} (in the hexagonal (H) configuration), Tm_{Ge}^{3+}, and V_{Ge}-Tm_i^{3+} in both (*axial and basal*) configurations were investigated. Of the three configurations investigated, V_{Ge}-Tm_i^{3+} in the *axial* configuration had the lowest

formation energy for all charge states. The Tm_i^{3+}, Tm_{Ge}^{3+}, and V_{Ge}-Tm_i^{3+} defects introduced transition levels of $(0/-1)$ and $(+1/0)$ that lay deep in the band gap of Ge. In addition to these levels, the V_{Ge}-Tm_i^{3+} and Tm_{Ge}^{3+} introduced $(+1/+2)$ and $(-1/-2)$ levels that lay close to the band edges. Unlike the Tm_{Ge}^{3+} and V_{Ge}-Tm_i^{3+} that act as an acceptor $(-1/-2)$, the Tm_i^{3+} does not act as an acceptor, instead, this level lies inside the CBM. These defects have not yet been observed experimentally but the data and information presented should be useful in the process modelling of Ge-based devices.

4. **Rare earth (Ce, Pr, Eu and Er) interstitials in Ge**

   The Ce, Pr, Eu and Er interstitials in Ge were investigated for both the tetrahedral (T) and hexagonal (H) configurations. The formation energy of the Ce, Pr, Eu and Er interstitials in Ge was between -4.76 and 6.17 eV for the neutral charge state. In all charge states, the formation energies of the Ce, Pr, and Eu interstitials in the T configuration were lower than that of the H configuration, while the Er interstitial exhibited charge state controlled metastability. Unlike the Pr interstitial in Ge, which did not have any thermodynamically accessible charge state transition levels, the Er and Eu interstitials in Ge induced charge state transition levels in the band gap. While the H configuration of Eu interstitial in Ge induced donor levels at $E_V + 0.26$ and $E_C - 0.26$ eV, the T configuration of the Eu interstitial in Ge displayed negative-U ordering at $(+2/-2)$. In both the T and H configurations, the Er interstitial in Ge introduced a donor and an acceptor level at $E_C - 0.28$ and $E_C - 0.18$ eV, respectively. The properties of rare earth interstitials in Ge were pointed out and the data and information presented in this thesis should be useful in the process modelling of Ge-based devices for industrial applications.

5. **Tm_{Ge}^{3+} -V_{Ge} defect complexes in germanium**

   The Tm_{Ge}^{3+} -V_{Ge} complex occurred in four configurations (first nearest neighbour (*fnn*), second nearest neighbour (*snn*), third nearest neighbour (*fnn*) and fourth nearest neighbour ($f_t nn$)) with low formation energy except for the *snn* which had a high formation energy. The *fnn* and $f_t nn$ of the Tm^{3+}-V_{Ge} under equilibrium condition were energetically the most favourable configurations. For the neutral state, the *fnn* and $f_t nn$ formed with 5.06 and 5.07 eV formation energies and with positive binding energies of 0.06 and 0.05 eV, respectively. The charge state transition levels showed that the Tm^{3+}-V_{Ge} induced shallow levels are close to the valence band maximum. These shallow levels are acceptors at $\epsilon(-1/-2) = 0.06$ eV and $\epsilon(-1/-2) = 0.21$ eV for the *fnn* and $f_t nn$ configurations, respectively, and donor at $\epsilon(+1/0) = 0.05$ eV for the *tnn* configuration. In addition, the Tm^{3+}-V_{Ge} displays charge state controlled metastability between the *fnn* and $f_t nn$ configurations. The difference in energy between the *fnn* and $f_t nn$ configuration was small (0.05 and 0.1 eV for -1 and -2 charge states, respectively). This difference is in the order of $k_B T$ at room temperature, so both states should be occupied at room temperature. The result presented in this section will be useful in the process modelling of Ge-based devices.

6.2 Future opportunities

The study of defects in Ge, although gaining more ground due to improved experimental techniques, is still in its infancy when one considers how few defects have been identified. Many fruitful attempts have been made comparing theoretical modelled results of properties of point defects in Ge to experimentally observed results. In order to qualitatively compare more properties of points defects in Ge predicted by *ab initio* results, various experimental results need to be fully investigated and studied using *ab*

initio techniques. Before the advent of the HSE functional, *ab initio* predictions of point defect properties in Ge were difficult due to the inadequacy of the various exchange correlation energies (GGA and LDA) applied within DFT to predict the band gap of Ge. The hybrid HSE functional has opened the door to various fundamental point defect studies in Ge, especially vacancy complexes, multiple interstitials and rare earth defects. In addition to the point defects investigated successfully using the HSE functional, there are still more point defects in Ge that need to be investigated. The following future opportunities need to be explored.

1. Electrical and optical activities of the rare earth interstitial and substitutional impurities in Ge need to be fully investigated using a hybrid functional.

2. More studies of vacancy complexes formed in Ge need to be investigated using the hybrid functional.

3. Although *di*-vacancies and *multi*-vacancies have been studied using either LDA or GGA, it is recommended that these defects should be studied using HSE hybrid functional.

4. Optical properties of rare earth interstitial and vacancy-complexes in Ge should be investigated using the HSE hybrid functional.

5. The electrical activities of group II substitutional impurities should be investigated and compared with experimental results.

Bibliography

[1] F. J. Morin and J. P. Maita. Conductivity and hall effect in the intrinsic range of germanium. *Physical Review*, 94(6):1525–1529, 1954. [1, 54, 110]

[2] E. E. Haller. Germanium: From its discovery to SiGe devices. *Materials Science in Semiconductor Processing*, 9:408 – 422, 2006. [1]

[3] C. Claeys and E. Simoen. *Germanium-based technologies: from materials to devices*. Elsevier, 2011. [1, 2, 37, 43, 44, 53, 55, 78]

[4] F. D. Auret, S. M. M. Coelho, M. Hayes, W. E. Meyer, and J. M. Nel. Electrical characterization of defects introduced in Ge during electron beam deposition of different metals. *physica status solidi (a)*, 205(1):159–161, 2008. [2, 55]

[5] E. Simoen and J. Vanhellemont. On the diffusion and activation of ion-implanted n-type dopants in germanium. *Journal of Applied Physics*, 106(10):103516, 2009. [2]

[6] F. D. Auret, P. J. Janse van Rensburg, M. Hayes, J. M. Nel, S. Coelho, W. E. Meyer, S. Decoster, V. Matias, A. Vantomme, and D. Smeets. Electrical characterization of defects in heavy-ion implanted n-type Ge. *Nuclear Instruments and Methods in Physics Research Section B: Beam Interactions with Materials and Atoms*, 257(1–2):169–171, 2007. [2]

[7] F. D. Auret, S. M. M. Coelho, G. Myburg, P. J. Janse van Rensburg, and W. E. Meyer. Electronic and annealing properties of the E 0.31 defect introduced during ar plasma etching of germanium. *Physica B: Condensed Matter*, 404(22):4376–4378, 2009. [2]

[8] V. P. Markevich, I. D. Hawkins, A. R. Peaker, V. V. Litvinov, L. I. Murin, L. Dobaczewski, and J. L. Lindström. Electronic properties of vacancy-oxygen complex in Ge crystals. *Applied Physics Letters*, 81(10):1821–1823, 2002. [2, 55]

[9] H. Haesslein, R. Sielemann, and C. Zistl. Vacancies and self-interstitials in germanium observed by perturbed angular correlation spectroscopy. *Physical Review Letters*, 80(12):2626, 1998. [2, 55, 56, 59, 110]

[10] P. Hohenberg and W. Kohn. Inhomogeneous electron gas. *Physical Review*, 136 (3):864–871, 1964. [2, 15, 17]

[11] W. Kohn. Thoughts about density functional theory in 1998. *Journal of Computational Chemistry*, 20(1):1–1, 1999. [2, 15]

[12] W. Kohn and L. J. Sham. Self-consistent equations including exchange and correlation effects. *Physical Review*, 140(4):1133, 1965. [2, 15, 18, 19, 22]

[13] J. P. Perdew, K. Burke, and M. Ernzerhof. Generalized gradient approximation made simple. *Physical Review Letters*, 77(18):3865–3868, 1996. [2, 22, 24, 27]

[14] J. P. Perdew. Accurate density functional for the energy: Real-space cutoff of the gradient expansion for the exchange hole. *Physical Review Letters*, 55(16):1665, 1985. [2, 22]

[15] J. Heyd, G. E. Scuseria, and M. Ernzerhof. Hybrid functionals based on a screened coulomb potential. *The Journal of Chemical Physics*, 118(18):8207–8215, 2003. [2, 25, 71, 109]

[16] A. Chroneos, R. W. Grimes, and C. Tsamis. Atomic scale simulations of arsenic–vacancy complexes in germanium and silicon. *Materials Science in Semiconductor Processing*, 9(4–5):536–540, 2006. [3]

[17] J. Coutinho, S. Öberg, V. J. B. Torres, M. Barroso, R. Jones, and P. R. Briddon. Donor-vacancy complexes in Ge: Cluster and supercell calculations. *Physical Review B*, 73(23):235213, 2006. [3, 59, 73]

[18] J. Vanhellemont, P. Śpiewak, and K. Sueoka. On the solubility and diffusivity of the intrinsic point defects in germanium. *Journal of Applied Physics*, 101(3): 036103, 2007. [3]

[19] P. Deák, B. Aradi, T. Frauenheim, E. Janzén, and A. Gali. Accurate defect levels obtained from the HSE06 range-separated hybrid functional. *Physical Review B*, 81(15):153203, 2010. [3, 23, 24, 25, 27, 28, 39, 56]

[20] M. Kuisma, J. Ojanen, J. Enkovaara, and T. T. Rantala. Kohn-Sham potential with discontinuity for band gap materials. *Physical Review B*, 82(11):115106, 2010. [3, 25]

[21] R. M Martin. *Electronic structure: basic theory and practical methods*. Cambridge University Press, 1999. [8, 37]

[22] R. M. Martin. *Electronic structure: basic theory and practical methods*. Cambridge university press, 2004. [8, 10, 14, 17, 20, 37]

[23] W. Kohn and A. E Mattsson. Edge electron gas. *Physical Review Letters*, 81(16): 3487, 1998. [8, 15]

[24] D. Joubert. Density functionals: theory and applications. In *Lecture Notes in Physics, Berlin Springer Verlag*, volume 500, 1998. [8, 10, 20]

[25] M. Born and R. Oppenheimer. Zur quantentheorie der molekeln. *Annalen der Physik*, 389(20):457–484, 1927. [10]

[26] D. R. Hartree. The wave mechanics of an atom with a non-coulomb central field. Part I. theory and methods. 24(01):89–110, 1928. [11, 12, 14]

[27] V. Fock. Näherungsmethode zur lösung des quantenmechanischen mehrkörper-problems. *Zeitschrift für Physik*, 61(1-2):126–148, 1930. [12]

[28] J. C. Slater. The theory of complex spectra. *Physical Review*, 34(10):1293, 1929. [13]

[29] J. C. Slater. A simplification of the Hartree-Fock method. *Physical Review*, 81 (3):385, 1951. [13]

[30] C. J Cramer. *Essentials of computational chemistry: theories and models*. John Wiley & Sons, 2013. [15]

[31] F. Jensen. *Introduction to computational chemistry*. John Wiley & Sons, 2013. [15]

[32] L. H. Thomas. The calculation of atomic fields. 23(05):542–548, 1927. [15]

[33] E. Fermi. Eine statistische methode zur bestimmung einiger eigenschaften des atoms und ihre anwendung auf die theorie des periodischen systems der elemente. *Zeitschrift für Physik*, 48(1-2):73–79, 1928. [15]

[34] W. Kohn, A. D. Becke, and R. G. Parr. Density functional theory of electronic structure. *The Journal of Physical Chemistry*, 100(31):12974–12980, 1996. [15, 17, 19, 20]

[35] R. M. Dreizler and E. K. U Gross. Springer Science & Business Media, 2012. [15, 17]

[36] M. Levy. Electron densities in search of hamiltonians. *Physical Review A*, 26(3): 1200, 1982. [18]

[37] E. H. Lieb, A. Shimony, and H. Feshbach. Physics as natural philosophy. *Essays in Honor of Laszlo Tisza, MIT Press, Cambridge*, page 111, 1982. [18]

[38] E. H. Lieb. Density functionals for coulomb systems. *Inequalities*, pages 269–303, 2002. [18]

[39] R. G. Parr and W. Yang. *Density-functional theory of atoms and molecules*. Oxford university press, 1989. [22]

[40] F. Tran and P. Blaha. Accurate band gaps of semiconductors and insulators with a semilocal exchange-correlation potential. *Physical Review Letters*, 102 (22):226401, 2009. [22]

[41] F. Fuchs, J. Furthmüller, F. Bechstedt, M. Shishkin, and G. Kresse. Quasiparticle band structure based on a generalized Kohn-Sham scheme. *Physical Review B*, 76(11):115109, 2007. [22, 23]

[42] A. Seidl, A. Görling, P. Vogl, J. A. Majewski, and M. Levy. Generalized Kohn-Sham schemes and the band-gap problem. *Physical Review B*, 53(7):3764–3774, 1996. [22, 23]

[43] J. Muscat, A. Wander, and N.M. Harrison. On the prediction of band gaps from hybrid functional theory. *Chemical Physics Letters*, 342(3):397–401, 2001. [22]

[44] J. P. Perdew and M. Levy. Physical content of the exact Kohn-Sham orbital energies: band gaps and derivative discontinuities. *Physical Review Letters*, 51 (20):1884–1887, 1983. [22, 24]

[45] B. G. Johnson, P. M. W. Gill, and J. A. Pople. The performance of a family of

density functional methods. *The Journal of Chemical Physics*, 98(7):5612–5626, 1993. [22, 24]

[46] C. W Murray, N. C. Handy, and R. D. Amos. A study of O3, S3, CH2, and Be2 using Kohn–Sham theory with accurate quadrature and large basis sets. *The Journal of Chemical Physics*, 98(9):7145–7151, 1993. [22, 24]

[47] J. P. Perdew and Y. Wang. Accurate and simple analytic representation of the electron-gas correlation energy. *Physical Review B*, 45(23):13244, 1992. [22, 24]

[48] E. Igumbor, K. Obodo, and W. E. Meyer. Ab initio study of MgSe self-interstitial (Mgi and Sei). *Solid State Phenomena*, 242:440–446, 2015. [22, 24, 27, 43, 61]

[49] O. Bengone, M. Alouani, P. Blöchl, and J. Hugel. Implementation of the projector augmented-wave LDA+U method: Application to the electronic structure of NiO. *Physical Review B*, 62(24):16392–16401, 2000. [22]

[50] A. Rohrbach, J. Hafner, and G. Kresse. Electronic correlation effects in transition-metal sulfides. *Journal of Physics: Condensed Matter*, 15(6):979, 2003. [22]

[51] P. Melissa, H. Jrgen, and M. Martijn. Structural, electronic and magnetic properties of gd investigated by dft+ u methods: bulk, clean and h-covered (0001) surfaces. *Journal of Physics: Condensed Matter*, 18(30):7021, 2006. [22]

[52] A. J. Cohen, P. Mori-Sánchez, and W. Yang. Challenges for density functional theory. *Chemical Reviews*, 112(1):289–320, 2011. [23, 24]

[53] J. P. Perdew, A. Ruzsinszky, G. I. Csonka, O. A. Vydrov, G. E. Scuseria, L.A. Constantin, X. Zhou, and K. Burke. Restoring the density-gradient expansion for exchange in solids and surfaces. *Physical Review Letters*, 100(13):136406, 2008. [24]

[54] J. Hafner. Ab-initio simulations of materials using VASP: Density-functional theory and beyond. *Journal of computational chemistry*, 29(13):2044–2078, 2008. [24, 25, 61, 62]

[55] C. Lee, W. Yang, and R. G. Parr. Development of the colle-salvetti correlation-energy formula into a functional of the electron density. *Physical Review B*, 37 (2):785–789, 1988. [24]

[56] C. Sosa and C. Lee. Density functional description of transition structures using nonlocal corrections. silylene insertion reactions into the hydrogen molecule. *The Journal of Chemical Physics*, 98(10):8004–8011, 1993. [24]

[57] P. Bagno, O. Jepsen, and O. Gunnarsson. Ground-state properties of third-row elements with nonlocal density functionals. *Physical Review B*, 40(3):1997, 1989. [24]

[58] M. Dion, H. Rydberg, E. Schröder, D. C. Langreth, and B. I. Lundqvist. Van der waals density functional for general geometries. *Physical Review Letters*, 92(24): 246401, 2004. [24]

[59] A. D. Becke. Density-functional thermochemistry III the role of exact exchange. *The Journal of Chemical Physics*, 98(7):5648–5652, 1993. [25]

[60] P.J. Stephens, F.J. Devlin, C.F. Chabalowski, and M.J. Frisch. Ab initio calculation of vibrational absorption and circular dichroism spectra using density functional force fields. *The Journal of Physical Chemistry*, 98(45):11623–11627, 1994. [25]

[61] M. Ernzerhof and G. E. Scuseria. Assessment of the perdew–burke–ernzerhof exchange-correlation functional. *The Journal of Chemical Physics*, 110(11):5029–5036, 1999. [25]

[62] C. Adamo and V. Barone. Toward reliable density functional methods without adjustable parameters: The PBE0 model. *The Journal of Chemical Physics*, 110 (13):6158–6170, 1999. [25]

[63] A. V. Krukau, O. A. Vydrov, A. F. Izmaylov, and G. E. Scuseria. Influence of the exchange screening parameter on the performance of screened hybrid functionals. *The Journal of Chemical Physics*, 125(22):224106–224106, 2006. [25, 27, 109]

[64] J. P. Dombroski, S. W. Taylor, and P.M.W. Gill. Kwik: Coulomb energies in O (N) work. *The Journal of Physical Chemistry*, 100(15):6272–6276, 1996. [26]

[65] S. J. Clark and J. Robertson. Screened exchange density functional applied to solids. *Physical Review B*, 82(8):085208, 2010. [26]

[66] M. Amini. *First-Principles study of defects in transparent conducting oxide materials*. Universiteit Antwerpen (Belgium), 2014. [27, 49, 65]

[67] F. Drief, A. Tadjer, D. Mesri, and H. Aourag. First principles study of structural, electronic, elastic and optical properties of MgS, MgSe and MgTe. *Catalysis Today*, 89(3):343–355, 2004. [27]

[68] D. J. Chadi and K. J. Chang. Energetics of dx-center formation in GaAs and AlxGa1-x as alloys. *Physical Review B*, 39(14):10063, 1989. [27]

[69] E. Igumbor and W. E. Meyer. A hybrid functional calculation of Tm3+ defects in germanium (Ge). *Materials Science in Semiconductor Processing*, 43:129–133, 2016. [28, 43]

[70] J. L. F. Da Silva, M. V. Ganduglia-Pirovano, J. Sauer, V. Bayer, and G. Kresse. Hybrid functionals applied to rare-earth oxides: The example of ceria. *Physical Review B*, 75(4):045121, 2007. [28]

[71] B. G. Janesko, T. M. Henderson, and G. E. Scuseria. Screened hybrid density functionals for solid-state chemistry and physics. *Physical Chemistry Chemical Physics*, 11(3):443–454, 2009. [28]

[72] C. Kittel. *Introduction to solid state physics*. Wiley, 2005. [28, 37]

[73] H. J. Monkhorst and J. D. Pack. Special points for Brillouin-zone integrations. *Physical Review B*, 13(12):5188–5192, 1976. [29, 35, 71]

[74] Jorge Kohanoff. *Electronic structure calculations for solids and molecules: theory and computational methods*. Cambridge University Press, 2006. [29]

[75] R. P. Feynman. Forces in molecules. *Physical Review*, 56(4):340, 1939. [30, 31]

[76] S. T. Epstein, A. C. Hurley, R. E. Wyatt, and R. G. Parr. Integrated and integral HellmannFeynman Formulas. *The Journal of Chemical Physics*, 47(4):1275–1286, 1967. [30, 31]

[77] P. Schwerdtfeger. The pseudopotential approximation in electronic structure theory. *ChemPhysChem*, 12(17):3143–3155, 2011. [32]

[78] M. T. Yin and M. L. Cohen. Theory of ab initio pseudopotential calculations. *Physical Review B*, 25(12):7403, 1982. [32]

[79] M. C. Payne, M. P. Teter, D. C. Allan, T.A. Arias, and J.D. Joannopoulos. Iterative minimization techniques for ab initio total-energy calculations: molecular dynamics and conjugate gradients. *Reviews of Modern Physics*, 64(4):1045, 1992. [32, 61]

[80] P. E. Blöchl. Projector augmented-wave method. *Physical Review B*, 50(24): 17953, 1994. [33, 34, 62, 63, 71]

[81] G. Makov and M. C. Payne. Periodic boundary conditions in ab initio calculations. *Physical Review B*, 51(7):4014, 1995. [34]

[82] C. J. Pickard and M. C. Payne. Extrapolative approaches to Brillouin-zone integration. *Physical Review B*, 59(7):4685, 1999. [34]

[83] D. J. Chadi and M. L. Cohen. Special points in the Brillouin zone. *Physical Review B*, 8(12):5747, 1973. [35]

[84] S. Gotthard, K. Thomas, H. Zoltan, and F. Thomas. Tubular structures of germanium. *Solid State Communications*, 119(12):653 – 657, 2001. [37]

[85] J. Singh. *Semiconductor devices: basic principles*. John Wiley & Sons, 2007. [38]

[86] W. A. Harrison. *Electronic structure and the properties of solids: the physics of the chemical bond*. Courier Corporation, 2012. [38]

[87] C. Claeys and E. Simoen. *Extended defects in germanium: Fundamental and technological aspects*, volume 118. Springer Science & Business Media, 2008. [39]

[88] M. L. Lee, E. A. Fitzgerald, M. T. Bulsara, M. T. Currie, and A. Lochtefeld. Strained Si, SiGe, and Ge channels for high-mobility metal-oxide-semiconductor field-effect transistors. *Journal of Applied Physics*, 97(1):011101, 2005. [39]

[89] P Śpiewak, J. Vanhellemont, K. Sueoka, K. J. Kurzydłowski, and I. Romandic. Ab-initio simulation of self-interstitial in germanium. *Materials Science in Semiconductor Processing*, 11(5):328–331, 2008. [39, 55, 56, 59, 110]

[90] P Śpiewak, J Vanhellemont, and KJ Kurzydłowski. Improved calculation of vacancy properties in Ge using the heyd-scuseria-ernzerhof range-separated hybrid functional. *Journal of Applied Physics*, 110(6):063534, 2011. [39, 42, 56, 70]

[91] J. R. Weber, A. Janotti, and C. G. Van de Walle. Dangling bonds and vacancies in germanium. *Physical Review B*, 87(3):035203, 2013. [39, 56, 59]

[92] E. Igumbor, C. N. M. Ouma, G. Webb, and W. E. Meyer. Ab-initio study of germanium di-interstitial using a hybrid functional (HSE). *Physica B: Condensed Matter*, 480:191–195, 2016. [39, 43, 55, 56]

[93] E. Igumbor, R. E. Mapasha, and W. E. Meyer. Ab_initio study of aluminium impurity and interstitial-substitutional complexes in Ge using a Hybrid functional (HSE). *Journal of Electronic Materials*, pages 1–8, 2016. URL http://dx.doi.org/10.1007/s11664-016-5026-z. [39]

[94] Emmanuel Igumbor, Refilwe Edwin Mapasha, Richard Andrew, and Walter Ernst Meyer. Ia first principle hybrid functional calculation of TmGe3+-VGeVGe defect complexes in germanium. *Computational Condensed Matter*, 8:31–35, 2016. [39, 47]

[95] D. B. Holt and B. G. Yacobi. Cambridge University Press, 2007. [40, 44]

[96] J. H. Crawford and L. M. Slifkin. *Point Defects in Solids: General and ionic crystals*. Springer Science & Business Media, 2013. [40, 41]

[97] M. D. McCluskey and E. E. Haller. *Dopants and defects in semiconductors*. CRC Press, 2012. [41, 43, 44]

[98] A. Carvalho, R. Jones, C. Janke, J. P. Goss, P. R. Briddon, J. Coutinho, and S. Öberg. Self-interstitial in germanium. *Physical Review Letters*, 99(17):175502, 2007. [42, 56, 78, 110]

[99] H. Bracht, S. Schneider, J. N. Klug, C. Y. Liao, J. Lundsgaard Hansen, E. E. Haller, A. N. Larsen, D. Bougeard, M. Posselt, and C. Wündisch. Interstitial-mediated diffusion in germanium under proton irradiation. *Physical Review Letters*, 103(25):255501, 2009. [42]

[100] A. Chroneos and H. Bracht. Diffusion of n-type dopants in germanium. *Applied Physics Reviews*, 1(1):011301, 2014. [42, 55]

[101] S. Lany and A. Zunger. Assessment of correction methods for the band-gap problem and for finite-size effects in supercell defect calculations: Case studies for ZnO and GaAs. *Physical Review B*, 78(23):235104, 2008. [44, 47, 64, 66, 72]

[102] C. G. Van de Walle and J. Neugebauer. First-principles calculations for defects and impurities: Applications to III-nitrides. *Journal of Applied Physics*, 95(8): 3851–3879, 2004. [44, 45, 47, 62, 63, 65]

[103] S.B. Zhang and J. E. Northrup. Chemical potential dependence of defect formation energies in GaAs: Application to Ga self-diffusion. *Physical Review Letters*, 67(17):2339, 1991. [45, 46, 47]

[104] C. Freysoldt, B. Grabowski, T. Hickel, J. Neugebauer, G. Kresse, A. Janotti, and G. C. Van de Walle. First-principles calculations for point defects in solids. *Rev. Mod. Phys.*, 86(1):253–305, 2014. [46, 47, 49, 51, 63, 64, 65, 72]

[105] P. Śpiewak, K. Sueoka, J. Vanhellemont, K.J. Kurzydłowski, K. Młynarczyk, P. Wabiński, and I. Romandic. Ab initio calculation of the formation energy of charged vacancies in germanium. *Physica B: Condensed Matter*, 401–402(0): 205–209, 2007. [47, 55, 56, 59]

[106] G. Zollo, Y. J. Lee, and R. M. Nieminen. Properties of intrinsic di-interstitials in GaAs. *Journal of Physics: Condensed Matter*, 16(49):8991, 2004. [47]

[107] A. Chroneos, B. P. Uberuaga, and R. W. Grimes. Carbon, dopant, and vacancy interactions in germanium. *Journal of Applied Physics*, 102(8):083707, 2007. [48, 57, 70, 110]

[108] W. E. Meyer. *Digital DLTS studies on radiation induced defects in Si, GaAs and GaN*. University of Pretoria (South Africa), 2007. [50]

[109] J. Dkabrowski and M. Scheffler. Defect metastability in III-V compounds. *Materials Science Forum*, 83:735–750, 1992. [50]

[110] M. Risse and R. Vianden. Metastable behavior of anion-site donors in InAs. *Journal of applied physics*, 93(5):2648–2652, 2003. [50, 51]

[111] D. E. Onopko, A. I. Ryskin, and N. T. Bagraev. Electron-structural metastability of cationic donor centers in GaAs. *Semiconductors*, 31(11):1128–1131, 1997. [50, 51]

[112] R. L. Jones and P. Fisher. Excitation spectra of group III impurities in germanium. *Journal of Physics and Chemistry of Solids*, 26(7):1125–1131, 1965. [52]

[113] S. T. Pantelides. The electronic structure of impurities and other point defects in semiconductors. *Reviews of Modern Physics*, 50(4):797, 1978. [52]

[114] T. Mattila and A. Zunger. Deep electronic gap levels induced by isovalent p and as impurities in gan. *Physical Review B*, 58(3):1367, 1998. [52, 53]

[115] E. E Haller, B. Joos, and L. M. Falicov. Acceptor complexes in germanium: Systems with tunneling hydrogen. *Physical Review B*, 21(10):4729, 1980. [52]

[116] Y. Zhang and J. Wang. Bound exciton model for an acceptor in a semiconductor. *Physical Review B*, 90(15):155201, 2014. [52]

[117] E. Cohen and M. D. Sturge. Excited states of excitons bound to nitrogen pairs in gap. *Physical Review B*, 15(2):1039, 1977. [52]

[118] J. Bardeen and W. H. Brattain. The transistor, a semi-conductor triode. *Physical Review*, 74(2):230–231, 1948. [53, 54]

[119] W. F Brinkman, D. E Haggan, and W. W Troutman. A history of the invention of the transistor and where it will lead us. *Solid-State Circuits, IEEE Journal of*, 32(12):1858–1865, 1997. [53, 54]

[120] O. C. Chi, K. Hyoungsub, P. C. McIntyre, and K. C. Saraswat. A germanium nmosfet process integrating metal gate and improved hi-kappa; dielectrics. *Electron Devices Meeting, 2003. IEDM '03 Technical Digest. IEEE International*, pages 1831–1834, 2003. [54]

[121] M. Houssa, A. Satta, E. Simoen, B. De, M. Jaeger, M. Caymax, and M. Heyns. *Germanium-Based Technologies: From Materials to Devices*, page 233, 2011. [54]

[122] J. S. Coursey, D. J. Schwab, J. J. Tsai, and R. A. Dragoset. Atomic weights and isotopic compositions. *National Institute of Standards and Technology Gaithersburg, MD*, 69(1):13–44, 2014. [54]

[123] J. Emsley. *Nature's building blocks: an AZ guide to the elements*. Oxford University Press, 2011. [54]

[124] W. M. Haynes. *CRC handbook of chemistry and physics*. CRC press, 2014. [54]

[125] G. Audi, M. Wang, A. H. Wapstra, F. G. Kondev, M. MacCormick, X. Xu, and B. Pfeiffer. The Ame2012 atomic mass evaluation. *Chinese Physics C*, 36(12): 1287, 2012. [54]

[126] O. Madelung. *Semiconductors: Group IV elements and III-V compounds*. Springer Science & Business Media, 2012. [54]

[127] J. Vanhellemont, J. Lauwaert, A. Witecka, P. Śpiewak, I. Romandic, and P. Clauws. *Physica B: Condensed Matter*, 404(23):4529–4532, 2009. [55]

[128] J. Fage-Pedersen, A. Nylandsted Larsen, and A. Mesli. Irradiation-induced de-

fects in ge studied by transient spectroscopies. *Physical Review B*, 62(15):10116–10125, 2000. [55, 59, 73]

[129] P. Fahey, S. S. Iyer, and G. J. Scilla. Experimental evidence of both interstitial- and vacancy-assisted diffusion of Ge in Si. *Applied Physics Letters*, 54(9):843–845, 1989. [55]

[130] V. P. Markevich, I. D. Hawkins, A. R. Peaker, K. V. Emtsev, V. V. Emtsev, V. V. Litvinov, L. I. Murin, and L. Dobaczewski. Vacancy–group-V-impurity atom pairs in Ge crystals doped with P, As, Sb, and Bi. *Physical Review B*, 70 (23):235213, 2004. [55, 58, 59, 73]

[131] E. Simoen, K. Opsomer, C. Claeys, K. Maex, C. Detavernier, R. L. Van Meirhaeghe, and P. Clauws. Study of metal-related deep-level defects in germanide schottky barriers on n-type germanium. *Journal of Applied Physics*, 104(2):023705, 2008. [55]

[132] C. G. Van de Walle, M. Choi, J. R. Weber, J. L. Lyons, and A. Janotti. Defects at Ge/oxide and III–V/oxide interfaces. *Microelectronic Engineering*, 109:211–215, 2013. [55]

[133] S. M. M. Coelho, F. D. Auret, P.J. van Rensburg, and J. M. Nel. Electrical characterization of defects introduced in n-ge during electron beam deposition or exposure. *Journal of Applied Physics*, 114(17):173708, 2013. [55]

[134] P. Śpiewak, J. Vanhellemont, K Sueoka, K. J. Kurzydłowski, and I. Romandic. First principles calculations of the formation energy and deep levels associated with the neutral and charged vacancy in germanium. *Journal of Applied Physics*, 103(8):086103, 2008. [55, 56, 59]

[135] H. Bracht, S. Schneider, and R. Kube. Diffusion and doping issues in germanium. *Microelectronic Engineering*, 88(4):452–457, 2011. [55]

[136] C. Janke, R. Jones, S. Öberg, and P. R. Briddon. Supercell and cluster density functional calculations of the thermal stability of the divacancy in germanium. *Physical Review B*, 75(19):195208, 2007. [55, 57, 59]

[137] C. O. Chui, K. Gopalakrishnan, P. B. Griffin, J. D. Plummer, and K. C. Saraswat. Activation and diffusion studies of ion-implanted p and n dopants in germanium. *Applied physics letters*, 83(16):3275–3277, 2003. [55]

[138] J. R. Weber, A. Janotti, and C. G. Van de Walle. Defects in germanium. *Photonics and Electronics with Germanium*, 1:1, 2015. [55, 56, 78]

[139] M. D. Moreira, R. H. Miwa, and P. Venezuela. Electronic and structural properties of germanium self-interstitials. *Physical Review B*, 70:115215, 2004. [56, 59]

[140] E. Kamiyama, K. Sueoka, and J. Vanhellemont. Surface-induced charge at a Ge (100) dimer surface and its interaction with vacancies and self-interstitials. *Journal of Applied Physics*, 113(9):5, 2013. [56]

[141] A. Fazzio, A. Janotti, A. J.R. da Silva, and R. Mota. Microscopic picture of the single vacancy in germanium. *Physical Review B*, 61(4):2401, 2000. [56, 59]

[142] C. Zistl, R. Sielemann, H. Haesslein, S. Gall, D. Bräunig, and J. Bollmann. DLTS combined with perturbed angular correlation (PAC) on radioactive 111 In atoms in Ge. *Materials Science Forum*, 258:53–58, 1997. [56, 59]

[143] J. Coutinho, R. Jones, V. J. B. Torres, M. Barroso, Söberg, and P. R. Briddon. Electronic structure and jahnteller instabilities in a single vacancy in Ge. *Journal of Physics: Condensed Matter*, 17(48):521, 2005. [56]

[144] H. Tahini, A. Chroneos, R. W. Grimes, U. Schwingenschlögl, and H. Bracht.

Diffusion of e centers in germanium predicted using GGA+ U approach. *Applied Physics Letters*, 99(7):072112, 2011. [56, 57, 59]

[145] F. Ishii and M. Saito. First-principles calculations of multivacancies in germanium. *Japanese Journal of Applied Physics*, 55(1):011301, 2015. [57, 59]

[146] A. Chroneos, R. Kube, H. Bracht, R. W. Grimes, and U. Schwingenschlögl. Vacancy–indium clusters in implanted germanium. *Chemical Physics Letters*, 490(1):38–40, 2010. [57]

[147] A. Chroneos. Dopant-vacancy cluster formation in germanium. *Journal of Applied Physics*, 107(7), 2010. [57, 70]

[148] A. Chroneos, C. A. Londos, and H. Bracht. A-centers and isovalent impurities in germanium: Density functional theory calculations. *Materials Science and Engineering: B*, 176(5):453–457, 2011. [58, 70]

[149] J. Lauwaert, S.H. Segers, F. Moens, K. Opsomer, P. Clauws, F. Callens, E. Simoen, and H. Vrielinck. Electronic properties of manganese impurities in germanium. *Journal of Physics D: Applied Physics*, 48(17):175101, 2015. [58, 59]

[150] A Colder, M Levalois, and P Marie. Study of electron, proton, and swift heavy ion irradiation of n-type germanium using deep level transient spectroscopy. *Journal of Applied Physics*, 88(5):3082–3084, 2000. [59, 73]

[151] G. Kresse and J. Furthmüller. Efficient iterative schemes for ab initio total-energy calculations using a plane-wave basis set. *Physical Review B*, 54(16):11169, 1996. [61, 62, 71]

[152] G. Kresse and D. Joubert. From ultrasoft pseudopotentials to the projector augmented-wave method. *Physical Review B*, 59(3):1758, 1999. [61, 62, 71]

[153] P. Giannozzi, S. Baroni, N. Bonini, M. Calandra, R. Car, C. Cavazzoni, D. Ceresoli, G. L. Chiarotti, M. Cococcioni, I. Dabo, et al. QUANTUM ESPRESSO: a modular and open-source software project for quantum simulations of materials. *Journal of Physics: Condensed Matter*, 21(39):395502, 2009. [61]

[154] E. Artacho, E. Anglada, O. Diéguez, J. D. Gale, A. García, J. Junquera, R. M. Martin, P. Ordejón, J. M. Pruneda, and D. Sánchez-Portal. The SIESTA method; developments and applicability. *Journal of Physics: Condensed Matter*, 20(6): 064208, 2008. [61]

[155] T. B. Martins, R. H. Miwa, A. J. R. da Silva, and A. Fazzio. Electronic and transport properties of boron-doped graphene nanoribbons. *Physical Review Letters*, 98(19):196803, 2007. [61]

[156] J. Elsner, R. Jones, P.K. Sitch, V.D. Porezag, M. Elstner, T. Frauenheim, M.I. Heggie, S. öberg, and P.R. Briddon. Theory of threading edge and screw dislocations in GaN. *Physical Review Letters*, 79(19):3672, 1997. [61]

[157] H. Komsa and A. Pasquarello. Assessing the accuracy of hybrid functionals in the determination of defect levels: Application to the as antisite in GaAs. *Physical Review B*, 84(7):075207, 2011. [61]

[158] J. Elsner, R. Jones, M.I. Heggie, P.K. Sitch, M. Haugk, Th. Frauenheim, S. Öberg, and P.R. Briddon. Deep acceptors trapped at threading-edge dislocations in gan. *Physical Review B*, 58(19):12571, 1998. [61]

[159] C.D. Latham, M. Haugk, R. Jones, Th. Frauenheim, and P.R. Briddon. Density-functional calculations of carbon diffusion in GaAs. *Physical Review B*, 60(22): 15117, 1999. [61]

[160] L. Benco, D. Tunega, J. Hafner, and H. Lischka. Upper limit of the OH O hydrogen bond. Ab initio study of the kaolinite structure. *The Journal of Physical Chemistry B*, 105(44):10812–10817, 2001. [61, 62]

[161] G. Kresse and J. Furthmüller. Efficiency of ab-initio total energy calculations for metals and semiconductors using a plane-wave basis set. *Computational Materials Science*, 6(1):15–50, 1996. [61]

[162] D. R. Hamann, M. Schlüter, and C. Chiang. Norm-conserving pseudopotentials. *Physical Review Letters*, 43(20):1494, 1979. [61]

[163] D. Vanderbilt. Soft self-consistent pseudopotentials in a generalized eigenvalue formalism. *Physical Review B*, 41(11):7892, 1990. [61]

[164] B. Adolph, J. Furthmüller, and F. Bechstedt. Optical properties of semiconductors using projector-augmented waves. *Physical Review B*, 63(12):125108, 2001. [61]

[165] V. Brázdová and D. R. Bowler. *Atomistic computer simulations: a practical guide*. John Wiley & Sons, 2013. [62]

[166] C. Freysoldt, J. Neugebauer, and C. G. Van de Walle. Electrostatic interactions between charged defects in supercells. *physica status solidi (b)*, 248(5):1067–1076, 2011. [62, 66, 67, 68, 72]

[167] C. Freysoldt, J. Neugebauer, and C. G Van de Walle. Fully ab initio finite-size corrections for charged-defect supercell calculations. *Physical Review Letters*, 102 (1):016402, 2009. [62, 63, 64, 65, 66, 67, 68]

[168] S. Lany and A. Zunger. Accurate prediction of defect properties in density functional supercell calculations. *Modelling and Simulation in Materials Science and Engineering*, 17(8):084002, 2009. [62, 63, 65, 66]

[169] Y. Kumagai and F. Oba. Electrostatics-based finite-size corrections for first-principles point defect calculations. *Physical Review B*, 89(19):195205, 2014. [64, 65, 66, 68]

[170] H. Komsa, T. T. Rantala, and A. Pasquarello. Finite-size supercell correction schemes for charged defect calculations. *Physical Review B*, 86(4):045112, 2012. [64, 67]

[171] G. Makov and M.C. Payne. Periodic boundary conditions in ab initio calculations. *Physical Review B*, 51(7):4014, 1995. [65, 66]

[172] A. Alkauskas, P. Broqvist, and A. Pasquarello. Defect levels through hybrid density functionals: Insights and applications. *physica status solidi (b)*, 248(4): 775–789, 2011. [65]

[173] M. Leslie and N.J. Gillan. The energy and elastic dipole tensor of defects in ionic crystals calculated by the supercell method. *Journal of Physics C: Solid State Physics*, 18(5):973, 1985. [66]

[174] N.D.M. Hine, K. Frensch, W.M.C. Foulkes, and M.W. Finnis. Supercell size scaling of density functional theory formation energies of charged defects. *Physical Review B*, 79(2):024112, 2009. [67]

[175] J. Heyd and G. E. Scuseria. Assessment and validation of a screened coulomb hybrid density functional. *The Journal of Chemical Physics*, 120(16):7274–7280, 2004. [71]

[176] C. E. Lindberg, J. L. Hansen, P. Bomholt, A. Mesli, K. B. Nielsen, A. N. Larsen, and L. Dobaczewski. The antimony-vacancy defect in p-type germanium. *Applied Physics Letters*, 87(17):172103–172103, 2005. [73]

[177] H. P. Singh. Determination of thermal expansion of germanium, rhodium and iridium by X-rays. *Acta Crystallographica Section A*, 24(4):469–471, 1968. [110]